


Influence of (Ba,F) multidoping on structural, magnetic, optical, and electrical properties as well as performance enhancement of multiferroic BiFeO₃

Shahrbano Rahimi, Reyhaneh Ebrahimi-Jaberi, Farhad Jalali-Asadabadi, Leila Mollabashi, and S. Jalali-Asadabadi ^{*}
Department of Physics, Faculty of Physics, University of Isfahan (UI), Hezar Jerib Avenue, Isfahan 81746-73441, Iran

 (Received 30 May 2022; revised 19 August 2022; accepted 9 September 2022; published 28 September 2022)

Antiferromagnetic (AFM) and high ferroelectric (FE) orderings coexist in the pristine BiFeO₃. However, its performance is suppressed by complex FE switching originated from its *R3c* space group and high leakage current due to the volatile nature of Bi. We theoretically predict that the performance can be enhanced by (B,F) codoping. To this end, BiFeO₃ and its Ba-doped, Bi_{1-x}Ba_xFeO_{3-x/2}, as well as (Ba,F) multidoped, Bi_{1-x}Ba_xFeO_{3-x}F_x, are analyzed structurally, magnetically, optically, and electrically for the pure (doped) compound (compositions), where $x = 0.25$. The analyses are performed in the framework of density functional theory accompanied by random phase approximation, Berry phase theory, and Hubbard model using PBE-GGA + U with $U_{\text{eff}} = 4(5)$ eV. Here, we predict that the tetragonal polar distortions of the co-doped compound with an AFM ordering lead to a nonzero spontaneous polarization. Hence, both the magnetic and electric polarizations coexist in the codoped composition. To assess the accuracy of the results, we calculate the spontaneous polarization for the pure BiFeO₃ in both the *R3c* and *P4mm* symmetries and find the results in agreement with the available experimental and theoretical data. Furthermore, our dielectric functions for the pure case are found consistent with the experimental data. Moreover, absorption coefficient spectra, as calculated by GGA + U with $U_{\text{eff}} = 4$ eV and TB-mBJ with its self-consistently converged $c = 1.38$ parameter, using Tauc method also reveal direct optical gaps of 2.66 and 2.80 eV, which agree with the corresponding experimental optical gap of 2.74 eV. To study the impacts of doping on the intrinsic ferroelectricity improvement of BiFeO₃, we then calculate and analyze the optical absorption edges and loss functions for the pristine and doped compounds. By taking the band structure, partial densities of states, energy loss function, and parallel component of the imaginary part of the dielectric tensor, $\Im[\epsilon_{\parallel}]$, for the pure case into consideration simultaneously, the energies of the prominent peaks for $\Im[\epsilon_{\parallel}]$ spectra and their corresponding permitted absorption (emission) transitions are rigorously analyzed and determined. The analyses reveal that the sources of the prominent peaks occurred in $\Im[\epsilon_{\parallel}]$ mainly originate from the excitation states of the bound electrons of O *2s*, O *2p*, Bi *6s*, Bi *6p*, Fe *3d*, and Fe *4s* orbitals. Our results in most of the energy ranges show that the intrinsic ferroelectricity can be improved by the (Ba,F) codoping due to the reduction of the leakage current achieving from the calculated electric energy loss function. Further, the rhombohedral (*R3c*) is changed by the codoping to the tetragonal (*P4mm*) structure with more convenient symmetry for polarization switching. Hence, the system not only remains multiferroic after the codoping, but also its performance is enhanced. These evidences show that the codoping can play a key role for the applications of this multiferroic system in various devices.

DOI: [10.1103/PhysRevB.106.115205](https://doi.org/10.1103/PhysRevB.106.115205)

I. INTRODUCTION

Multiferroic systems due to their multifunctionality play a vital role in reducing the size of modern devices engineered by advanced materials and thence are attractive for a variety of high technology applications (HTAs) [1–3]. Particularly, the bismuth-based multiferroic systems have attracted considerable attention in a broad range of HTAs because they are environment-friendly, low-cost, useful for developing high energy density capacitors, clean energy exploration and environmental remediation, and functionality induced by conversion between mechanical and electrical energy [4–9]. More specifically, BiFeO₃ as a multifunctional compound with space group *R3c* is a primary multiferroic material due

to the coexistence of ferroelectric (FE) and anti-ferromagnetic (AFM) orderings at room temperature [10–14].

Extremely high polarization was reported for BiFeO₃ [15–17]. However, it can be argued that the *R3c* structure has significant problems and challenges [18]. It is well known that, in practice, it is difficult to synthesize the stoichiometric BiFeO₃, as reviewed by Silva *et al.* [19]. In addition to the above practical difficulty of synthesizing the ideal stoichiometric BiFeO₃ single crystal, FE polarization along [111] direction creates eight possible orientations [18]. Due to these possibilities, ferroelectric switching is complex and whence difficult to control for BiFeO₃ with the *R3c* symmetry [18]. Therefore, demands for finding other structures than *R3c* for BiFeO₃ have been increased [20]. Makhdoom *et al.* explored the structural phase transition from rhombohedral to pseudocubic symmetry in polycrystalline samples with formula Bi_{1-x}Ba_xFeO₃ ($x = 0.00$ – 0.25) using XRD diffraction [21].

^{*}Corresponding author: sjalali@sci.ui.ac.ir

However, pseudocubic symmetry is not suitable for ferroelectric point of view [22]. BiFeO₃ thin films under biaxial compressive strain can be deflected from the rhombohedral to the tetragonal with a high c/a ratio [23–25]. Oliver *et al.* reported on the synthesis, crystallographic, and magnetic structures of Ba and (Ba,F)-codoped BiFeO₃ compounds with compositions Bi_{1-x}Ba_xFeO_{3-x/2} and Bi_{1-x}Ba_xFeO_{3-x}F_x, respectively [26]. They [26] in agreement with Makhdoom *et al.* [21], found that the c/a ratios for the oxide compounds were remain pseudocubic, i.e. 1, for $x = 0.2$ and nearly pseudocubic, i.e., $1.003 \approx 1$, for $x = 0.3$. However, they [26] explored two large tetragonal polar distortions, i.e., $c/a \simeq 1.08$ with $x = 0.2$ and 1.05 with $x = 0.3$, for the oxyfluoride compounds exhibiting G-type AFM (G-AFM) ordering in the ab plane. Thus, the space group $R3c$ suffering from the complexity problem of the ferroelectric switching can be transformed by (Ba,F) codoping to a more suitable space group, i.e., $P4mm$, having simpler switching properties than $R3c$ [18]. Furthermore, Oliver *et al.* by neutron powder diffraction found that the remanent magnetization in the oxide compound, Ba-doped BiFeO₃, was related to the ferrimagnetic impurity BiFe₁₂O₁₉ and not to an intrinsic property of the oxide compounds [26]. From the above reviewed and discussed evidences, the new oxyfluoride compounds in question with tetragonal structure, $c/a \geq 1.05$, would be good candidates for the novel multiferroic materials. Therefore, here, we intend to shed light into the electronic structures and optical as well as electrical properties of all these multiferroic compounds to profoundly understand the physical mechanism governed. Furthermore, we below discuss another motivation that has attracted our attention to study these compounds. Besides the adversity of manufacturing nominal stoichiometric crystal, and the switching problem of the $R3c$ symmetry and the proposed solutions discussed above, another limitation that declines the ferroelectric properties has been attributed to the high levels of leakage current presented in the BiFeO₃ [27,28]. The volatile nature of Bi and changing valency of iron ion from trivalent to divalent, as Fe⁺³ to Fe⁺², can produce defects such as oxygen vacancies, especially in the thin films of BiFeO₃. Therefore, the BiFeO₃ exhibits a high leakage that reduces the residual polarization in this material [28,29]. Consequently, the intrinsic conductivity of nonstoichiometric BiFeO₃ makes it not so useful in ferroelectric applications. According to the earlier investigations, small dielectric loss at low frequencies reflects a reduction in leakage current [27,28,30]. Therefore, theoretical and experimental investigations of the optical properties of BiFeO₃ and comparing them with those of doped BiFeO₃ may be very helpful. Choi *et al.* determined the dielectric function and refractive index spectra of BiFeO₃ by spectroscopic ellipsometry [31]. Liu *et al.* used density functional theory (DFT) within generalized gradient approximation (GGA) and Lima employed Hubbard model using PBE-GGA + U with $U_{\text{eff}} = 6$ eV to determine the optical properties of rhombohedral BiFeO₃ [32,33]. Makhdoom *et al.* [21] measured the optical properties for Ba doped BiFeO₃ in the pseudocubic symmetry and found a reduction in the dielectric constant compared to the pure case. However, there are theoretical and experimental data lacking in the electronic, optical, and electrical properties for the tetragonal symmetry of Bi_{1-x}Ba_xFeO_{3-x/2} and Bi_{1-x}Ba_xFeO_{3-x}F_x. The above important evidences mo-

tivated us to investigate the leakage current of these possible multiferroic compounds. Therefore, here, in addition to the structural and electronic properties, we aim to study their optical properties and examine their leakage current using the loss optical function. Furthermore, we calculate the magnitude of the spontaneous electric polarization (SEP) using Berry phase method based on the modern theory of polarization [34–38] for the AFM tetragonal structure of pure and multidoped compounds. By this, we investigate the possibility of coexistence of nonzero ferroelectric polarization and AFM ordering and reduction of the leakage current in the codoped compounds under consideration.

To achieve the goals discussed above, i.e., solving FE switching and leakage current problems by (Ba,F) codoping, we perform DFT calculations using PBE-GGA + U . We then analyze the structural, electronic, optical and electrical properties of the rhombohedral BiFeO₃, pseudocubic Bi_{1-x}Ba_xFeO_{3-x/2} and tetragonal Bi_{1-x}Ba_xFeO_{3-x}F_x, where $x = 0.25$. By our analyses, we predict that the tetragonal Bi_{1-x}Ba_xFeO_{3-x}F_x with $x = 0.25$ would be a G-AFM with nonzero spontaneous polarization and hence a novel multiferroic composition. Moreover, we find that the doped compounds have a smaller leakage current than those of pristine BiFeO₃ in the most energy ranges. In agreement with the experiment [26], we find that G-AFM configuration is more energetically favorable than FM configuration. Our optical results show that the real and imaginary parts of the optical spectra are anisotropic along the two light polarizations for all the materials. This observation is in accordance with the hexagonal and tetragonal symmetries and available experimental data [31,39]. Although Ba doping can decrease the static dielectric constant consistent with experiment [21], we find that this decrement in codoping is smaller than that of Ba-doped compound only. Therefore, the codoped is more suitable than Ba doped from the dielectric point of view. Furthermore, absorption coefficient spectra are obtained from their corresponding extinction coefficient spectra, as calculated by GGA + U with $U_{\text{eff}} = 4$ eV, and various versions of the mBJ methods, including the original TB-mBJ [40], KTB-mBJ [41], Sgap-KTB-mBJ [42], JTSKT-mBJ [43], and Ir-TB-mBJ [41,44]. Then, by means of Tauc approach [45] following the method proposed by Makuła, Pacia, and Macyk [46], we extract, from the absorption coefficient spectra, the direct optical gaps to be 2.66 eV using GGA + U with $U_{\text{eff}} = 4$ eV, and 2.80 eV using TB-mBJ with its self-consistently converged $c = 1.38$ parameter. The calculated optical gaps are found to be consistent with the corresponding experimental optical gap of 2.74 eV [31,39]. The energy loss function (ELF) spectra show great sensitivity to doping and indicate a reduction in the ELF up to 21.65 eV and above the 28.56 eV for both the oxide and oxyfluoride doped compounds compared to the pristine BiFeO₃. The lower dielectric ELF usually shows lower leakage current [27] and thereby it may indicate an improvement in ferroelectric properties. Moreover, we determine the permissible optical absorption and emission transitions to find their sources in the pure case. To this end, we considered the band structure, partial densities of states, energy loss function, and parallel component of the imaginary part of the dielectric tensor, $\Im[\epsilon_{\parallel}]$, at the same time. Then, we rigorously analyze the energies of the prominent

peaks for $\Im[\epsilon_{\parallel}]$ spectra and their corresponding permitted absorption (emission) transitions. From the optical analyses, the origins of the prominent peaks occurred in $\Im[\epsilon_{\parallel}]$ are found to be O 2s, O 2p, Bi 6s, Bi 6p, Fe 3d, and Fe 4s states. In addition, we calculate spontaneous polarizations for the $R3c$ and $P4mm$ symmetries of the pure BiFeO_3 and the multidoped composition in $P4mm$ symmetry. The calculated values for spontaneous polarizations of pristine BiFeO_3 in both $R3c$ and $P4mm$ symmetries are found in agreement with the available theoretical [47–49] and experimental data [50,51]. Due to doping, in addition to the c tetragonal direction, we observe a nonzero component for the polarization along the “ a ” tetragonal direction. Therefore, the main objective of this work is to show that G-AFM tetragonal $\text{Bi}_{1-x}\text{BaF}_x\text{O}_{3-x/2}$ with $x = 0.25$ can be a multifunctional compound with a more convenient symmetry structure compared to the rhombohedral $R3c$ BiFeO_3 and an acceptable spontaneous polarization.

II. CHEMICAL AND MAGNETIC SUPERSTRUCTURES

A. Pure compound

Bismuth iron oxide BiFeO_3 crystallizes in a rhombohedrally distorted simple cubic perovskite cell with space group $R3c$ and lattice parameters $a_r = 5.364 \text{ \AA}$ and $\alpha_r = 59.348^\circ$ [52]. The rhombohedral structure can be converted to the hexagonal structure. To this end, we use the $a = 2a_r \cos[(\pi - \alpha_r)/2]$ and $c = 3[a_r^2 - a^2/3]^{1/2}$ relations, as reported in Chap. 4.3, p. 40 of Ref. [53], to convert the primitive rhombohedral lattice parameter a_r and the rhombohedral angle α_r to the conventional hexagonal lattice parameters a and c , respectively.

In this work, by (Ba,F) codoping we intend to enhance the performance of BiFeO_3 multiferroic, as to be subsequently discussed in Sec. V. Let us discuss below to what extent the stoichiometric BiFeO_3 can be considered as a reference for comparison to ensure the improvement of the results after impurity doping compared to the actual defective nonstoichiometric BiFeO_3 . It is of significant importance to notice that, in practice, it is hard to synthesize the nominal or ideal stoichiometric BiFeO_3 , as indicated in Sec. I and Refs. [19,54]. Nevertheless, so far, remarkable progresses have been made to synthesize highly pure BiFeO_3 . Ortiz-Quiñonez *et al.* have synthesized it using a combustion reaction, employing tartaric acid or glycine as promoter [55]. Peñalva and Lazo also have synthesized it applying the combustion method, utilizing metallic nitrates with a mixture of fuel between glycine and urea [56]. They [56] have determined the stoichiometry ratios of BiFeO_3 by scanning electron microscopy (SEM) and energy dispersive spectroscopy (EDS) techniques obtaining the atomic percentage values of 18.1% for Bi, 22.9% for Fe, and 59% for O, which are close to the theoretical ratios (1 : 1 : 3), viz. $18.1/8.1 = 1.0$, $22.9/18.1 \approx 1.2$, $59/18.1 \approx 3.2 \implies (1.0 : 1.2 : 3.2) \approx (1 : 1 : 3)$. These experimental progresses have led to extensive theoretical studies of the stoichiometric BiFeO_3 by *ab initio* methods. Lima [33] recently has studied electronic structures, effective masses, and magnetic, as well as optical properties of the pure stoichiometric BiFeO_3 in its $R3c$ phase using DFT + U calculations. Benyoussef *et al.* [57] very recently—after synthesizing BiFeO_3 nanoparticles, and depositing them using spray pyrolysis method, as well

as preparing BiFeO_3 thin films—have studied experimentally optical properties of the prepared thin films. Furthermore, they [57] also theoretically studied the bulk and thin films of the pure BiFeO_3 using the ideal stoichiometric rhombohedral structure by performing *ab initio* DFT calculations and found their theoretical results to be in agreement with their experimental data. The above reviewed experimental and theoretical evidences as well as the conciseness achieved between the experimental results of the highly pure synthesized material and the theoretical results of the corresponding stoichiometric material confirm that the defective nonstoichiometric BiFeO_3 can be approximated by its stoichiometric single crystal to the extent discussed above experimentally and theoretically. Therefore, the stoichiometric BiFeO_3 can be considered approximately as a benchmark test to confirm the performance enhancement due to doping. Furthermore, let us discuss below the accuracy of such an approximation. It is well known that the nonstoichiometric BiFeO_3 suffers from the relatively low (high) electrical resistivity (conductivity) leading to leakage current problem [58,59]. The latter problem mainly originates from the valence fluctuation of Fe ions (Fe^{3+} to Fe^{2+}) [58]. This, in turn, produces oxygen vacancies to compensate electric charges [58]. Therefore, an appropriate doping can diminish the oxygen vacancies [58]. This, in turn, can suppress the leakage current of the nonstoichiometric BiFeO_3 due to field-assisted ionic conduction [58]. From the above discussion, higher conductivity is expected in the defective or nonstoichiometric than in the pure or stoichiometric BiFeO_3 . This expectation has been already confirmed by Singh *et al.* [58] and Habouti *et al.* [59] who have shown that the leakage current density in the defective nonstoichiometric BiFeO_3 can be substantially reduced by optimizing the process conditions of stoichiometric BiFeO_3 chemical solution, see also Ref. [60]. Therefore, the ideal stoichiometric BiFeO_3 can be considered as an appropriate criterion for the improvement achieved by doping, since the conductivity of the ideal single crystal is less than that of the defective solid-solution material. Consequently, if the leakage current of the doped-material is less than that of the nominal stoichiometric material, it is most likely also less than that of defective nonstoichiometric material. Furthermore, in this work we also study the single doped composition, i.e., Ba-doped material. Therefore, our Ba-doped case can also provide another alternative reference system for the co-(Ba,F)-doped composition than the theoretical stoichiometric BiFeO_3 or defective BiFeO_3 . Nevertheless, despite the above evidences, we created a defective sample for companion, as well. The comparison once more confirmed that the stoichiometric BiFeO_3 can provide a reliable reference system.

B. Single-doped and codoped compositions

The structure of $\text{Bi}_{1-x}\text{Ba}_x\text{FeO}_{3-x/2}$ ($\text{Bi}_{1-x}\text{Ba}_x\text{FeO}_{3-x/2}$) is tetragonal (pseudocubic) with G-AFM ordering lying in the ab plane [26]. Since the c/a ratio for the pseudocubic compound is not exactly one, i.e., the ratio is slightly larger than unity, we select the $P4mm$ space group even for the pseudocubic compound. In the tetragonal structure, Bi atoms are located at the corners, O atoms are placed at the centers of the faces, and Fe atoms are positioned at the center of the unit

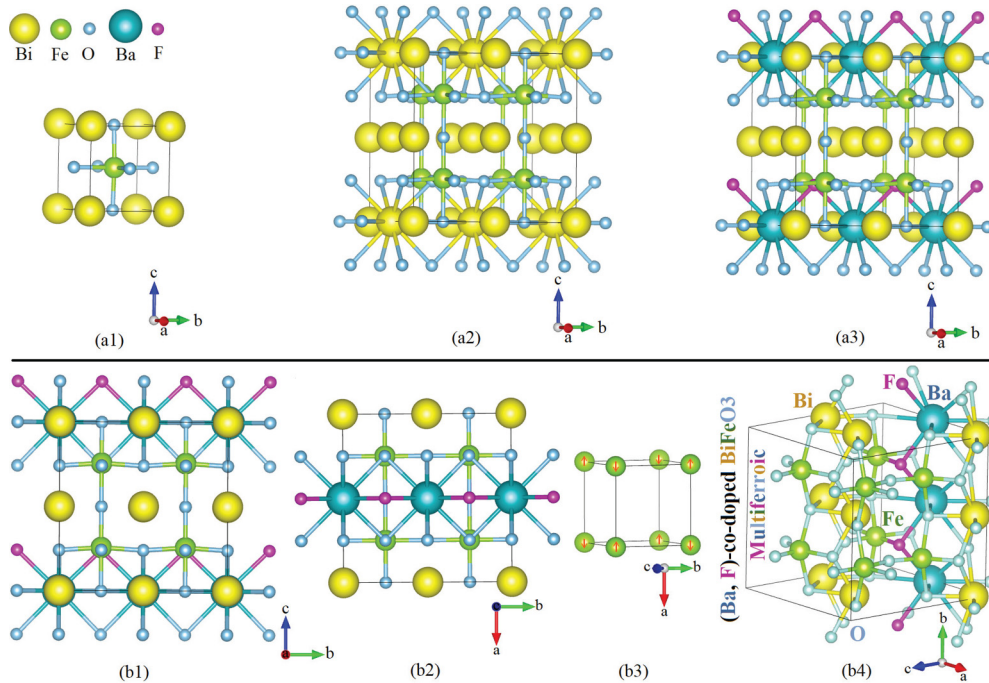


FIG. 1. (a1) Tetragonal structure of BiFeO_3 , (a2) a $2 \times 2 \times 2$ supercell of tetragonal BiFeO_3 , (a3) the latter supercell after codoping Ba and F impurities into the pure compound at Bi and O sites, respectively, (b1) the latter codoped supercell projected in ab plane, (b2) the latter projected codoped supercell after a clockwise rotation by 90° about the transverse b axis, and (b3) magnetic unit cell involving G-AFM spin configurations along a direction. (b4) Crystal structure of (Ba, F)-co-doped- BiFeO_3 .

cell for the tetragonal BiFeO_3 , as shown in Fig. 1(a1). We construct a $2 \times 2 \times 2$ supercell to prepare enough space and/or sites for codoping Ba and F impurities and setup the G-AFM configuration, see Fig. 1(a2). Then, we dope the Ba and F impurities into the pure compound at Ba and F sites, respectively, as shown in Fig. 1(a3). The spins are oriented along either a or b direction. Figures 1(a3) and 1(b1) demonstrate the same structure in different points of view, viz. Fig. 1(b1) is the projection of Fig. 1(a3) on ab plane. In order to orient the spin directions towards a axis, we rotate clockwise the structure by 90 degrees around the b axis, see Fig. 1(b2). The G-AFM spin direction of Fe atoms included in Fig. 1(b2) is shown in Fig. 1(b3). Figure 1(b4) shows the supercell of the (Ba, F)-co-doped- BiFeO_3 . In analogous to the construction of the codoped structure discussed above, we follow the same steps to construct a similar $2 \times 2 \times 2$ supercell to setup the G-AFM structure for the single-doped $\text{Bi}_{1-x}\text{Ba}_x\text{FeO}_{3-x/2}$ ($x = 0.25$), where only Ba impurity and O vacancy are presented in the absence of F impurity. To construct the G-AFM configuration of the pure BiFeO_3 , we use the hexagonal structure with the spin configurations reported in Ref. [61].

Let us below discuss to which extent our selected $2 \times 2 \times 2$ supercell can represent the experimental situation. To this end, we, first, notice that the dimensions of the supercell depend on the percentage (concentration) of the impurity substitution. The impurity concentration can be tuned by the variable x used as the subscript of Ba atom in the chemical formulas of the compositions in question. In this work, we aim to enhance the multiferroic performance of BiFeO_3 by doping. To this end, it is also necessary to reduce the leakage current density (J), as one of the major problems of the pure material, as discussed in Sec. I. We, second, notice that, in addition to

the supercell dimensions, J also depends on x . Therefore, in order to optimize x and whence the supercell dimensions, we consider the experimental behavior of J versus x and choose the x that minimizes J , as an ideal choice, or yields reasonably small J , as an efficient and affordable choice. The latter point, i.e. optimizing x by choosing an efficient and affordable value for x , plays more crucial role, if we, third, note that not only the dimensions of the unit cell but also the number of atoms in the unit cell and as a result the speed of calculations depend on x , as well. Therefore, to find an efficient and affordable x , we, fourth, note the experimental effects of Ba impurity concentration on J . Makhdoom *et al.* [21] have experimentally studied the effects of Ba impurity concentration on J to determine the x variable in their $\text{Bi}_{1-x}\text{Ba}_x\text{FeO}_3$ samples prepared by the conventional solid state reaction method. Since J , based on the power law relation, is proportional to E^m , i.e., $J \propto E^m$, where m is a constant, they have plotted also $\log(J)$ as functions of E for $x = 0, 0.1$, and 0.2 , as shown in Fig. 3(b) of Ref. [21]. By this way, the power relation can be transformed to a linear relation, $\log(J) \propto mE$, where m determines the slope of the line. Figure 3(b) of Ref. [21] shows that for $x = 0.20$, corresponding to 20% Ba impurity concentration, m is unity ($m = 1$), indicating an Ohmic conduction mechanism ($J \propto E$), for intermediate electric field region, and $m > 2$, indicating the space-charge-limited conduction mechanism, for the high electric field region. Figure 3(a) of Ref. [21] shows that J for $x = 0.25$ behaves like and thereby follows the same mechanism as J for $x = 0.2$. More importantly the J curve for $x = 0.25$ is located under the J curve for $x = 0.20$ for all the electric field region. As a result, the leakage current density for $x = 0.25$ is less than that for $x = 0.20$. This figure shows the following behaviors for the leakage current density:

TABLE I. Concentrations of Ba impurity (x) and their corresponding dimensions of the supercells (Supercell) as well as their corresponding number of atoms (NA) for $\text{Bi}_{1-x}\text{Ba}_x\text{FeO}_3$ composition. The interval for the variation of x in this table is selected based on the experimental data reported by Makhdoom *et al.* [21] and Clemens *et al.* [26].

x	Supercell	NA
0.00	$2 \times 2 \times 2$	40
0.05	$2 \times 2 \times 5$	100
0.50	$2 \times 2 \times 2$	40
0.10	$2 \times 2 \times 5$	100
0.15	$2 \times 2 \times 5$	100
0.20	$2 \times 2 \times 5$	100
0.25	$2 \times 2 \times 2$	40
0.30	$2 \times 2 \times 5$	100

(i) J is minimized by $x = 0.10$, (ii) J is substantially reduced by $x = 0.15$ and 0.25 compared to the pure material, i.e., $x = 0$, and (iii) J for $x = 0.15$ remains very close to and only a little bit smaller than that for $x = 0.25$. Therefore, based on these behaviors, the ideal choice is $x = 0.10$, since it minimizes J . In order to choose the efficient and affordable x , however, we determine the concentrations of the Ba impurity, and their corresponding dimensions of the supercells, as well as corresponding number of atoms of the supercells for $\text{Bi}_{1-x}\text{Ba}_x\text{FeO}_3$ composition so that G-AFM supercells can be constructed for each case, as tabulate in Table I. From this table the efficient and affordable choice can be determined to be $x = 0.25$, since not only its leakage is considerably less than that of $x = 0.20$ but also its number of atoms is much less than those of $x = 0.10$, 0.15 , and 0.20 . Therefore, we choose $x = 0.25$ which is corresponding to the $2 \times 2 \times 2$ supercell rather than the ideal choice of $x = 0.10$ and a little bit better choice of $x = 0.15$ which are both corresponding to a $2 \times 2 \times 5$ supercell, since not only the calculations can be speed up but also more importantly the leakage current can be substantially reduced by this efficient and affordable supercell. Hence, the accuracy of the calculations are reported to the experimental extent discussed above in this work.

III. COMPUTATIONAL DETAILS

The first principle calculations were performed using DFT [62,63] as implemented in the WIEN2K simulation package [53,64,65] employing PBE-GGA [66], and GGA + U [67,68] for the exchange-correlation functional. It is well-known that the Hubbard U parameter can be case-dependent [69–74]. Therefore, we try to optimize the U_{eff} case by case. Our results show that $U_{\text{eff}} = 4$ eV can reproduce nearly acceptable experimental data for both the pure and doped compounds. However, we perform more elaborations and optimize the U_{eff} to be 4(5) eV for the pure (doped) case by fitting to the experimental magnetic moment per each Fe atom [26] and optical properties [31]. Therefore, both of the optimized values of U_{eff} , i.e., 4 and 5 eV, are used in this work to predict the electrical and optical properties. We optimize the k mesh to be $9 \times 9 \times 3$ ($14 \times 14 \times 4$) in the first Brillian zone (1BZ) for

the self-consistent (SCF) DFT (post-processing optical) calculations of the $R3c$ unit cell of the pure case. For the $P4mm$ supercells of the pure and doped cases, we optimize the k -mesh to be $6 \times 6 \times 6$ ($7 \times 7 \times 8$) in the 1BZ for the SCF-DFT (post-processing optical) calculations. For the expansion of the wave functions (charge densities) $R_{\text{MT}}K_{\text{max}}$ (G_{max}) is optimized to be 7 (12 Bohr $^{-1}$). We select the separation energies to be -9 Ry for separating the valence electrons from the core electrons so that electronic configurations of $6s^24f^{14}5d^{10}6p^3$ for Bi, of $4d^{10}5s^26p^66s^2$ for Ba, of $3s^23p^64s^23d^6$ for Fe, of $2s^22p^4$ for O, and of $2s^22p^5$ for F are applied for the valence electrons included in the SCF-calculations. The radii of the muffin-tin spheres are chosen to be 2.17, 2.15, 1.52, 1.48, and 1.50 Bohr for Bi, Ba, Fe, O, and F atoms, respectively. Internal coordinates and lattice parameters are fully optimized by minimizing the Hellmann-Feynman forces [75] with the criterion of $fc < 1$ mRy/bohr. The spin-orbit coupling (SOC) is considered in all the calculations.

It is well known that the DFT-based methods suffer from the precise electronic band gap prediction [40,41,44,76–78]. Tran and Blaha (TB) [40] have proposed an exchange potential to overcome the latter shortcoming. This potential is called TB-mBJ, see Eq. (4) of Ref. [41] or Eq. (1) of Refs. [40,44]. David Koller, Fabien Tran, and Peter Blaha [41] have also reported merits and limits of TB-mBJ exchange potential. The failure to describe ferromagnetic metals by TB-mBJ is not unexpected, see Table II and the related discussion right below this table of Ref. [41]. In the TB-mBJ exchange potential, there is a correction (c) factor, see Eq. (5) of Ref. [41] or Eq. (3) of Ref. [40] or Eq. (2) of Ref. [44]. This c factor of the TB-mBJ can be expressed as [40]

$$c = \alpha + \beta\sqrt{\bar{g}}, \quad (1)$$

where $\alpha = -0.012$, $\beta = 1.023$ (Bohr) $^{1/2}$, and \bar{g} depends on the electron charge density $\rho(\mathbf{r}')$ and its gradient $\nabla\rho(\mathbf{r}')$ as follows [40]:

$$\bar{g} = \frac{1}{V_{\text{cell}}} \int_{\text{cell}} \frac{|\nabla\rho(\mathbf{r}')|}{\rho(\mathbf{r}')} d\mathbf{r}', \quad (2)$$

which is the average of $g = \nabla\rho(\mathbf{r}')/\rho(\mathbf{r}')$ in the unit cell of volume V_{cell} in the absence of spin polarization. In the presence of spin polarization, \bar{g} can be generalized by taking spins up and down into account, as expressed in Eq. (6) of Ref. [42]. Koller, Tran, and Blaha (KTB) in another contribution [42], than their last contribution [41], have improved the TB-mBJ exchange potential. To this end, they, i.e., KTB [42], generalized the c factor of the TB-mBJ potential from $c = \alpha + \beta\sqrt{\bar{g}}$ with the above ($\alpha = -0.012$, $\beta = 1.023$ (Bohr) $^{1/2}$) to $c = A + B\bar{g}^e$ with ($e = 1$, $A = 0.488$, $B = 0.500$ (Bohr) $^e = 0.500$ (Bohr) $^1 = 0.500$ Bohr) for large band gap insulators, as well as with ($e = 1$, $A = 0.267$, $B = 0.656$ Bohr) for small band gap semiconductors, see Table II of Ref. [42]. Therefore, the TB-mBJ method is called KTB-mBJ, if $c = A + Bg$ is used, whereas it is still called TB-mBJ, if $c = \alpha + \beta\sqrt{\bar{g}}$ is used. The above KTB-mBJ designed for small-gap (Sgap) insulators [large-gap (Lgap) semiconductors] is called Sgap-KTB-mBJ (Lgap-KTB-mBJ). In Eq. (1) ($c = A + B\bar{g}^e$), c and whence α (c and whence A) are dimensionless parameters, while the dimension of β (B) is $\sqrt{\text{Bohr}}$ ((Bohr) e) to

compensate the dimension of \sqrt{g} (g^e). Here, in this work, since the band gap of our system is not too large, we use Sgap-KBT-mBJ only, i.e., $c = A + Bg$ with ($A = 0.267$, $B = 0.656$ Bohr), as well as TB-mBJ, i.e., $c = \alpha + \beta\sqrt{g}$ with ($\alpha = -0.012$, $\beta = 1.023$ (Bohr) $^{1/2}$). Jishi, Ta, and Sharif by means of the above generalized $c = A + Bg^e$ relation, as proposed by KTB [42], have reparameterized it considering a set of perovskite materials, and obtained A , B , and e parameters to be 0.4, 1.0 (Bohr) $^{1/2}$, and 0.5, where $A = 0.4 > \alpha = -0.012$ but B and e are the same as the original TB-mBJ, viz. $B = 1.0$ (Bohr) $^{1/2} \approx \beta = 1.023$ (Bohr) $^{1/2}$ and $e = 1/2$, see Eq. (5) of Ref. [43]. The TB-mBJ with ($A = 0.4$, $B = 1.0$ (Bohr) $^{1/2}$, $e = 0.5$) is called JTSKTB-mBJ method. Since according to Eqs. (1) and (2) c depends on $\rho(\mathbf{r}')$, the c factor of the TB-mBJ functional is an internal parameter which can be self-consistently converged and determined. This kind of treatment, i.e., TB-mBJ with its self-consistently converged c parameter, is called regular TB-mBJ or simply TB-mBJ, see Ref. [44]. Similarly, KTB-mBJ with its self-consistently converged c parameter, can be called regular KTB-mBJ or simply KTB-mBJ. The same is true for JTSKTB-mBJ, since in this method c is self-consistently converged and determined. A band gap of a system depends on the c parameter and can be increased by increasing this factor, as shown in Fig. 1 of Ref. [41]. During a self-consistent field (SCF) TB-mBJ calculations, the c parameter can be also forced to remain fixed to a desired constant value. This kind of constrained calculations, i.e., TB-mBJ with a fixed c parameter, is called nonregular or irregular TB-mBJ method, see Ref. [44]. The irregular TB-mBJ, as proposed in Ref. [44], is a constrained TB-mBJ method, since in the irregular TB-mBJ (Ir-TB-mBJ) method it is possible to constrain c to a constant (c) value during an SCF calculation. The c factor is a dimensionless parameter which can be varied usually from around 0 or 0.5 to around 2 or 2.5 in an Ir-TB-mBJ calculation, where the interval (0, 2.5) or (0.5, 2) depends on the material under study which would be checked per case, see Fig. 1 of Ref. [41]. Therefore, the band gap can be obtained as a function of c parameter by performing a set of Ir-TB-mBJ calculations. By means of the Ir-TB-mBJ with various c parameters, c can be directly optimized to achieve further improvements over the regular the TB-mBJ method, see magnetic moment discussion of Fe atom, as reported below Table II of Ref. [41]. Therefore, by Ir-TB-mBJ with optimized c (c_{opt}), as introduced in Ref. [40] and used in its Table IV, band gap prediction can be considerably improved.

In summary, the TB-mBJ method refers to the exchange potential expressed in Eq. (1) of Ref. [40], where $c = \alpha + \beta\sqrt{g}$ with ($\alpha = -0.012$, $\beta = 1.023$ (Bohr) $^{1/2}$) for every material. The Lgap-KTB-mBJ method refers to Eq. (1) of Ref. [40], where $c = A + Bg^e$ with ($e = 1$, $A = 0.488$, $B = 0.500$ Bohr) for wide band gap insulators having band gaps larger than or equal 7 eV. The Sgap-KTB-mBJ method refers to Eq. (1) of Ref. [40], where $c = A + Bg^e$ with ($e = 1$, $A = 0.267$, $B = 0.656$ Bohr) for small band gap semiconductors having band gaps smaller than 7 eV. The Lgap-KBT-mBJ can be distinguished from Sgap-KBT-mBJ by the latter band gap of 7 eV which is considered by KBT as the border between small and large gaps, see page 155109-4, second

column, of Ref. [42]. The JTSKTB-mBJ method refers to Eq. (1) of Ref. [40], where $c = A + Bg^e$ with ($A = 0.4$, $B = 1.0$ (Bohr) $^{1/2}$, $e = 0.5$) for perovskite materials. The Ir-TB-mBJ method refers to Eq. (1) of Ref. [40], where c is constrained to a fixed value reigning between 0 to around 2.5. In TB-mBJ, KTB-mBJ, and JTSKTB-mBJ methods, c in Eq. (1) of Ref. [40] is a local functional of $\rho(\mathbf{r}')$. In the latter methods, A , B , and e are three free parameters that can be used to determine an initial value for c . Then, in TB-mBJ, KTB-mBJ, and JTSKTB-mBJ methods, c in Eq. (1) of Ref. [40] is allowed to vary iteration by iteration during an SCF-DFT procedure to reach its converged value. In the Ir-TB-mBJ method, c itself is directly considered as a free parameter. Thus, in the Ir-TB-mBJ method, exchange potential given in Eq. (1) of Ref. [40] itself varies via $\rho(\mathbf{r}')$ during an SCF-DFT procedure cycle by cycle up to the end of well converged SCF procedure, while its c factor from the beginning up to the end of SCF calculation is kept fixed and not allowed to vary.

In order to elucidate to which extent our GGA + U calculations can yield reliable results, in this work, the accuracy of our PBE-GGA + U results are also estimated by the TB-mBJ exchange potential. To this end, we have also calculated the electronic structure for the rhombohedral phase of the pure stoichiometric BiFeO₃ compound using the TB-mBJ, KTB-mBJ, JTSKTB-mBJ, and irregular TB-mBJ with various c parameters, including c_{opt} , as indicated above, in addition to the PBE-GGA + U .

IV. THEORETICAL BACKGROUNDS

Let us, first below in Sec. IV A (Sec. IV B), briefly and theoretically discuss how post processing calculations are performed over the SCF-DFT band structures to obtain optical (spontaneous electric polarization) properties, as discussed in Sec. V B (Sec. V C).

A. Optics

A linear response of a system to an incident light having energy $\hbar\omega$ can be calculated by the complex dielectric function $\varepsilon(\omega)$ using random-phase approximation (RPA) [79]. The results of this kind of calculations were found consistent with experiments [31,39]. Here, we calculate the imaginary part of the dielectric tensor, $\Im[\varepsilon_{\alpha\alpha'}(\omega)]$, using the following formula:

$$\Im[\varepsilon_{\alpha\alpha'}(\omega)] = \left(\frac{e^2 \Omega}{2\pi \hbar m^2 \omega^2} \right) \sum_{cv} \int d\mathbf{k} \langle c\mathbf{k} | p_{\alpha} | v\mathbf{k} \rangle \langle v\mathbf{k} | p_{\alpha'} | c\mathbf{k} \rangle \times f_{c\mathbf{k}} (1 - f_{v\mathbf{k}}) \Delta(E_{c\mathbf{k}} - E_{v\mathbf{k}} - \hbar\omega), \quad (3)$$

where e and m are charge and mass of electron, respectively. Ω is the volume of the unit cell. $\hbar\omega$ is the energy of the incident photon. p_{α} and $p_{\alpha'}$ are the momentum operators where $\alpha = \alpha' = x, y, z$. $|c\mathbf{k}\rangle$ and $|v\mathbf{k}\rangle$ are crystal eigenstates with momentum \mathbf{k} and eigenvalues $E_{c\mathbf{k}}$ and $E_{v\mathbf{k}}$ where c and v indexes refer to the conduction and valence bands, respectively. $f_{c\mathbf{k}}$ and $f_{v\mathbf{k}}$ are the Fermi-Dirac distribution function and $\Delta(E_{c\mathbf{k}} - E_{v\mathbf{k}} - \hbar\omega)$ is the Dirac delta function. The rank of the dielectric tensor is one for the hexagonal and tetragonal symmetries. The dielectric tensor can be decomposed into two

independent components ε_{\parallel} and ε_{\perp} , where $\varepsilon_{\parallel} = \varepsilon_{zz}$ is along the c hexagonal (tetragonal) direction and $\varepsilon_{\perp} = \varepsilon_{xx} = \varepsilon_{yy}$ lies along the other two perpendicular directions. The real part of the dielectric function, $\Re[\varepsilon(\omega)]$, is evaluated from the imaginary part by substituting Eq. (3) into the Kramers-Kronig formula:

$$\Re[\varepsilon(\omega)] = 1 + \frac{2}{\pi} \wp \int_0^{\infty} \frac{d\omega' \omega' \Im[\varepsilon(\omega')]}{\omega'^2 - \omega^2}, \quad (4)$$

where symbol “ \wp ” stands for the Cauchy principle part of the integral. The other optical properties can be straightforwardly obtained from Eqs. (3) and (4). In Sec. VB, we discuss our calculated index of refraction, $N(\omega) = \Re[N(\omega)] + i\Im[N(\omega)] \equiv n(\omega) + ik(\omega)$, where $n(\omega)$ is the index of refraction and $k(\omega)$ is the extinction coefficient. $N(\omega)$ is related to the complex dielectric function as $\varepsilon(\omega) = N^2(\omega)$. If, for simplicity, we represent the dielectric function as $\varepsilon(\omega) = \Re[\varepsilon(\omega)] + i\Im[\varepsilon(\omega)] = \varepsilon_1(\omega) + i\varepsilon_2(\omega)$, then from $\varepsilon(\omega) = N^2(\omega)$, we have $\varepsilon_1(\omega) + i\varepsilon_2(\omega) = n^2(\omega) - k^2(\omega) + 2in(\omega)k(\omega)$. Hence, $\varepsilon_1(\omega) = n^2(\omega) - k^2(\omega)$ and $\varepsilon_2(\omega) = 2n(\omega)k(\omega)$. The latter relations can be solved to obtain the index of refraction n and the extinction coefficient k . In Sec. VB, we substitute Eqs. (3) and (4) into the following formulas to calculate $n(\omega) \equiv \Re[N(\omega)]$ and $k(\omega) \equiv \Im[N(\omega)]$ as follows:

$$n(\omega) \equiv \Re[N(\omega)] = \sqrt{\frac{|\varepsilon(\omega)| + \Re[\varepsilon(\omega)]}{2}}, \quad (5)$$

$$k(\omega) \equiv \Im[N(\omega)] = \sqrt{\frac{|\varepsilon(\omega)| - \Re[\varepsilon(\omega)]}{2}}, \quad (6)$$

where $|\varepsilon(\omega)| = \sqrt{(\Re[\varepsilon(\omega)])^2 + (\Im[\varepsilon(\omega)])^2} \equiv \sqrt{n^2(\omega) + k^2(\omega)}$. Light absorption measurement, as an optical technique, can be used to measure the decay of the light intensity $I(z) = I_0 e^{-\alpha(\omega)z}$ after traversing a thickness z of a material with respect to the initial incident intensity I_0 , where $\alpha(\omega)$ is the absorption coefficient. The intensity $I(z)$ is proportional to the square of the absolute value of the incident field. Thus, the absorption coefficient is proportional to the extinction coefficient as follows, see Eq. (5.2) of Ref. [80]:

$$\alpha(\omega) = \frac{2\omega \Im[N(\omega)]}{c} \equiv \frac{2\omega k(\omega)}{c}, \quad (7)$$

where the factor of 2 originates from $|I(z)|^2$. The extinction coefficient is dimensionless, whereas the unit of absorption coefficient is cm^{-1} . In Sec. VB, we substitute Eq. (6) into Eq. (7) to calculate the absorption coefficient. Then, we calculate the optical gap E_g^{opt} using Tauc method [45], i.e., the following relation between $\alpha(\omega)$, the energy of the incident photon $h\nu$, and E_g^{opt} , see Eq. (1) of Ref. [46]:

$$(\alpha(\omega)h\nu)^{1/\gamma} = B(h\nu - E_g^{\text{opt}}), \quad (8)$$

where h is the Planck constant, ν is the photon's frequency, B is a proportionality constant, and γ is 1/2 for the direct transition and 2 for the indirect transition. The energy-loss function (ELF) is also related to the dielectric function by $\text{ELF}(\omega) = \Im[\frac{-1}{\varepsilon(\omega)}]$ relation. Hence, it reads

$$\text{ELF}(\omega) = \Im\left[\frac{-1}{\varepsilon(\omega)}\right] = \frac{\Im[\varepsilon(\omega)]}{(\Re[\varepsilon(\omega)])^2 + (\Im[\varepsilon(\omega)])^2}. \quad (9)$$

Other optical properties such as reflectivity, transmission, conductivity, polarization coefficient, and so on can be also derived from Eqs. (3) and (4). More details are discussed and presented in Refs. [81–83].

B. Spontaneous electric polarization

According to the modern theory of polarization [34–38], the total microscopic polarization of structure λ can be defined as follows:

$$\mathbf{P}^{(\lambda)} = \frac{e}{\Omega^{(\lambda)}} \sum_{s=1}^N Z_s^{\text{ion}(\lambda)} \mathbf{r}_s^{(\lambda)} + \frac{2e}{(2\pi)^3} \sum_{n=1}^M \int_{1\text{BZ}^{(\lambda)}} d\mathbf{k} \langle u_{n\mathbf{k}}^{(\lambda)} | -i\nabla_{\mathbf{k}} | u_{n,\mathbf{k}}^{(\lambda)} \rangle, \quad (10)$$

where λ can be 1 or 2. Here $\lambda = 1$ ($\lambda = 2$) refers to the initial high-symmetry (final polar low-symmetry) structure which is the cubic (tetragonal) structure in our study. In this equation, e is the electron charge, $\Omega^{(\lambda)}$ is the unit cell volume of the structure λ , s is an index to numerate number of ions in the unit cell, and N is the number of ions. In the first term of this equation, $Z_s^{\text{ion}(\lambda)}$ is the ionic number in the unit cell of the phase, i.e., the number of valence electrons of the atom in the structure λ so that $eZ_s^{\text{ion}(\lambda)}$ is the positive point charge of the atom in the unit cell. $\mathbf{r}_s^{(\lambda)}$ is the position vector of atom s in structure λ . The factor of 2 in the numerator of the second term shows the band occupancy for the spin polarized systems in the absence of the SOC. However, it is worth to highlight that the latter factor should not be considered in the presence of the SOC, because this relativistic interaction itself couples spins up and down states. Therefore, in practice, we have ignored this factor of 2 in Eq. (10) to avoid double counting, since our spin polarized calculations have been performed in the presence of the SOC and whence the up and down electric polarizations have been already mixed together by default using this relativistic coupling. n is the band index, M is the number of occupied bands, \mathbf{k} is the wave vector, $u_{n\mathbf{k}}^{(\lambda)}$ is the cell-periodic complex amplitude of the Bloch eigenstate in the structure (λ) , $-i\nabla_{\mathbf{k}}$ is the momentum representation of the position vector \mathbf{r} , and $\langle u_{n\mathbf{k}}^{(\lambda)} | -i\nabla_{\mathbf{k}} | u_{n,\mathbf{k}}^{(\lambda)} \rangle$ is the electronic contribution of the band n at the wave vector \mathbf{k} in the λ phase to the Berry phase, i.e., $\varphi_{el,n}^{(\lambda)}(\mathbf{k})$, or gauge potential. The first (second) term in Eq. (10) refers to the ionic (electronic) part of the polarization. The integral in the second term is taken over the first Brillouin zone of the λ structure ($1\text{BZ}^{(\lambda)}$) and gives the electronic Berry phase of band n for the λ phase, $\varphi_{el,n}^{(\lambda)}$. The summation in the second term is taken over the bands and therefore, it is proportional to the electronic Berry phase of the λ structure, viz. $\varphi_{el}^{(\lambda)}$. Similarly, the summation in the first term is proportional to the ionic Berry phase of the λ structure, i.e., $\varphi_{ion}^{(\lambda)}$, so that Eq. (10) for polarization in μ cartesian direction can be represented as

$$P_{\mu}^{(\lambda)} = \frac{e}{2\pi} \frac{\varphi_{\mu}^{(\lambda)}}{\Omega^{(\lambda)}} R_{\mu}^{(\lambda)}, \quad (11)$$

where $\varphi_{\mu}^{(\lambda)}$ is the total Berry phase in the polarization direction and $R_{\mu}^{(\lambda)}$ is the length of lattice vector in the real space for the

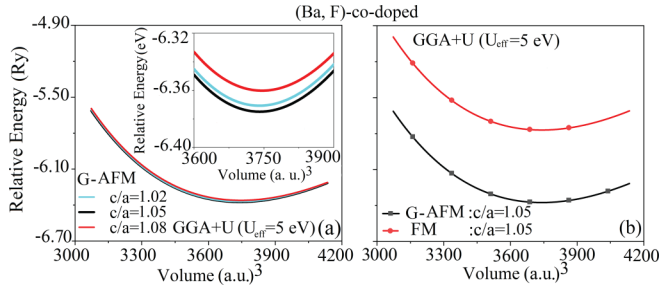


FIG. 2. Relative changes in total energies with respect to the origin of the energy coordinate chosen at $-315\,600$ Ry calculated by PBE-GGA + U + SOC with $U_{\text{eff}} = 5$ eV for the (Ba,F)-codoped composition as functions of volume per formula unit for (a) the G-AFM configuration using three different c/a ratios, and (b) both the G-AFM and FM spin configurations using the optimized c/a ratio obtained from (a). The inset shows (a) after zooming in for higher resolution.

structure λ , viz. $\mathbf{R}^{(\lambda)} = \sum_{\mu=1}^3 R_{\mu}^{(\lambda)} \hat{e}_{\mu}^{(\lambda)}$, where $R_{\mu}^{(\lambda)} \hat{e}_{\mu}^{(\lambda)}$ ($R_{\mu}^{(\lambda)}$) is the primitive vector of structure λ along μ in the direction of unit vector $\hat{e}_{\mu}^{(\lambda)}$. According to the modern theory of polarization, the spontaneous polarization of a compound $\Delta\mathbf{P}$ is defined as the difference between the polarization of the polar low-symmetry structure and the high-symmetry structure, viz. $\Delta\mathbf{P} = \Delta\mathbf{P}^{(2)} - \Delta\mathbf{P}^{(1)}$ [34–38]. In Sec. V C, we use this definition to calculate the spontaneous electric polarization.

V. RESULTS AND DISCUSSIONS

A. Structural and electronic properties

1. Lattice parameters

Let us, here, in this section check that which of the cases in question can be suitable candidates for the ferroelectricity. To this end, we calculate relative changes in total energies with respect to the origin of the energy coordinate chosen at $-315\,600$ Ry as functions of volume per formula unit using PBE + GGA + U with $U_{\text{eff}} = 5$ eV for three ratios $c/a = 1.02, 1.05, 1.08$ of the codoped compound with $x = 0.25$, see Figs. 1(b2) and 2(a). Two of these three selected ratios, i.e., $c/a = 1.05$ and 1.08 , were reported experimentally by Oliver *et al.* [26] for $x = 0.3$ and 0.2 , respectively. The lowest energy state is observed for $c/a = 1.05$, see Fig. 2(a) and also its inset which is rescaled for more clarity. Therefore, we select 1.05 as our optimized c/a ratio for the oxyfluoride composition. Then, we calculate the lattice parameter a using the latter c/a . Similarly, the lattice parameters a and c/a ratios are optimized for the pure and Ba doped cases, as tabulated in Table II. In this table, experimental [15] and theoretical [84] data for the pure case and experimental data [26] for the doped cases with $x = 0.2$ and 0.3 are included for comparison. The comparison shows good agreement. For the pure (doped) compound (compositions), in addition to the optimized $U_{\text{eff}} = 4$ eV ($U_{\text{eff}} = 5$ eV), the results calculated by $U_{\text{eff}} = 5$ eV ($U_{\text{eff}} = 4$ eV) are also included. The comparison shows that lattice parameters are not very sensitive to this change made in U_{eff} . This is in agreement with our observations for the highly correlated CeIn_3 case [71,71]. It is worth to mention that for the optimization only lattice parameters

TABLE II. Lattice parameter a in Å and c/a ratio calculated by PBE-GGA + U + SOC for the rhombohedral BiFeO_3 , tetragonal $\text{Bi}_{1-x}\text{Ba}_x\text{FeO}_{3-x/2}$ ($x = 0.25$) and $\text{Bi}_{1-x}\text{Ba}_x\text{FeO}_{3-x}\text{F}_x$ ($x = 0.25$) compounds together with the available experimental and computational results for comparison. The present results are denoted by *. To avoid repetition, every blank cell of each block of the table, excluding irrelevant cells assigned to the experimental data, represents the repetition of its own upper cell in the table.

Crystal	x	Scheme	U_{eff} (eV)	a (Å)	c/a	Ref.
BiFeO_3	— ^a	PBE+U	4	5.625	2.510	*
			5	5.628	2.509	*
			3 ^b	5.631	2.502	[84]
		Exp.		5.571	2.490	[15]
$\text{Bi}_{1-x}\text{Ba}_x\text{FeO}_{3-x/2}$	0.25	PBE+U	4	4.089	1.003	*
			5	4.096		*
	0.20	Exp.		3.985	1.000	[26]
	0.30	Exp.		3.996	1.003	[26]
$\text{Bi}_{1-x}\text{Ba}_x\text{FeO}_{3-x}\text{F}_x$	0.25	PBE+U	4	3.988	1.050	*
			5	4.053		*
	0.20	Exp.		3.928		[26]
	0.30	Exp.		3.962	1.080	[26]

^aThe math symbol “—” stands for “not presented.”

^bIn Ref. [84], the Hubbard parameter $U = 4$ eV and the exchange interaction. $J = 1$ eV $\Rightarrow U_{\text{eff}} = U - J = 4 - 1 = 3$ eV.

are not considered. To optimize the U_{eff} parameter, a variety of more sensitive quantities with respect to the variation of the Hubbard parameter, including magnetic moments and band gaps, are taken into account. We have also made sure that the doped cases remain insulator after doping.

Let us terminate this section by highlighting the following fact deduced from the above results. Although the Ba-doped composition, due to its tiny polar distortion c/a of around 1.003 leading to the cubic or more precisely pseudocubic symmetry, cannot be an appropriate ferroelectric material, the pure compound with hexagonality c/a of about 2.5 and (Ba,F)-codoped composition with tetragonality c/a of about 1.05 can properly constitute ferroelectric materials.

2. Magnetic moments

A weak ferromagnetism was reported experimentally [85] for Ba doped BiFeO_3 . However, Oliver *et al.* explored G-AFM ordering for Ba doped BiFeO_3 and attributed the remanent magnetization to the ferrimagnetic impurity $\text{BiFe}_{12}\text{O}_{19}$ in this doped compound [26]. Therefore, for the optimized $c/a = 1.05$, we compare the energies versus volume of FM and G-AFM spin configurations. The total energy of FM configuration is about 0.4 Ry ≈ 5.4 eV higher than that of G-AFM configuration, see Fig. 2(b). Thus, we found that the G-AFM configuration can be energetically more favorable than FM configuration which is consistent with the G-AFM ordering reported experimentally by Oliver *et al.* [26].

Here, let us show that GGA + U can also reproduce the experimental magnetic moments per each Fe atom in the pure and doped cases. Accordingly, in agreement with the corresponding experimental magnetic moment of $4.1 \mu_B$ [51], we have calculated the magnetic moment to be 4.11 (4.17) μ_B

by PBE-GGA + U with $U_{\text{eff}} = 4(5)$ eV for the pure compound. In addition to the pure case, the averages of magnetic moments are calculated for the Ba-doped and (Ba,F)-codoped compositions with $x = 0.25$ by PBE-GGA + U with $U_{\text{eff}} = 4(5)$ eV to be about $3.71(3.80) \mu_B$ and $3.60(3.62) \mu_B$, respectively. These results are also found in agreement with the corresponding experimental data [26], i.e., $3.74(3.70) \mu_B$ for the Ba-doped composition with $x = 0.2(0.3)$ and overall $3.70 \mu_B$ for the (Ba,F)-codoped composition considering both $x = 0.2$ and 0.3 . The results show that the magnetic moment decreases as U_{eff} increases in all the three cases. This confirms that the localization degree of the d electrons of iron ion increases as U_{eff} increases in these cases. This is in agreement with our previous observation for the CeIn_3 [71], as well. We also notice that the magnetic moment decreases by doping. For instance, magnetic moment of the single doped composition decreases compared to the pure case. Subsequently, magnetic moment of the codoped composition also decreases compared to the single doped case. From this, it appears that these kinds of doping cause the d electrons of Fe ion to behave a little bit more like itinerant electrons than localized electrons. We have performed more elaborations and, however, found that the change in the magnetic moment originates mainly from the change in symmetry rather than doping. To this end, for the tetragonal structure before (Ba,F) codoping, we, using PBE-GGA + U with $U_{\text{eff}} = 5$ eV, calculated the magnetic moments to be very close (almost equal) to that calculated for the tetragonal structure after (Ba,F) codoping, i.e., $3.80 \mu_B$. This magnetic moment, $3.80 \mu_B$, obtained for the tetragonal structure before and after (Ba,F) codoping differs from the magnetic moment of $4.11(4.17) \mu_B$ calculated by PBE-GGA + U with $U_{\text{eff}} = 4(5)$ eV for the pure case having different symmetry, i.e., rhombohedral ($R3c$). This shows that symmetry can play more important role than doping for the cases under study.

Before closing this section, let us also assess the accuracy of our magnetic moment calculated by the PBE-GGA + U with $U_{\text{eff}} = 4$ eV, including both the spin polarization, and SOC for the pristine compound. To this end, let us calculate the total magnetic moment per Fe atom for the rhombohedral phase of BiFeO_3 using PBE-GGA + U with various U parameters and a variety of mBJ versions, i.e., TB-mBJ, Sgap-KTB-mBJ, Ir-TB-mBJ, and JTSKTB-mBJ with their various c parameters, as defined and discussed in Sec. III. The results together with the experimental and other theoretical results are presented in Table III for comparison. The comparison shows that the magnetic moment increases by increasing U in PBE-GGA + U as well as c in various versions of TB-mBJ. The results also show that both the PBE-GGA + U with $U_{\text{eff}} = 4$ eV and the original version of the mBJ, i.e., TB-mBJ [40], with its well converged $c = 1.38$ in agreement with each other can successfully reproduce the experimental datum and there are accurate enough for prediction of magnetic moment of this compound.

Let us conclude this section by noting that the doped compositions have already shown one of the degrees of freedom required to being among multiferroic materials, viz. nonzero magnetic moments with G-AFM ordering as shown above. Clearly the Ba-doped composition due to its pseudocubic symmetry, however, cannot satisfy the second degree of free-

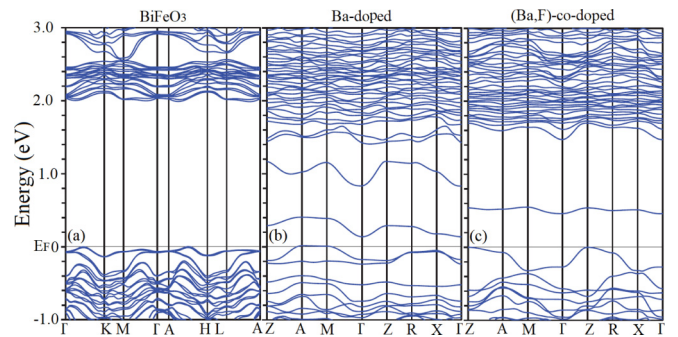


FIG. 3. Band structures calculated by GGA + U + SOC for the (a) pristine BiFeO_3 with $U_{\text{eff}} = 4$ eV, (b) Ba-doped composition, $\text{Bi}_{1-x}\text{Ba}_x\text{FeO}_{3-x/2}$ ($x = 1/4$), with $U_{\text{eff}} = 5$ eV, and (c) (Ba,F)-multidoped composition, $\text{Bi}_{1-x}\text{Ba}_x\text{FeO}_{3-x}\text{F}_x$ ($x = 1/4$), with $U_{\text{eff}} = 5$ eV. The Fermi energy levels (E_F) are set to zero.

dom, viz. the spontaneous electric polarization vanishes in all the cubic crystals. Thus, in Sec. V C, we concentrate only on the (Ba,F)-codoped composition with $P4mm$ symmetry to investigate whether its tetragonal symmetry can allow electric and magnetic polarizations to occur simultaneously.

3. Band structures

Sometimes, in *ab initio* calculations, the presence of impurities in narrow-gap semiconductors can lead to an undesired zero band gap. However, existence of a nonzero band gap plays a vital role in electric polarization calculations, at least using the available standard polarization approaches, as to be performed and discussed in Sec. V C. To this end, let us, here, examine that the effective Hubbard parameter is selected in such a way that it can produce not only satisfactory results compared to the experiment, but can also prevent a possible unwanted metallic behavior of the doped systems. Therefore, in order to check the band gaps and to show the accuracy of our optical properties, as to be discussed in Sec. V B, let us calculate the band structures of BiFeO_3 and its doped tetragonal compositions using PBE-GGA + U . The band structures along high symmetry k-points, as shown in Fig. 3, reveal that the indirect band gap of the pure case, $2.29(1.99)$ eV calculated by PBE-GGA + U with $U_{\text{eff}} = 5$ eV ($U_{\text{eff}} = 4$ eV), substantially reduces by doping. However, the indirect insulator character remains unchanged after doping by PBE-GGA + U with $U_{\text{eff}} = 5$ eV. The reductions of the band gaps originate from the subbands produced by the doped impurities inside the gap region between the valence and conduction bands of the pure case. This observation is consistent with the following reports: (i) Sang Won Bae *et al.* [86] studied nanostructured cubic SrTiO_3 particles and its doped $\text{SrTi}_{0.5}\text{M}_{0.5}\text{O}_3$ ($M = \text{Ru}, \text{Rh}, \text{Ir}, \text{Pt}$) nanoparticles as visible light photocatalysts and found that the doped impurities tailored the band structure of the SrTiO_3 and thence giving a reduction in the band gap compared to the large band gap of SrTiO_3 , (ii) HIRAK KUMAR CHANDRA and coauthors [87] performing pseudopotential calculations using GGA(PW91)+ U as implemented in the VASP code calculated the DOSs of BaTiO_3 introducing Mn-doped with $U = 3$ eV and V-doped with $U = 4$ eV to study the effects of these different dopants on the impurity states inside the band gap, see Fig. 1 of this

TABLE III. Total magnetic moment per Fe atom (MM), electronic bangap (E_g^c), type of electronic band gap (Type), direct optical band gap (dir. E_g^{opt}), and indirect optical band gap (ind. E_g^{opt}) for rhombohedral phase of BiFeO₃. XC, SOC, c , and U_{eff} represent exchange-correlation, spin-orbit coupling, c parameter of various mBJ versions, including TB-mBJ, Sgap-KTB-mBJ, JTSKTB-mBJ, and Ir-TB-mBJ, as defined and discussed in Sec. III, and effective Hubbard parameter of LDA/GGA+ U , respectively. Results of this work are denoted by *.

Scheme	XC	SOC	c	U_{eff} (eV)	MM (μ_B)	E_g^c (eV)	Type	dir. E_g^{opt} (eV)	ind. ^a E_g^{opt} (eV)	Ref.
GGA	PBE	Yes	\neq^b	\neq^b	3.74	0.44	ind.	1.89 ^r	0.32 ^r	*
GGA + U	PBE	Yes	\neq^b	2.0	3.96	1.30	ind.	2.60 ^r	1.22 ^r	*
GGA + U	PBE	Yes	\neq^b	4.0	4.11	1.99	ind.	2.66 ^q	1.86 ^q	*
GGA + U	PBE	Yes	\neq^b	5.0	4.17	2.29	ind.	2.82 ^r	2.00 ^r	*
GGA + U	PBE	Yes	\neq^b	6.0	4.22	2.48	ind.	2.92 ^r	2.29 ^r	*
TB-mBJ	PBE	Yes	1.38	\neq^b	4.10	2.15	ind.	2.80 ^q	2.00 ^q	*
Sgap-KTB-mBJ ^d	PBE	Yes	1.49	\neq^b	4.12	2.28	ind.	2.89 ^r	2.13 ^r	*
Ir-TB-mBJ ^d	PBE	Yes	1.53	\neq^b	4.19	2.62	ind.	3.18 ^r	2.41 ^r	*
Ir-TB-mBJ ^d	PBE	Yes	1.55	\neq^b	4.20	2.67	ind.	3.22 ^r	2.44 ^r	*
Ir-TB-mBJ ^d	PBE	Yes	1.57	\neq^b	4.22	2.73	ind.	3.28 ^r	2.50 ^r	*
Ir-TB-mBJ ^d	PBE	Yes	1.60	\neq^b	4.23	2.81	ind.	3.37 ^r	2.62 ^r	*
JTSKTB-mBJ ^d	PBE	Yes	1.80	\neq^b	4.35	3.33	ind.	4.02 ^r	3.00 ^r	*
LDA	\rightarrow^c	No	\neq^b	\neq^b	\rightarrow^c	0.51	dir.	\rightarrow^c	\rightarrow^c	[100]
LDA	\rightarrow^c	No	\neq^b	\neq^b	3.54	\rightarrow^c	ind.	\rightarrow^c	\rightarrow^c	[100]
LDA	\rightarrow^c	No	\neq^b	\neq^b	3.3	0.4	ind.	\rightarrow^c	\rightarrow^c	[16]
LDA	PW91	No	\neq^b	\neq^b	3.6	0.5	ind.	\rightarrow^c	\rightarrow^c	[109]
GGA	\rightarrow^c	No	\neq^b	\neq^b	\rightarrow^c	0.50	ind.	\rightarrow^c	\rightarrow^c	[57]
GGA	PBE	No	\neq^b	\neq^b	3.9	1.0	ind.	\rightarrow^c	\rightarrow^c	[109]
GGA	PBE	No	\neq^b	\neq^b	\rightarrow^c	1.0	ind.	\rightarrow^c	\rightarrow^c	[110]
GGA	PBE	No	\neq^b	\neq^b	3.7	1.0	ind.	\rightarrow^c	\rightarrow^c	[109]
GGA ⁱ	PBE-HSE06	No	\neq^b	\neq^b	\rightarrow^c	1.94 ^j	ind.	2.14	1.83	[101]
GGA	PBEsol	No	\neq^b	\neq^b	\rightarrow^c	0.99	ind.	\rightarrow^c	\rightarrow^c	[111]
GGA	WC	No	\neq^b	\neq^b	3.8	0.8	ind.	\rightarrow^c	\rightarrow^c	[109]
LDA+ U	\rightarrow^c	No	\neq^b	6.0	\rightarrow^c	2.80(2.40)	dir. (ind.)	\rightarrow^c	\rightarrow^c	[33]
LDA+ U	\rightarrow^c	No	\neq^b	3.8	4.1	2.0	ind.	\rightarrow^c	\rightarrow^c	[109]
LDA+ U	\rightarrow^c	No	\neq^b	2	3.8	1.3	ind.	\rightarrow^c	\rightarrow^c	[16]
LDA+ U	\rightarrow^c	No	\neq^b	4	4	1.9	ind.	\rightarrow^c	\rightarrow^c	[16]
LDA+ U	\rightarrow^c	No	\neq^b	5.5	\rightarrow^c	2.10	\rightarrow^c	\rightarrow^c	\rightarrow^c	[104]
GGA + U	\rightarrow^c	No	\neq^b	2.0	4.02	\rightarrow^c	\rightarrow^c	\rightarrow^c	\rightarrow^c	[88]
GGA + U	\rightarrow^c	No	\neq^b	2.0	4.30	\rightarrow^c	ind.	\rightarrow^c	\rightarrow^c	[49]
GGA + U	\rightarrow^c	No	\neq^b	4.5	\rightarrow^c	2.1	ind.	\rightarrow^c	\rightarrow^c	[105]
TB-mBJ ^f	\rightarrow^c	No	\rightarrow^c	\neq^b	\rightarrow^c	2.50 (1.60 ^e)	dir.	\rightarrow^c	\rightarrow^c	[57]
TB-mBJ	\rightarrow^c	Yes	\rightarrow^c	\neq^b	\rightarrow^c	1.60	ind.	\rightarrow^c	\rightarrow^c	[112]
TB-mBJ	\rightarrow^c	Yes	\rightarrow^c	\neq^b	\rightarrow^c	1.92	ind.	\rightarrow^c	\rightarrow^c	[113]
TB-mBJ	\rightarrow^c	No	\rightarrow^c	\neq^b	\rightarrow^c	1.70	ind.	\rightarrow^c	\rightarrow^c	[112]
TB-mBJ	\rightarrow^c	No	\rightarrow^c	\neq^b	\rightarrow^c	1.96	ind.	\rightarrow^c	\rightarrow^c	[113]
TB-mBJ	\rightarrow^c	No	PBEsol	\neq^b	\rightarrow^c	2.46	ind.	\rightarrow^c	\rightarrow^c	[111]
i-TB-mBJ ^h	PBEsol	No	\rightarrow^c	\neq^b	\rightarrow^c	2.84	dir.	\rightarrow^c	\rightarrow^c	[111]
Hybrid	B3LYP	No	\neq^b	\neq^b	4.2	3.6	ind.	\rightarrow^c	\rightarrow^c	[109]
Hybrid	B1-WC	No	\neq^b	\neq^b	4.2	3.0	ind.	\rightarrow^c	\rightarrow^c	[109]
Hybrid	B1-WC	No	\neq^b	\neq^b	4.2	3.0	ind.	\rightarrow^c	\rightarrow^c	[110]
Hybrid	HSE	No	\neq^b	\neq^b	4.1	3.4	ind.	\rightarrow^c	\rightarrow^c	[110]
sX ^g	\rightarrow^c	No	\neq^b	\neq^b	\rightarrow^c	2.8	ind.	\rightarrow^c	\rightarrow^c	[114]
Exp.								2.10	1.92	[101]
					3.75					[115]
					4.10					[51]
								2.67 ^k		[116]
								2.74 ^l		[39]
								2.50		[102]
						0.90 \pm 0.5	\rightarrow^c			[100]
						1.30	\rightarrow^c			[99]
								2.00 ^m		[103]
								1.85 ⁿ		[104]
								2.25 ^p		[104]
								2.10 ^p		[105]

TABLE III. (Continued.)

Scheme	XC	SOC	c	U_{eff} (eV)	MM (μ_B)	E_g^e (eV)	Type	dir. E_g^{opt} (eV)	ind. ^a E_g^{opt} (eV)	Ref.
								2.74 ^o	2.18 ^o	[31]
								2.35 \rightarrow 1.70 ^s		[106]
								2.25 \rightarrow 1.40 ^t		[106]
								2.09 \rightarrow 2.32 ^u		[107]
								3.0		[108]

^aIndirect transitions in RPA are forbidden according to the Fermi's golden rule due to the momentum conservation law, $\Delta\mathbf{k} = 0$, in the absence of phonon interactions, as discussed in Sec. VB, see also Refs. [117–119], though it can be estimated using Tauc method [45], employing Eqs. (7) and (8).

^bMath symbol “ \nexists ” stands for “does not exist”.

^cMath symbol “–” stands for “not presented”.

^dSee second and third paragraphs of Sec. III for the discussion of this version of mBJ-based scheme and its corresponding c parameter.

^eCalculated for BiFeO₃ thin films.

^fUsing GGA.

^gsX potential is a DFT method based on Hartree-Fock, including electron exchange via Thomas-Fermi screened exchange term, as used by the pseudopotential-based CASTEP code.

^hi-TB-mBJ defined in Ref. [111] is identical to Sgap-KTB-mBJ defined, here, in Sec. III.

ⁱPBE-GGA using Heyd–Scuseria–Ernzerhof (HSE06) hybrid functional as implemented in the VASP code.

^jExtracted from Fig. 6 of Ref. [101].

^kMeasured for BiFeO₃ thin films at 300 K.

^lMeasured for BiFeO₃ thin films.

^mExtracted from Fig. III of Ref. [103].

ⁿUsing absorbance measurement.

^oExtracted, as shown in Fig. 14 and discussed in Sec. VB, using Eqs. (7) and (8), as expressed and discussed in Sec. IV A, from experimental k_a spectrum, as shown in Fig. 3(b) of Ref. [31].

^pUsing reflectance measurement.

^qExtracted, as shown in Fig. 14 and discussed in Sec. VB, using Eqs. (7) and (8), as expressed and discussed in Sec. IV A, from our calculated k_{\perp} spectrum, e.g., see Fig. 10(c).

^rExtracted using Eqs. (7) and (8), as expressed and discussed in Sec. IV A, from our calculated k_{\perp} spectrum.

^sMeasured by conventional absorption spectroscopy from 297.77 to 800.03 K.

^tMeasured with fixed wavelength using the Urbach equation by slowly varying temperature from 369.85 to 1074.80 K.

^uMeasured for BiFeO₃ nano-crystals from (5 nm, 623 K) to (65 nm, 823 K), see Table 1 of Ref. [107].

reference, (iii) Ayana Ghosh *et al.* [88] using first-principles calculations have recently calculated the band structures of BiFeO₃ compounds and its doped BiLaFe₂O₆ and BiSrFe₂O₆ compositions and found that the band gap of BiFeO₃ is reduced by La doping whereas vanished by Sr doping driving the system to be metallic, as can be clearly seen in the band structures shown in Fig. 2 of this reference, (iv) Manpreet Kaur *et al.* experimentally measured a decrease of band gap with increasing concentration of Ba impurity in BiFeO₃ [89], (v) Manjula *et al.* also reported a decrease in band gap with increasing Ba concentration measuring reflectance spectra [90], (vi) Essosimna Djatoubai and coworkers [91] very recently tuned the electronic structure of BiFeO₃ via band gap engineering by Ti-dopants and oxygen vacancies for efficient photocatalytic water oxidation, and (vii) Chan-Ho Yang *et al.* [92] by comprehensively reviewing A-site (Bi-site), B-site (Fe-site), and O-site substitution of BiFeO₃ and giving specific examples for each case discussed the effects of doping on the electronic structure of the BiFeO₃ and confirmed that the midgap states could be partially filled by band filling control and even charge trapping in an electric field. Furthermore, our results also show that the indirect band gap of the oxyfluoride composition, 0.46 eV, is larger than that of the oxide composition, 0.14 eV. The band gaps can be more improved by the advanced modern techniques such as TB-mBJ [40,42],

Green function (*GW*) [93–95], DFT plus dynamical mean field theory (DFT + DMFT) [70,96], and GGA-1/2 [97,98] methods. The latter method, GGA-1/2, can be applied as the starting point for G_0W_0 which may be more successful for band gap calculations of some cases. Here, in this work, in addition to the GGA + U with $U_{\text{eff}} = 4$ eV, different versions of the mBJ methods, as discussed in Sec. III, are used to improve the band gap of the pure case. To this end, besides the original version of mBJ, i.e., TB-mBJ [40], its other versions such as KTB-mBJ [41], Sgap-KTB-mBJ [42], JTSKTB-mBJ [43], and Ir-TB-mBJ [41,44] are also used.

Before concluding this section, let us also estimate the accuracy of our band gap calculated by the PBE-GGA + U with $U_{\text{eff}} = 4$ eV, including both the spin polarization, and SOC for the pure case. To this end, let us calculate the band gap for the rhombohedral phase of BiFeO₃ using PBE-GGA + U with various U parameters and a variety of mBJ versions, i.e., TB-mBJ, Sgap-KTB-mBJ, JTSKTB-mBJ, and Ir-TB-mBJ with their various c parameters, as defined and discussed in Sec. III. The results together with the experimental and other theoretical results are presented in Table III for comparison. The first thing that is worth paying attention to in this table is an apparent self-discrepancy between experimental electronic band gaps (optical gaps) already measured ranging from $(0.90 \text{ eV} \pm 0.50)_{\text{min}} \approx 0.40$ to 1.30 eV (1.85 to 3.00 eV) for

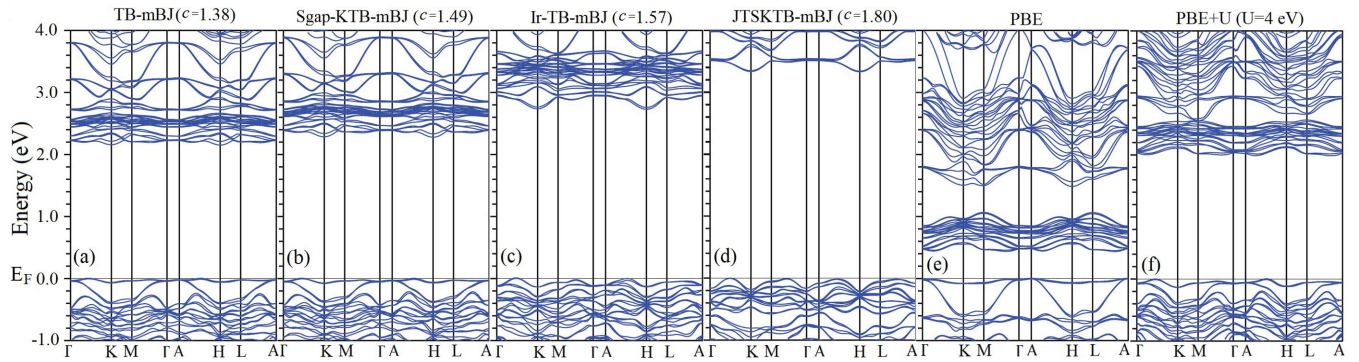


FIG. 4. Band structures calculated by (a) TB-mBJ, (b) Sgap-KTB-mBJ, (c) Ir-TB-mBJ, (d) JTSKTB-mBJ methods for the rhombohedral phase of BiFeO_3 , respectively. The latter methods are defined and discussed in Sec. III. The corresponding c parameter of each method is also indicated. The c parameters of the TB-mBJ, Sgap-KTB-mBJ, and JTSKTB-mBJ are self-consistently obtained, while the c_{opt} parameter of the constrained Ir-TB-mBJ method is so optimized to reproduce a band gap of 2.73 eV. (e) PBE-GGA, and (f) PBE-GGA + U with $U_{\text{eff}} = 4$ eV are also included for comparison. All the Fermi levels are set to zero.

this material, as reported in Refs. [99,100] (Refs. [31,39,99–108]) and tabulated in Table III. For instance, J. F. Ihlefeld *et al.* [39] experimentally measured a direct optical gap of 2.74 eV for the stoichiometric as well as 5% bismuth-deficient single-phase BiFeO_3 thin-films deposited on the (001) SiTiO_3 substrate. As another example, Kevin A. McDonnell *et al.* [101] measured direct and indirect optical gaps to be 2.10 and 1.92 eV for the BiFeO_3 crystal, respectively. The electronic band gap was measured by Higuchi *et al.* to be 0.9 eV with an uncertainty of 0.50 eV [99]. They [99] compared their measured electronic band gap with the optical gap measured by J. F. Ihlefeld *et al.* [39], and related the discrepancy to the difference of electron correlation energy between thin films and ceramic sample used due to the valence fluctuations of Fe ions (Fe^{2+} or Fe^{3+}), creating oxygen vacancies for charge compensation. Makuła, Pacia, and Macyk in a letter entitled “How To Correctly Determine the Band Gap Energy of Modified Semiconductor Photocatalysts Based on UV-Vis Spectra” [46] discuss that in some cases the well known Tauc method [45], as frequently used to obtain direct and indirect optical gaps from an experimental or theoretical absorption spectrum, can lead to inaccurate band gap, and thereby proposed a method to obtain more accurate band gap. In Sec. VB, to apply Tauc approach [45] on our calculated absorption spectra, we will also use the latter method to obtain more reliable optical gaps of the pure system, see Table 1 and Figs. 1 to 4 of Ref. [46]. Anyway, the discrepancies between experimental band gaps can originate from other sources. For example, the differences between the results of band gap measurements can be attributed to the purity or concentration of defects. The other sources of the differences may originate from different methods of measurements, preparation techniques of the materials, the effects of thin-films preparation, the sizes of the nanoparticles, the crystallographic direction of the crystal growth, the effects of different substrates, thickness of the thin-films, optical gap or electronic band gap, and so on. Furthermore, A. F. Lima [33] also recently reviewed this issue and discussed that the measured band gaps can vary from 0.9 to 2.7 eV depending on the experimental techniques and forms of the material. The second thing that is worth paying attention to in this table is an apparent self-inconsistency between theoretical

band gaps already calculated ranging from 0.50 to 2.80 eV for this material, as reported in Refs. [16,33,49,57,88,100,101,104,105,109–114] and tabulated in Table III. The differences between the results of band gap calculations can be attributed to the computational methods, and whether the calculations are performed for the bulk or thin-films of the material in question, as well as mainly the functionals used for the exchange-correlation term. The latter point is also in agreement with our band gaps calculated ranging from 0.44 to 3.50 eV by various schemes, as tabulated in Table III. A comparison shows that the band gap increases by increasing U_{eff} in PBE-GGA + U . The band structures calculated by the TB-mBJ, Sgap-KTB-mBJ, Ir-TB-mBJ, and JTSKTB-mBJ, including their corresponding c parameter, as defined and discussed in Sec. III, are shown in Fig. 4. In this figure, band structures calculated by PBE-GGA and PBE-GGA + U with $U_{\text{eff}} = 4$ eV are also included for comparison. The band structures, as presented in Figs. 4(a) to 4(d), show that the band gap increases as the c parameter of the mBJ-based methods increases, see also Table III. In this sense, the role of c parameter in mBJ can be comparable with that of U parameter in LDA/GGA + U , though they are physically and conceptually different. The results, as tabulated in Table III, show a reasonable agreement between the band gaps predicted by original TB-mBJ using its self-consistently converged $c = 1.38$ and PBE-GGA + U using $U_{\text{eff}} = 4$ eV. This nearly band gap agreement can be also seen by comparing band structure calculated by PBE-GGA + U with $U_{\text{eff}} = 4$ eV, as shown in Fig. 4(f), with the band structure calculated by TB-mBJ with $c = 1.38$, as shown in Fig. 4(a). Moreover, the valence bands of these two band structures show almost similar behaviors, see valence bands shown in Figs. 4(a) and 4(f). Despite the band gap agreement and the similarity of the valence bands, the curvatures of the conduction bands of the latter figures show a little bit deviation with respect to each other and with that of PBE-GGA band structure, see the bunch of conduction bands which is closer to the Fermi level shown in Fig. 4(a) and compare it with those of shown in Figs. 4(f) and 4(e). The bunch of conduction bands is more compressed by the TB-mBJ potential than that by the PBE-GGA + U compared to the initial bunch of the

conduction bands generated by the PBE-GGA without U and c parameters, see Figs. 4(a), 4(e) and 4(f). The comparison shows that both of the TB-mBJ and PBE-GGA + U shift up the GGA conduction bands. However, the nature or curvature of the bunch of conduction bands nearly remains unchanged by the PBE-GGA + U even after pushing up the PBE-GGA conduction bands, whereas it is somehow changed by the repulsion potential TB-mBJ. Although the ground state physical properties are mainly determined by the valence bands, the conduction bands are also important and can affect the results. This implies that band structure calculated by PBE-GGA + U with $U_{\text{eff}} = 4$ eV is approximately close (but not exactly identical) to that calculated by TB-mBJ with $c = 1.38$ for the pure case. This agreement, regardless of the differences observed between conduction bands, becomes more important, if we recall that the latter two methods are the same methods that were also able to predict the magnetic moment well before in Sec. V A 2. The third thing that is worth paying attention to in this table is that the “electronic band gap” would be distinguished from the “optical gap.” The electronic band gap (E_g^e) is defined as $E_g^e = E_{\text{CBM}} - E_{\text{VBM}}$, where E_{CBM} is the energy of the conduction band minimum (CBM) and E_{VBM} is the energy of the valence band maximum (VBM). According to this definition, E_g^e is a single-valued quantity for a given crystal, which is not the case for the optical gap, as to be discussed in Sec. V B. Therefore, E_g^e can be either direct or indirect, but not both at the same time, unless the values of the direct and indirect electronic band gaps are the same so that E_g^e remains single-valued. This is also not the case for the optical gap, as to be discussed in Sec. V B. It is noticeable that in spite of the single-valued characteristic of the electronic band gap, sometimes two different values with two different direct and indirect types have been reported for electronic band gaps of a crystal using its unique band structure. This has been performed usually when the two values of the electronic band gaps are very close to each other. Reporting two different band gaps close to each other using a single band structure may be considered as an approximation. However, this cannot be completely correct, since it violates the single-valued characteristic and whence the definition of the electronic band gap. The “optical gap” (E_g^{opt}), as to be defined in Sec. V B, differs from the electronic band gap E_g^e , see Table III. The latter point is obvious but it is important, because E_g^e and E_g^{opt} are frequently used instead of or compared with each other, though they are technically and physically two different quantities having apparent similarities. Jean-Luc Bredas [120] considering different types of energy gaps such as band gap, HOMO-LUMO gap, fundamental gap, optical gap, or transport gap has reported that “failure to appreciate the distinctions among these different energy gaps has caused much confusion in the literature, which is manifested by the frequent use of improper terminology,...” As shown in Table III, large values can be produced for E_g^e theoretically using screened exchange (sX) method, as used in Ref. [114], or JTSKTB-mBJ or “Ir-TB-mBJ with larger c parameters” methods, as used in this work, than those produced by “TB-mBJ using its self-consistently obtained c parameter” or “PBE-GGA + U using its systematically optimized U parameter.” This implies that, in practice, it is possible to force E_g^e to reproduce the

experimental E_g^{opt} , but, in principle, it is nonphysical and unreliable. Since most of the energy gaps reported for this material are optical band gap, let us postpone the gap discussion to Sec. V B where we calculate E_g^{opt} .

Let us close this section by limiting the accuracy of our results for the pure (doped) compound (compositions) to the extend predicted by TB-mBJ and PBE-GGA + U with $U_{\text{eff}} = 4(5)$ eV methods which can reproduce two different quantities, magnetic moment and band gap, consistent with some experimental data approximately.

4. Densities of states

It is well known that stereochemically active lone pair electrons can be responsible for the polarization in bismuth- and lead-based ferroelectrics [121–126]. Thus, here, in order to demonstrate the activity of the lone pair s electrons of Bi atom having electronic configuration [Xe] : $4f^{14} 5d^{10} 6s^2 6p^3$, let us shed light into the total and partial DOSs of the pure (doped) compound (compositions) calculated by GGA + U + SOC with $U_{\text{eff}} = 4$ eV ($U_{\text{eff}} = 5$ eV), as shown in Fig. 5. Total DOS of the pure case, as shown in Fig. 5(a), confirms the band gap reported above based on the corresponding band structure, as shown in Fig. 3(a). Looking at the edges of the total and partial DOSs between the valence and conduction states of the pure compound shows that gap edges mainly originate from s -Bi, p -Bi, d -Fe, and p -O orbitals, see Figs. 5(a)–5(d), respectively. Total DOS of the oxide doped composition, as shown in Fig. 5(e), confirms the reduction of the band gap reported above due to the subbands produced by the Ba impurity, compared to that of the pure compound, based on the corresponding band structure, as shown in Fig. 3(b). Although shifting DOSs down can be almost observed by comparing Figs. 5(a)–5(c), and 5(d) and 5(e), 5(f)–5(h), and 5(i), the last sources of the gap edges, i.e., s -Bi, p -Bi, d -Fe, and p -O orbitals, remain unchanged, see Figs. 5(e), 5(g) 5(f), 5(h), and 5(i). Total DOS of the oxyfluoride doped composition, as shown in Fig. 5(j), confirms the increase (decrease) of the band gap reported above due to the subbands produced by the oxyfluoride impurity, compared to that of the oxide (pure) composition (compound), based on the corresponding band structure, as shown in Fig. 3(c). In analogy to the oxide system, here also, for the oxyfluoride composition, we see that the DOSs are shifting down compared to the pure case, and again s -Bi, p -Bi, d -Fe, and p -O orbitals constitute the roots of the gap edges, see Figs. 5(j), 5(k), 5(l), 5(m), 5(n), and 5(o). For more clarity, the total DOSs of Ba-doped (codoped) compound from -0.5 to 1.5 eV energy ranges are shown in Fig. 6. The three peaks are located at 0.28 , 1.04 , and -0.13 eV for single doped, see Fig. 6(a). For the codoped, we see two small peaks at -0.09 and -0.26 eV in the valence region near the Fermi energy and a peak around 0.51 eV in the conduction region, see Fig. 6(b). The valence s -Bi, p -Bi, p -O, and d -Fe DOSs of the pure compound, as shown in Figs. 5(b) and 5(d), satisfy the hybridization conditions discussed in section 5.4 of our previous work on quantum size effects in Pb/Si(111) thin films [127]. Therefore, the s -Bi, p -Bi, p -O, and d -Fe states of the pristine compound can hybridize with each other, consistent with Ref. [126].

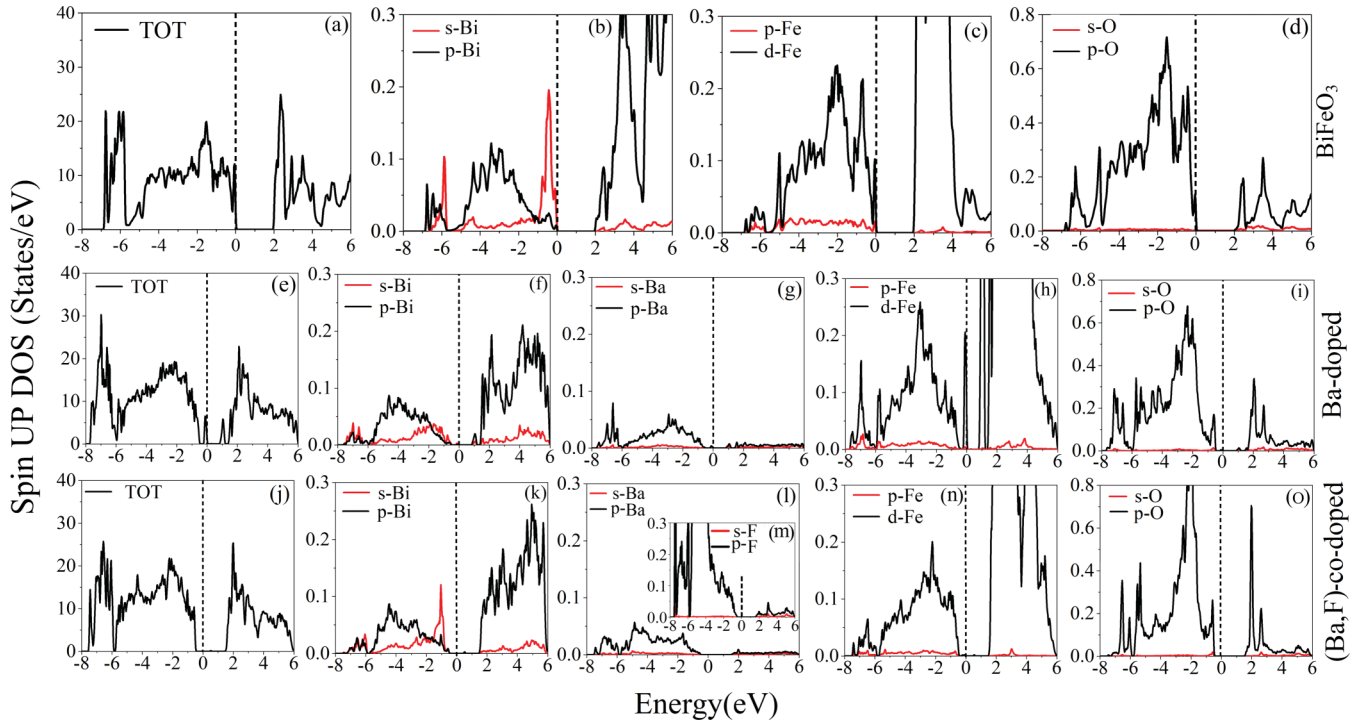


FIG. 5. Projected spins up total and partial DOSs generated by the GGA + U + SOC with $U_{\text{eff}} = 4$ (5) eV for the pure compound (doped compositions). The Fermi energy levels are set to zero.

In order to quantitatively verify the hybridization among s -Bi, p -Bi, d -Fe, and p -O orbitals, we calculate their corresponding occupation numbers for spins up and down (dn), $n_i(\text{up}, \text{dn})$ with $i = s, p$, and d , in all the pure and

doped compounds, see Table IV. The results show that the corresponding up and down occupation numbers are equal for each orbital in each compound, i.e., the up and down occupations are completely balanced. This confirms that the AFM calculations are well converged so that the corresponding total up and down DOSs can symmetrically cancel each other in each compound, resulting in a null total magnetic moment for each case, as expected for an AFM configuration. However, this can cause to raise a question that “how this can coexist with magnetic ordering.” To settle this down, let us consider d orbitals of the Fe atoms, as the main magnetic source, of the materials in question. Let us also consider only the pure compound as a convenient

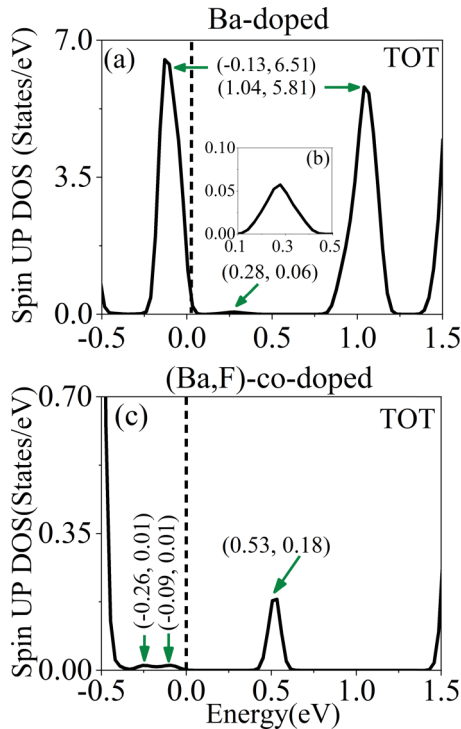


FIG. 6. Spin up total DOSs calculated by the GGA + U + SOC with $U_{\text{eff}} = 5$ eV for doped compositions in energy interval [0.5, 1.5 eV]. The new peaks originated from the doped impurities are shown by arrows indicating their energies and intensities.

TABLE IV. Averages of the occupation numbers for spins up and down [$n_i(\text{up}, \text{dn})$ with $i = s, p$, and d] and the number of atoms (N) for each atom in the unit cells of BiFeO_3 compound, and Ba-doped, as well as (Ba,F)-codoped compositions.

Crystal	Atom	N	$n_s(\text{up}, \text{dn})$	$n_p(\text{up}, \text{dn})$	$n_d(\text{up}, \text{dn})$
BiFeO_3	Bi	6	(0.71, 0.71)	(3.29, 3.29)	(4.92, 4.92)
	Fe	6	(1.08, 1.08)	(3.07, 3.07)	(2.65, 2.65)
	O	18	(0.83, 0.83)	(1.87, 1.87)	
Ba-doped	Bi	6	(0.57, 0.57)	(3.24, 3.24)	(4.81, 4.81)
	Fe	8	(1.05, 1.05)	(3.01, 3.01)	(2.51, 2.51)
	O	23	(0.74, 0.74)	(1.60, 1.60)	
	Ba	2	(0.84, 0.84)	(2.06, 2.06)	(5.03, 5.03)
(Ba,F)-codoped	Bi	6	(0.59, 0.59)	(3.21, 3.21)	(4.81, 4.81)
	Fe	8	(1.01, 1.01)	(2.90, 2.90)	(2.32, 2.32)
	O	22	(0.75, 0.75)	(1.63, 1.63)	
	Ba	2	(0.84, 0.84)	(2.06, 2.06)	(5.03, 5.03)
	F	2	(0.85, 0.85)	(2.14, 2.14)	

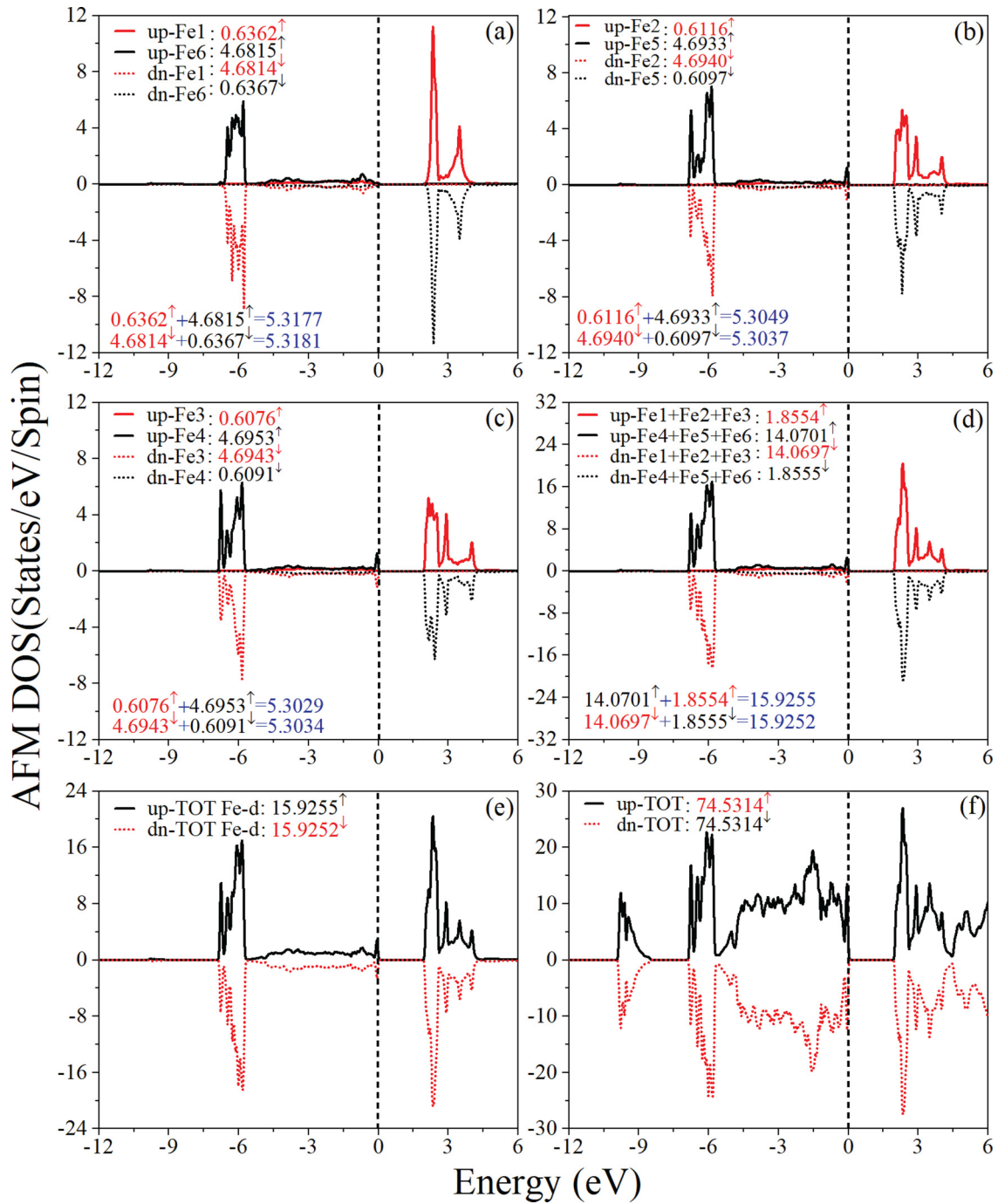


FIG. 7. Spins up and down DOSs calculated by GGA + U + SOC with $U_{\text{eff}} = 4$ eV for the partial d orbitals of the (a) Fe1 and Fe6, (b) Fe2 and Fe5, (c) Fe3 and Fe4, (d) Fe1 + Fe2 + Fe3 and Fe4 + Fe5 + Fe6, and (e) total d orbital of Fe1 + Fe2 + Fe3 + Fe4 + Fe5 + Fe6, as well as (f) total DOS of all the entire atoms and their orbitals inside the unit cell for the AFM phase of the stoichiometric pure BiFeO₃ compound. Occupation numbers per spin, as the areas under the up and down partial and total DOSs, are indicated in each figure. The Fermi level is set to zero.

sample for this purpose. Obviously, similar discussion with the same conclusion could be represented (not shown, here, to avoid repeated discussion) for the other orbitals of the pure compound and doped compositions. To this end, spins up and down DOSs calculated by PBE-GGA + U with $U_{\text{eff}} = 4$ eV are represented in Fig. 7 for the d orbitals of the six Fe atoms of the pure compound both individually and collectively, including occupation numbers per spin channel and their summations. As can be seen from

Fig. 7(a), up- d -Fe1-DOS (up- d -Fe6-DOS) is not balanced by its corresponding dn- d -Fe1-DOS (dn- d -Fe6-DOS), viz. $n_d^{\text{Fe1}}(\text{up}) = 0.6362 \neq n_d^{\text{Fe1}}(\text{dn}) = 4.6814$ ($n_d^{\text{Fe6}}(\text{up}) = 4.6815 \neq n_d^{\text{Fe6}}(\text{dn}) = 0.6367$). This confirms that Fe1 (Fe6) is magnetically ordered individually, viz. $n_d^{\text{Fe1}}(\text{up}) - n_d^{\text{Fe1}}(\text{dn}) = 0.6362 - 4.6814 = -4.0452 \leq 0$ ($n_d^{\text{Fe6}}(\text{up}) - n_d^{\text{Fe6}}(\text{dn}) = 4.6815 - 0.6367 = 4.0448 \geq 0$). However, as can be also seen from the latter figure, up- d -Fe1-DOS

($dn - d$ -Fe1-DOS) is almost well balanced by $dn - d$ -Fe6-DOS (up- d -Fe6-DOS), viz. $n_d^{\text{Fe1}}(\text{up}) = 0.6362 \approx n_d^{\text{Fe6}}(\text{dn}) = 0.6367$ ($n_d^{\text{Fe1}}(\text{dn}) = 4.6814 \approx n_d^{\text{Fe6}}(\text{up}) = 4.6815$). This implies that the resultant magnetic moment of Fe1 and Fe6 atoms collectively are very close to zero, as opposite channels of the Fe1 and Fe6 almost cancel each other, viz. $[n_d^{\text{Fe1}}(\text{up}) + n_d^{\text{Fe6}}(\text{up})] - [n_d^{\text{Fe1}}(\text{dn}) + n_d^{\text{Fe6}}(\text{dn})] = [0.6362 + 4.6815] - [4.6814 + 0.6367] = [5.3177 - 5.3181] = -0.0004 \approx 0$. Similarly, up- d -Fe2-DOS (up- d -Fe5-DOS) is not balanced by its corresponding $dn - d$ -Fe2-DOS ($dn - d$ -Fe5-DOS), viz. $n_d^{\text{Fe2}}(\text{up}) = 0.6116 \neq n_d^{\text{Fe2}}(\text{dn}) = 4.6040$ ($n_d^{\text{Fe5}}(\text{up}) = 4.6933 \neq n_d^{\text{Fe5}}(\text{dn}) = 0.6097$), as shown in Fig. 7(b). This shows that Fe2 (Fe5) is also magnetically ordered individually, viz. $n_d^{\text{Fe2}}(\text{up}) - n_d^{\text{Fe2}}(\text{dn}) = 0.6116 - 4.6940 = -4.0824 \leq 0$ ($n_d^{\text{Fe5}}(\text{up}) - n_d^{\text{Fe5}}(\text{dn}) = 4.6933 - 0.6097 = 4.0836 \geq 0$). Again we notice that, here also, up- d -Fe2-DOS ($dn - d$ -Fe2-DOS) is almost well balanced by $dn - d$ -Fe5-DOS (up- d -Fe5-DOS), viz. $n_d^{\text{Fe2}}(\text{up}) = 0.6116 \approx n_d^{\text{Fe5}}(\text{dn}) = 0.6097$ ($n_d^{\text{Fe2}}(\text{dn}) = 4.6940 \approx n_d^{\text{Fe5}}(\text{up}) = 4.6933$), see Fig. 7(b). Therefore, the resultant magnetic moment of Fe2 and Fe5 atoms collectively are also very close to zero, viz. $[n_d^{\text{Fe2}}(\text{up}) + n_d^{\text{Fe5}}(\text{up})] - [n_d^{\text{Fe2}}(\text{dn}) + n_d^{\text{Fe5}}(\text{dn})] = [0.6116 + 4.6933] - [4.6940 + 0.6097] = [5.3049 - 5.3037] = 0.0012 \approx 0$. In analogous to the above (Fe1, Fe6) and (Fe2, Fe5) pairs, we notice that Fe3 and Fe4 also collectively constitute a symmetric pair, see Fig. 7(c). This figure shows that up- d -Fe3-DOS (up- d -Fe4-DOS) is not balanced by its corresponding $dn - d$ -Fe3-DOS ($dn - d$ -Fe4-DOS), viz. $n_d^{\text{Fe3}}(\text{up}) = 0.6076 \neq n_d^{\text{Fe3}}(\text{dn}) = 4.6943$ ($n_d^{\text{Fe4}}(\text{up}) = 4.6953 \neq n_d^{\text{Fe4}}(\text{dn}) = 0.6091$). Consequently, Fe3 (Fe4) is magnetically ordered individually, viz. $n_d^{\text{Fe3}}(\text{up}) - n_d^{\text{Fe3}}(\text{dn}) = 0.6076 - 4.6943 = -4.0867 \leq 0$ ($n_d^{\text{Fe4}}(\text{up}) - n_d^{\text{Fe4}}(\text{dn}) = 4.6953 - 0.6091 = 4.0862 \geq 0$). However, up- d -Fe3-DOS ($dn - d$ -Fe3-DOS) can be nearly canceled by $dn - d$ -Fe4-DOS (up- d -Fe4-DOS), viz. $n_d^{\text{Fe3}}(\text{up}) = 0.6076 \approx n_d^{\text{Fe4}}(\text{dn}) = 0.6091$ ($n_d^{\text{Fe3}}(\text{dn}) = 4.6943 \approx n_d^{\text{Fe4}}(\text{up}) = 4.6953$). Hence, the resultant magnetic moment of Fe3 and Fe4 atoms together are very close to zero, viz. $[n_d^{\text{Fe3}}(\text{up}) + n_d^{\text{Fe4}}(\text{up})] - [n_d^{\text{Fe3}}(\text{dn}) + n_d^{\text{Fe4}}(\text{dn})] = [0.6076 + 4.6953] - [4.6943 + 0.6091] = [5.3029 - 5.3034] = -0.0005 \approx 0$. Thus, each of the iron atoms alone, Fe i for $i = 1$ to 6, is magnetically ordered, but considering the above three individual doublets, i.e., (Fe i , Fe j) for $(i, j) = (1, 6), (2, 5), (3, 4)$, the magnetizations of these pairs nearly vanish. The values of $[n_d^{\text{Fe}i}(\text{up}) + n_d^{\text{Fe}j}(\text{up})] - [n_d^{\text{Fe}i}(\text{dn}) + n_d^{\text{Fe}j}(\text{dn})]$ are obtained above to be $-0.0004, 0.0012, -0.0005$ for the paired indexes $(i, j) = (1, 6), (2, 5), (3, 4)$, respectively. Although the values $-0.0004, 0.0012, -0.0005$ are very small, their reflections can be observed from their corresponding asymmetric up and down DOSs, as shown in Figs. 7(a), 7(b) and 7(c), respectively. In fact, DOS is very sensitive to even any small changes, as expected from a fundamental quantity that constitutes the foundation upon which the other physical properties are based. To obtain a more symmetric up and down DOSs with respect to each other, we sum the asymmetric DOSs shown in Figs. 7(a), 7(b) and 7(c) and instead of the above three individual doublets obtain only one collective

doublet ($\sum_i \text{Fe}i, \sum_j \text{Fe}j$) for $(i, j) = (1, 6), (2, 5), (3, 4)$, as shown in Fig. 7(d). The collective up and down DOSs are made more symmetric, as qualitatively can be seen from Fig. 7(d), than the individual DOSs shown in Figs. 7(a), 7(b) and 7(c). To quantitatively assess the latter qualitative observation, let us compare occupation numbers of the collective DOSs, as well. As can be seen from Fig. 7(d), up- $d - \sum_i \text{Fe}i$ -DOS ($dn - d - \sum_i \text{Fe}i - \text{DOS}$) is better balanced by $dn - d - \sum_j \text{Fe}j - \text{DOS}$ (up- $d - \sum_i \text{Fe}i - \text{DOS}$) for $(i, j) = (1, 6), (2, 5), (3, 4)$, viz. $\sum_i n_d^{\text{Fe}i}(\text{up}) = 1.8554 \approx \sum_j n_d^{\text{Fe}j}(\text{dn}) = 1.8555$ ($\sum_i n_d^{\text{Fe}i}(\text{dn}) = 14.0697 \approx \sum_j n_d^{\text{Fe}j}(\text{up}) = 14.0701$). This implies that the resultant magnetic moment of $\sum_i \text{Fe}i$ and $\sum_j \text{Fe}j$ for $(i, j) = (1, 6), (2, 5), (3, 4)$ collectively are made closer to zero, viz. $[\sum_i n_d^{\text{Fe}i}(\text{up}) + \sum_j n_d^{\text{Fe}j}(\text{up})] - [\sum_i n_d^{\text{Fe}i}(\text{dn}) + \sum_j n_d^{\text{Fe}j}(\text{dn})] = [1.8554 + 14.0701] - [14.0697 + 1.8555] = [15.9255 - 15.9252] = 0.0003 \approx 0$. The latter value of 0.0003 is smaller than the absolute values of $-0.0004, 0.0012, -0.0005$, which results in more symmetric collective up and down d -DOSs shown in Fig. 7(d) compared to the individual up and down d -DOSs shown in Figs. 7(a), 7(b) and 7(c). We checked whether more symmetric up and down d -DOSs can be obtained by collecting all the d -Fe DOSs or not. To this end, we sum the up and down DOSs of all the six Fe atoms to obtain total-up and total down d -Fe-DOSs, as shown in Fig. 7(e). The up and down occupation numbers indicated in Fig. 7(e) are found to be the same as those indicated in Fig. 7(e). This shows that better symmetric up and down DOSs or smaller number than 0.0003 within our accuracy cannot be achieved by considering d orbitals of Fe atoms only. Although the orbitals of the other atoms and the other orbitals of the Fe atoms in the unit cell of the pure material in question cannot impose considerable magnetic moments, but if their small values are also considered collectively, well symmetric total up and down DOSs up to the accuracy of our calculations can be obtained for the whole of the unit cell, as can be clearly seen qualitatively from Fig. 7(e). Quantitatively, the total up and down occupation numbers for all the atoms in the whole of the unit cell are also perfectly balanced, i.e., $74.5314 - 74.5314 = 0$, see Fig. 7(e). The occupation number of the up d -orbital for the Fe in Table IV, $n_d^{\text{Fe}}(\text{up}) = 2.65$, is obtained by taking an average over the occupation numbers of the six Fe atoms of the unit cell for the pure compound, viz., $n_d^{\text{Fe}}(\text{up}) = (\sum_{i=1}^6 n_d^{\text{Fe}i}(\text{up}))/6 = (0.6362 + 0.6116 + 0.6076 + 4.6953 + 4.6933 + 4.6815)/6 = 15.9255/6 = 2.65425 \approx 2.65$, where Fe i is the i th Fe atom in the unit cell. Similarly, the occupation number of the down d orbital for the Fe in Table IV, $n_d^{\text{Fe}}(\text{dn}) = 2.65$, is obtained by averaging over the occupation numbers of the 6 Fe atoms of the unit cell for the pure compound, viz., $n_d^{\text{Fe}}(\text{dn}) = (\sum_{i=1}^6 n_d^{\text{Fe}i}(\text{dn}))/6 = (4.6814 + 4.6940 + 4.6943 + 0.6091 + 0.6097 + 0.6367)/6 = 15.9252/6 = 2.6542 \approx 2.65$. As can be clearly seen, although $n_d^{\text{Fe}i}(\text{up})$ differs from $n_d^{\text{Fe}j}(\text{up})$ for every i , the averaged up occupation number $n_d^{\text{Fe}}(\text{up})$ is completely balanced by the averaged down occupation number $n_d^{\text{Fe}}(\text{dn})$, viz., $n_d^{\text{Fe}}(\text{up}) = n_d^{\text{Fe}}(\text{dn}) = 2.65$. For the other averaged occupation numbers tabulated in Table IV

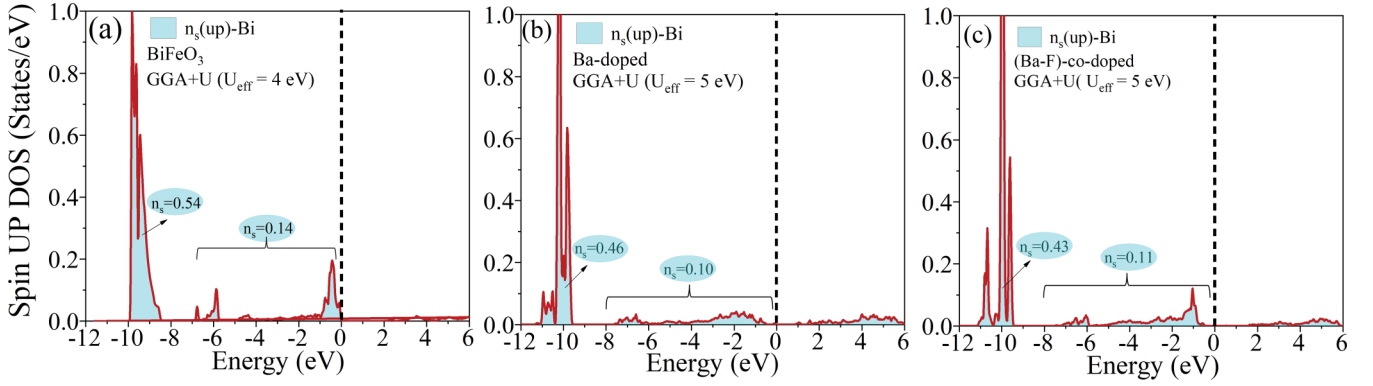


FIG. 8. Spin up partial DOSs calculated by GGA + U + SOC with $U_{\text{eff}} = 4$ (5) eV for the pure compound (doped compositions). Occupation numbers as the area under the partial DOSs are individually indicated for spins up of s -Bi in the (a) pure compound, (b) Ba-doped composition, and (c) codoped composition

similar discussion can be presented, which we avoid to repeat them, here. From the above discussion, the answer to the question is: although Table IV shows that spins up and down channels are completely balanced, iron atoms individually are magnetically ordered and collectively AFM ordering coexists.

The $n_s(\text{up}, \text{dn})$ for Bi atoms in the pure, Ba-doped, and (Ba,F)-codoped compounds are found to be (0.71, 0.71), (0.57, 0.57), and (0.59, 0.59), respectively. Moreover, we observe that the valence s -Bi DOS of the pure case consists of two parts with an energy gap between them. One part containing 0.54 electrons is almost distributed over $(-10, -8.5 \text{ eV})$ and the other part containing 0.14 electrons is distributed over $(-7.0 \text{ eV}, E_F)$, see Fig. 8(a). This is also the case for the doped compositions, see Figs. 8(b) and (c). The deeper (shallower) part of the valence s -Bi DOS for the Ba-doped composition containing 0.46 (0.10) electrons is distributed around $(-11, -9.5 \text{ eV})$ [$(-8.0, E_F)$], which is shifted downwards by approximately 1 eV compared to the pure case, as would be seen from Fig. 8(b) compared to Fig. 8(a). The occupation numbers of the deeper and shallower parts of the valence s -Bi DOS and the amount of the down shift towards deeper energies for the (Ba,F)-codoped composition, as shown in Fig. 8(c), are close to those for the Ba-doped composition, as shown in Fig. 8(b). Despite the latter close proximity, the shapes of both the deeper and shallower s -Bi DOS distributions of the (Ba,F)-codoped composition substantially differ from those of the Ba-doped composition, as would be noticed from Fig. 8(c) in comparison to Fig. 8(b). The partial occupancies, as tabulated in Table IV, show that $n_p(\text{up}, \text{dn})$ of the Bi atoms are (3.29, 3.29), (3.24, 3.24), and (3.21, 3.21) for the pure, Ba-doped and (Ba,F)-codoped compounds, respectively. This indicates that in all the three compounds, the p -Bi

orbitals are overfilled, $n_p(\text{up}) + n_p(\text{dn}) > 6$ electrons. The electronic configuration of the Bi atom outside of the crystalline environments, [Xe] : $4f^{14} 5d^{10} 6s^2 6p^3$, shows that p -Bi containing three electrons is only half-filled. Therefore, p -Bi orbitals of the compounds are so hybridized with the other orbitals that their p orbitals are filled inside the crystals under study. The kinds of p -Bi hybridization with the other states are exhibited in Figs. 5(b), 5(c), and 5(d) for the pure compound, in Figs. 5(f) to 5(i) for the Ba-doped composition, and in Figs. 5(k) to 5(o) for the (Ba,F)-codoped composition. The occupation numbers of the Fe atoms, as presented in Table IV, show that $n_s(\text{up}, \text{dn})$ and $n_p(\text{up}, \text{dn})$ are very close to (1, 1) and (3, 3) in all the three compounds, respectively. The electronic configuration of the Fe atom outside of the crystalline environments, [Ne] : $3s^2 3p^6 3d^6 4s^2$, shows that the occupation numbers of the s - and p -Fe orbitals remain almost unchanged. The $n_d(\text{up}, \text{dn})$ for the Fe atoms of the (Ba,F)-codoped composition (2.32, 2.32) is smaller than that of the Ba-doped composition (2.51, 2.51), which itself is less than that of the pure compound (2.65, 2.65), see Table IV, viz $2.32 < 2.51 < 2.65$. The occupation number of the d -Fe orbitals is reduced from $5^\uparrow + 1^\downarrow = 6$ for the free Fe atom to $2.65^\uparrow + 2.65^\downarrow = 5.30$ for the pure compound, and to $2.51^\uparrow + 2.51^\downarrow = 5.02$ for the Ba-doped composition, as well as to $2.32^\uparrow + 2.32^\downarrow = 4.64$ for the (Ba,F)-codoped composition. In analogous (contrast) to the latter (former) reduction (constant) trend of the d -Fe (s - and p -Fe) orbital (orbitals), a reduction trend can be nearly observed for both the s - and p -orbitals of oxygen atom from free space taking its atomic configuration [He] : $2s^2 2p^4$ into account to the pure and Ba-doped crystalline environment considering the occupation numbers given in Table IV, viz.

$$n_s(\text{up}) + n_s(\text{dn}) = \underbrace{1^\uparrow + 1^\downarrow = 2}_{\text{free O atom}} > \underbrace{0.83^\uparrow + 0.83^\downarrow = 1.66}_{\text{pure compound}} > \underbrace{0.74^\uparrow + 0.74^\downarrow = 1.48}_{\text{Ba-doped composition}}$$

and

$$n_p(\text{up}) + n_p(\text{dn}) = \underbrace{3^\uparrow + 1^\downarrow = 4}_{\text{free O atom}} > \underbrace{1.87^\uparrow + 1.87^\downarrow = 3.74}_{\text{pure compound}} > \underbrace{1.60^\uparrow + 1.60^\downarrow = 3.20}_{\text{Ba-doped composition}}$$

This reduction trend of the occupation numbers of the s - and p -O orbitals, as can be seen from Table IV, is stopped or more precisely reversed to a very small extent from Ba-doped to (Ba,F)-codoped composition, viz.

$$n_s(\text{up}) + n_s(\text{dn}) = \underbrace{0.74^\uparrow + 0.74^\downarrow = 1.48}_{\text{Ba-doped composition}} < \underbrace{0.75^\uparrow + 0.75^\downarrow = 1.50}_{\text{(Ba,F)-codoped composition}}$$

and

$$n_p(\text{up}) + n_p(\text{dn}) = \underbrace{1.60^\uparrow + 1.60^\downarrow = 3.20}_{\text{Ba-doped composition}} < \underbrace{1.63^\uparrow + 1.63^\downarrow = 3.26}_{\text{(Ba,F)-codoped composition}}.$$

For the s and p orbitals of the Ba impurity having atomic electronic configuration of [Kr] : $4d^{10} 5s^2 5p^6 6s^2$ the sums of the corresponding up and down occupation numbers reduce from free space to the doped compositions but remain unchanged from Ba-doped to (Ba,F)-codoped composition, viz.

$$n_s(\text{up}) + n_s(\text{dn}) = \underbrace{1^\uparrow + 1^\downarrow = 2}_{\text{free-Ba atom}} > \underbrace{0.84^\uparrow + 0.84^\downarrow = 1.68}_{\text{Ba-doped composition}} = \underbrace{0.84^\uparrow + 0.84^\downarrow = 1.68}_{\text{(Ba,F)-codoped composition}}$$

and

$$n_p(\text{up}) + n_p(\text{dn}) = \underbrace{3^\uparrow + 3^\downarrow = 6}_{\text{free-Ba atom}} > \underbrace{2.06^\uparrow + 2.06^\downarrow = 4.12}_{\text{Ba-doped composition}} = \underbrace{2.06^\uparrow + 2.06^\downarrow = 4.12}_{\text{(Ba,F)-codoped composition}}.$$

The d -orbital of the Ba impurity is full and its occupation numbers almost keep fixed from free space to the doped compositions, viz.

$$n_d(\text{up}) + n_d(\text{dn}) = \underbrace{5^\uparrow + 5^\downarrow = 10}_{\text{free-Ba atom}} > \underbrace{5.03^\uparrow + 5.03^\downarrow = 10.06}_{\text{Ba-doped composition}} = \underbrace{5.03^\uparrow + 5.03^\downarrow = 10.06}_{\text{(Ba,F)-codoped composition}}.$$

For the s and p orbitals of the F impurity having atomic electronic configuration of [He] : $2s^2 2p^5$ the sum of the corresponding up and down occupation numbers reduces from the free space to the (Ba,F)-codoped composition, viz.

$$n_s(\text{up}) + n_s(\text{dn}) = \underbrace{1^\uparrow + 1^\downarrow = 2}_{\text{free-Ba atom}} > \underbrace{0.85^\uparrow + 0.85^\downarrow = 1.70}_{\text{(Ba,F)-codoped composition}}$$

and

$$n_p(\text{up}) + n_p(\text{dn}) = \underbrace{3^\uparrow + 2^\downarrow = 5}_{\text{free-Ba atom}} > \underbrace{2.14^\uparrow + 2.14^\downarrow = 4.28}_{\text{Ba-doped composition}}.$$

By taking the electronic configurations of the atoms that make up the compounds in question, i.e., Bi, Fe O, Ba, and F atoms, as quantitatively compared above, and the number of atoms for each atom in each unit cell (N), as represented in Table IV, into account, we find that the amount of extra charges in p -Bi orbitals originate from the reductions of the charges of the s -Bi, d -Fe, s -O, and p -O orbitals in the pure case compared to those of the corresponding orbitals in the free space. For both of the doped cases, as also quantitatively compared above, we have observed the same reduction trends. All these reduction trends confirm that these orbitals are hybridized to each other.

Let us turn our attention to the deeper parts of the $6s$ -Bi-DOSs of the compounds. They containing $0.54^\uparrow + 0.54^\downarrow = 1.08$, $0.46^\uparrow + 0.46^\downarrow = 0.97$, and $0.43^\uparrow + 0.43^\downarrow = 0.86$ electrons are distributed over narrow energy intervals of (-10 , 8.5 eV), (-11 , 9.5 eV), and (-11 , 9.5 eV) in the pristine, Ba-doped, and (Ba,F)-codoped compounds, as shown in Figs. 8(a), 8(b) and 8(c), respectively. The latter occupation numbers and the deep positions of the $6s$ Bi of the compounds far from the Fermi level show that the $6s$ Bi can be approximately considered as lone pair orbitals compared

to the fully occupied $6s$ orbital of the free Bi atom. More precisely, one notices that the lonely pair character of the $6s$ Bi atom decreases by doping, i.e., the occupation number of $6s$ Bi reduces from two electrons in the free space to 1.08 in the pure compound, and to 0.97 electrons in the Ba-doped composition, as well as to 0.86 in the (Ba,F)-codoped composition. This reduction trend of the $6s$ -Bi lone pairs stems from the hybridization discussed above. Now let us determine the activity degrees of the $6s$ -Bi lone pairs. To this end, let us turn our attention to the shallower parts of the $6s$ -Bi DOSs. They containing $0.14^\uparrow + 0.14^\downarrow = 0.28$, $0.10^\uparrow + 0.10^\downarrow = 0.20$, and $0.11^\uparrow + 0.11^\downarrow = 0.22$ electrons are distributed over (-7 eV, E_F), (-8 eV, E_F), and (-8 eV, E_F) broad energy intervals in the pristine, Ba-doped, and (Ba,F)-codoped compounds, respectively, as shown in Figs. 8(a), 8(b) and 8(c). The $6s$ -Ba DOS piles up in the vicinity of the Fermi level inside the shallow part of the DOS for the pure compound, see the peak close to the Fermi energy in Fig. 8(a). Such a behavior can be almost also seen for the $6s$ -Ba DOS of the (Ba,F)-codoped composition, see Fig. 8(c) where the peak has also shifted slightly back from the Fermi energy compared to the pure case shown in Fig. 8(a). But this is not the case for the Ba-doped composition where the shallow part of its $6s$ -Ba DOS is broadened with no considerable sharp peak therein, see Fig. 8(b). Therefore, the $6s$ -Bi lone pairs can be stereochemically active rather than inert in all the compounds under study. But the activity degrees of the $6s$ -Bi lone pairs stereochemically differ depending on the case. The results, in agreement with results reported in Ref. [126], show that the s -Bi lone pair loses its entirely spherical spatial electron charge distribution (ECD) and deforms from spherical to aspherical spatial ECD. Consequently, complex hybridizations of the s Bi with p O can lead to the asymmetric charge transfer in

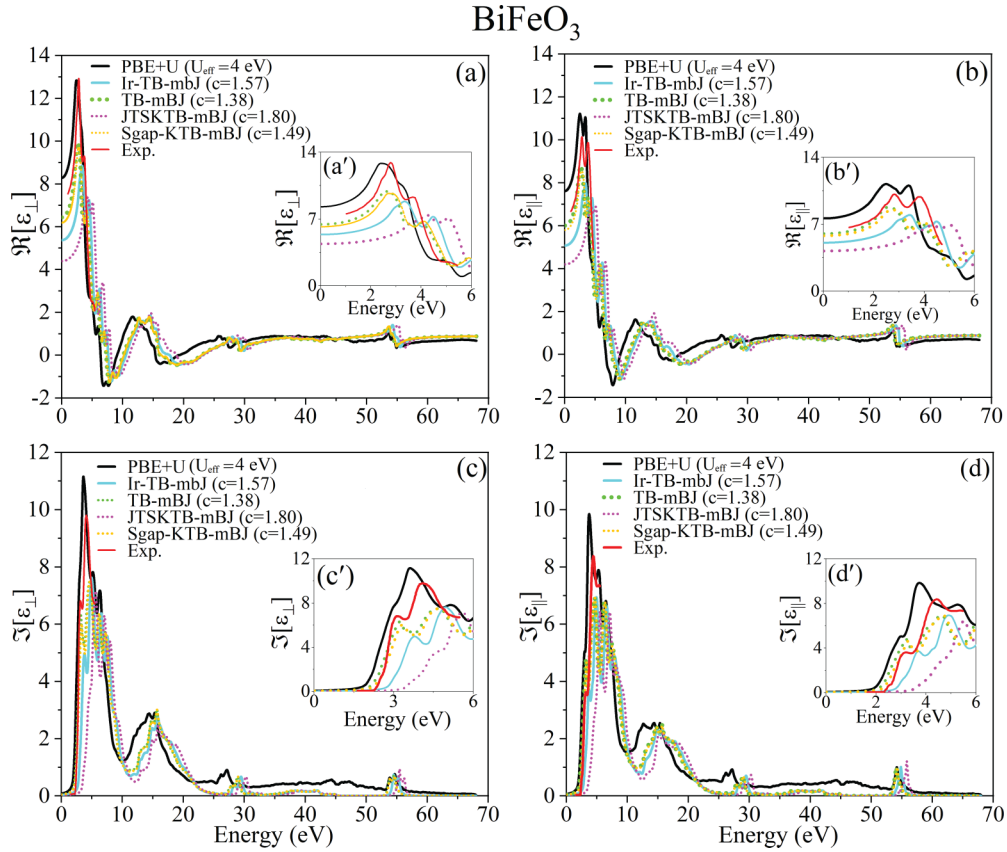


FIG. 9. (a) Perpendicular component of the real part of the dielectric tensor $\Re[\epsilon_{\perp}]$, (a') previous figure after magnification, (b) parallel component of the real part of the dielectric tensor $\Re[\epsilon_{\parallel}]$, (b') previous figure after magnification, (c) perpendicular component of the imaginary part of the dielectric tensor $\Im[\epsilon_{\perp}]$, (c') previous figure after magnification, (d) parallel component of the imaginary part of the dielectric tensor $\Im[\epsilon_{\parallel}]$, and (d') previous figure after magnification. These spectra as functions of the incident light energy, $E = \hbar\omega$, are calculated by GGA + U + SOC ($U_{\text{eff}} = 4$ eV), Ir-TB-mBJ ($c = 1.57$), TB-mBJ ($c = 1.38$), JTSKTb-mBJ ($c = 1.80$), and Sgap-KTB-mBJ ($c = 1.49$) for the pure compound. The experimental spectra extracted from Ref. [31] are represented for comparison. For the convenience of comparison, the magnified insets (a') to (d') are presented in higher resolution.

the Bi-O bonds which can provide the development of ferroelectricity in the pristine BiFeO₃. On the other hand, the s -Bi DOS of the codoped case behaves similar to the pure case, see Figs. 5(b) and 5(k). In addition, in both cases, one notices that near the Fermi surface DOS of s Bi is prominently larger than p Bi. But the behavior of s -Bi DOS in pseudocubic doped compound changes compared to the pure and codoped cases. This may indicate that the nature of the lone pair electrons of the pseudocubic composition, as can be seen from Fig. 5(f), differs from that of the hexagonal pure compound, as shown in Fig. 5(b), and that of the tetragonal codoped composition, as shown in Fig. 5(k).

Let us conclude the present section by indicating that the (Ba,F)-codoped composition, due to the stereochemically lone pair s -Bi activity discussed above, like (unlike) the pure (Ba-doped) compound has the potential to nominate in the selection of ferroelectric systems.

B. Optical properties

Leakage current is one of the most important physical factors that can reduce the residual polarization in the bismuth-based ferroelectrics [27,28]. On the other hand, it

is well known that the lower the dielectric loss at low frequency, the lower the leakage current [27]. Thus, in order to investigate the effects of Ba doping and (Ba,F) codoping on the leakage current in BiFeO₃, here, we calculate the optical loss functions of the pure and doped compounds. Optical properties including loss function can be obtained from dielectric tensors. Therefore, as the first step, let us calculate the real and imaginary parts of the dielectric tensors. In this way, we can also assess the accuracy of the results by comparing our optical properties with the available experimental data.

The perpendicular and parallel components of the real and imaginary parts of the dielectric tensor are calculated by GGA + U + SOC with $U_{\text{eff}} = 4$ eV for the pure compound. All the latter components together with the corresponding experimental spectra [31] are shown as $\Re[\epsilon_{\perp}]$, $\Re[\epsilon_{\parallel}]$, $\Im[\epsilon_{\perp}]$, and $\Im[\epsilon_{\parallel}]$ with respect to the energy of the incident radiations, $E = \hbar\omega$, in Figs. 9(a)–9(d), respectively. For more clarity, let us restrict the energy interval from [0, 70 eV] to a narrower region where measurement was performed, [0, 6 eV]. In the narrower interval, the $\Re[\epsilon_{\perp}]$, $\Re[\epsilon_{\parallel}]$, $\Im[\epsilon_{\perp}]$, and $\Im[\epsilon_{\parallel}]$ are represented in Figs. 9(a'), 9(b'), 9(c'), and 9(d'), respectively. The results show reasonable agreement with the experimental data [31], see Fig. 9. The imaginary parts of the dielectric

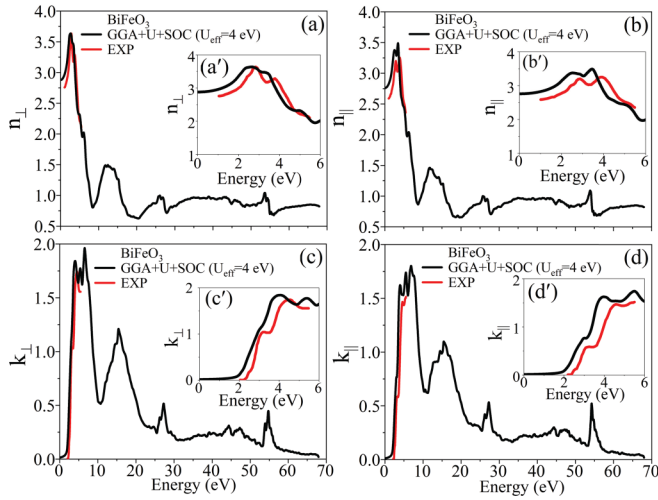


FIG. 10. (a) Perpendicular component of the index of refraction n_{\perp} , (a') previous figure after magnification, (b) parallel component of the index of refraction n_{\parallel} , (b') previous figure after magnification, (c) perpendicular component of the extinction coefficient k_{\perp} , (c') previous figure after magnification, (d) parallel component of the extinction coefficient k_{\parallel} , and (d') previous figure after magnification. All these spectra as functions of the incident light energy, $E = \hbar\omega$, are calculated by GGA + U + SOC with $U_{\text{eff}} = 4$ eV for the pure compound. The experimental spectra extracted from Ref. [31] are represented for comparison. For the convenience of comparison, the magnified insets (a') to (d') are presented in higher resolution.

tensor start to rise up at energies close to the band gap of the system. This can be seen in Figs. 9(c') and 9(d') with no a serious need to use scissor operator to shift the calculated spectrum towards higher energies, as our calculated band gaps are close to the experimental data, see Sec. V A 3. The real part of the dielectric tensor becomes negative around (6, 9 eV) and asymptotically approaches unity at high energies as expected, see Figs. 9(a) and 9(b). To ensure the accuracy of our desired results, let us also evaluate the index of refraction n and extinction coefficient k of the pure compound and compare them with the corresponding available experimental spectra. To this end, they are also obtained from the corresponding components of the dielectric tensor for the pure compound. The results, including n_{\perp} , n_{\parallel} , k_{\perp} , and k_{\parallel} together with the corresponding experimental spectra extracted from Ref. [31] are shown as functions of $E (= \hbar\omega)$ in Figs. 10(a)–10(d), respectively. For convince of comparison, the n_{\perp} , n_{\parallel} , k_{\perp} , k_{\parallel} , and k_{\perp} , k_{\parallel} are represented in the experimental energy range in Figs. 10(a'), 10(b'), 10(c'), and 10(d'), respectively. These results, as shown in Fig. 10, are also consistent with the experimental data [31].

The consistencies achieved between our optical results calculated by DFT plus RPA and the corresponding experimental spectra, as discussed above, in turn, show that the method used can provide sufficiently reliable results for the current purpose of the work. Thus, since our optical results are close to the experimental data, here, we limited the accuracy of the optical results to that is predicted by DFT + U + RPA. Despite the latter agreement, it is worth indicating that such a treatment can be further improved by including excitonic effects

or electron-hole interactions using the Bethe-Salpeter equation (BSE) [128,129]. In anticipation of further investigations, let us below discuss how optical properties can be improved by BSE over RPA. It is well known that the dielectric tensor, as the response function to the incident light, can be used to obtain optical properties of materials [130]. In principle, the dielectric function can be calculated by Eq. (1.3), as expressed in the second column of page 606 of Ref. [79], including the nonlocal bare Coulomb or Hartree interaction and the nonlocal polarizability operator. The latter operator as a sum over independent transitions can be simplified to Eq. (1.4) of Ref. [79], where in the numerator of the fraction under the summation of the latter equation exchange term is expressed. The RPA was introduced to calculate the dielectric function using the time-dependent Hartree-Fock scheme, or Lindhard approximation, for a homogeneous electron gas, where the classical electron-electron or Coulomb interaction and the ion-electron interaction cancel each other as represented in the Hartree-Fock equations [130]. The latter cancellation also occurs in the Kohn-Sham equation [131]. The term RPA indicates that the approximation expressed in Eq. (1.4) is used for the polarizability operator and thereby for the calculation of the dielectric function regardless of the classical Coulomb interaction. The imaginary and real parts of the dielectric function are represented in Eqs. (10) and (11) using a combination of the Eqs. (1.3) and (1.4) of Ref. [79] as discussed above, respectively. RPA can be either more simplified or further improved. It can be more simplified to independent particle approximation (IPA) by removing the exchange term, as well [132]. It can be further improved by keeping both the Coulomb term in Eq. (1.4) of Ref. [79] and the exchange expression in Eq. (1.4) of Ref. [79] and consequently the electron-hole interactions as included in the BSE [128]. Thus, the RPA can be considered as a simplification of the BSE in which the Coulomb term in Eq. (1.4) of Ref. [79] is neglected while the exchange expression in Eq. (1.4) of Ref. [79] is steel kept, see Ref. [132]. The holes and electrons (but not electron-hole interactions) can be described by the single-particle Kohn-Sham DFT. To understand the physics behind RPA and BSE methods, let us return to the simple IPA. If the Coulomb term is removed from Eq. (1.3) of Ref. [79] and the exchange term is also removed from Eq. (1.4) of Ref. [79], then the BSE Hamiltonian becomes diagonal, see Eq. (28) of Ref. [132]. In this simple IPA, the spectrum can be obtained by taking summation of matrix elements of the polarizability operator as the proper oscillator matrix elements over transitions between valence and conduction states [79,132]. In this case, the neutral quasiparticle excitons are neglected because in the IPA there is not any bound state for an electron and a hole to attract each other by the electrostatic Coulomb force. Therefore, the RPA (BSE) is more comprehensive than the IPA (RPA), because in RPA (BSE) exchange (and Coulomb term) term (terms) exists (exist). The exciton as an elementary excitation or electrically neutral quasiparticle is produced in insulators if they can absorb a higher energy of an incident light than its band gap so that an electron can be excited from the valence into the conduction state and whence a hole can be created in the valence band as the excited electron vacancy. In this case, the excited electron can be attracted by the created hole. Hence, the electron excited into the conduction band

can interact with the hole created in the valence band. This interaction between the excited electron and the created hole is called excitonic effects. The excitonic effects, in turn, can also introduce additional midgap states or subbands inside the band gap of the insulator or semiconductor materials, see the schematic figure represented in page 15, Fig. 4 of Ref. [132] for the DFT, GW, and BSE effects on the band structure and optical properties. These subbands can play as trapping centers in analogy to the subbands created by impurities inside the band gap of the pure system, as discussed in Sec. V A 3. Despite the latter similarity between the subbands induced by excitonic effects and impurities, the physical aspects behind them are completely different, as can be inferred from the above discussion. From the above discussion the following points may be deduced intuitively and physically. (i) The strength of the electron-hole interaction or excitonic effects can be weakened if the holes created in the valence bands are largely screened by a lot of valence electrons. This point is consistent with the statement already reported by Adamyan *et al.* on page 2 of Ref. [133]. (ii) The excitonic effects can depend on the band gap because as the band gap increases the material moves further away from the metallic state and therefore, the number of itinerant electrons decreases which, in turn, reduces the dielectric screening. This point is also in agreement with the report indicated by Gao *et al.*, see page 4, column 2 of Ref. [134], and also see the paragraph right before Eq. (5) of Ref. [129] related to the wide band gap of α -quartz shown in Fig. 1 of the latter reference. Various other points like the effects of temperature, incorporation of vacancies, defects, impurities, low dimensions, or quantum confinements, on the excitonic effects can be qualitatively deduced from the underlying physics of the quasiparticle excitons (electron-hole pairs) and most likely confirmed by already published articles. However, let us conclude the BSE discussion by turning our attention to the possible excitonic effects on the materials in question. The excitonic effects and as a result BSE can more affect insulators having wider band gaps [129] than that of the pure compound in question. The reasonable agreement between our optical and electrical results excluding excitonic effects confirm that GGA + U with optimized U can provide sufficiently satisfactory results without using BSE for the current purpose of this work. However, if further subbands created by the possible excitonic effects are experimentally demanded for some specific purposes, many-body time consuming BSE calculations would be also performed. For the doped compositions in question, the excitonic effects can even less affect the results than the pure case because their band gaps have already reduced by doping impurities compared to the pure material. This shows that the dielectric screenings in the doped compositions are stronger than that in the pure compound. Therefore, the GGA + U with the optimized U can predict better results for the doped compositions having much smaller band gaps than the pure compound.

Let us now turn our attention to the optical results calculated for the doped compositions using GGA + U + SOC with $U_{\text{eff}} = 5$ eV. In contrast to the pure compound, the doped compositions are asymmetric so that after doping the perpendicular components of their dielectric tensors, ϵ_{xx} and ϵ_{yy} , no longer remain equal to each other, *viz.* $\epsilon_{xx} = \epsilon_{\perp,xx} \neq \epsilon_{yy} = \epsilon_{\perp,yy} \neq \epsilon_{zz} = \epsilon_{\parallel}$ for doped composi-

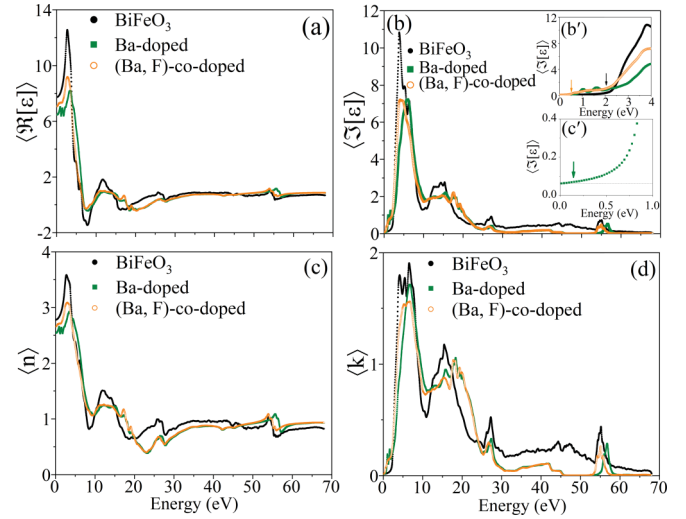


FIG. 11. (a) Average of the perpendicular and parallel components of the real part of the dielectric tensor $\langle \Re[\epsilon] \rangle$, (b) average of the perpendicular and parallel components of the imaginary part of the dielectric tensor $\langle \Im[\epsilon] \rangle$, (b') previous figure after magnification, (c') the latter figure after zooming in involving only codoped spectrum for the sake of higher resolution, (c) average of the perpendicular and parallel components of the index of refraction $\langle n \rangle$, and (d) average of the perpendicular and parallel components of the extinction coefficient $\langle k \rangle$. The spectra as functions of the incident light energy, $E = \hbar\omega$, are calculated by GGA + U + SOC with $U_{\text{eff}} = 4$ eV for the pure compound and by GGA + U + SOC with $U_{\text{eff}} = 5$ eV for the Ba-doped and (Ba,F)-codoped compositions.

tions and $\epsilon_{xx} = \epsilon_{yy} = \epsilon_{\perp} \neq \epsilon_{zz} = \epsilon_{\parallel}$ for the pure compound. Therefore, in order to make the results of the asymmetric doped compositions comparable with that of the symmetric pure compound, let us as usual take an average over the components of the dielectric tensors for the pure and doped cases. To this end, we evaluate the average as $\langle \epsilon \rangle = (\epsilon_{xx} + \epsilon_{yy} + \epsilon_{zz})/3 = \Re[\epsilon_{xx} + \epsilon_{yy} + \epsilon_{zz}]/3 + i\Im[\epsilon_{xx} + \epsilon_{yy} + \epsilon_{zz}]/3 = \langle \Re[\epsilon] \rangle + i\langle \Im[\epsilon] \rangle$ for the pure and doped compounds. By this, the effects of doping can be deduced, at least in their mean field form. Since for the pure compound the accuracy of the optical results has been already shown above in comparison with experiment, let us compare the $\langle \Re[\epsilon] \rangle$, $\langle \Im[\epsilon] \rangle$, $\langle n \rangle$, and $\langle k \rangle$ of the doped compositions with those of the pure compound in Figs. 11(a), 11(b) 11(c), and 11(d), respectively. At zero energy, $\langle \Re[\epsilon] \rangle$ is 7.74 for the pure BiFeO₃ whereas it decreases after doping to 6.48 for the Ba-doped and to 7.10 for the (Ba,F)-codoped compositions. The maximum of $\langle \Re[\epsilon] \rangle$ for the pure case, $\langle \Re[\epsilon] \rangle_{\text{max}} = 13.15$, occurs at 2.68 eV. Then, $\langle \Re[\epsilon] \rangle$ rapidly decreases to -1.50 at 7.69 eV in the pure case. In analogy to the pristine case, $\langle \Re[\epsilon] \rangle$ spectra of the doped compositions also fall suddenly after reaching to their corresponding maximum values, see Fig. 11(a). These rapid reductions can be attributed to the fact that the dipoles cannot change their orientations promptly when the electric field oscillates rapidly and/or changes suddenly. In all the pure and doped samples, $\langle \Re[\epsilon] \rangle$ spectra, after the sharp drops and reaching their minimum values, increase with oscillations as energy increases. Then, the spectra gradually become nearly constant at energies larger than

20 eV. They eventually approach unity asymptotically. We also notice that the $\langle \Im[\varepsilon] \rangle$ spectra of the doped compositions lie lower than the corresponding spectrum of the pure compound, except for a small range of energy near 10 eV and higher energies than 45 eV, see Fig. 11(b). These observations are in agreement with the previous results reported for the Ba-doped composition [21], where a decrease in $\langle \Re[\varepsilon] \rangle$ was found for 25% doping level compared to the pure sample. The optical absorption edges are estimated to occur at 2.0, 0.15, and 0.5 eV, as indicated by downward arrows in the inset Fig. 11(b') for the pure and (Ba,F)-codoped and in the inset Fig. 11(c') for the Ba-doped compositions, respectively. For more clarity, the middle energy, 0.15 eV, of the Ba-doped composition due to its small value is indicated by a downward arrow individually in Fig. 11(c'). The former (middle) [latter] energy, 2.0 (0.15) [0.5] eV, can be corresponded to the indirect energy band gap of 1.99 (0.14) [0.46] eV calculated for the pure (Ba-doped) [(Ba,F)-codoped] compound, as shown in Fig. 3(a) [Fig. 3(b)] [Fig. 3(c)]. Absorption cannot occur at energies lower than the energies of optical absorption edges. The energies of the incident photons are lower than the band gaps of the systems. Thus, the incident low energy photons cannot excite electrons from the valence into the conduction bands. The static index of refraction, $n(E = 0)$, decreases from 2.88 in the BiFeO₃ to 2.54 in Ba-doped composition and to 2.66 in the (Ba,F)-codoped composition, that is, the spectra n of the doped compositions lie below the spectrum n of the pristine compound at zero energy, see Fig. 11(c). This trend is not changed for the other energy ranges so that $n(E)$ spectra of the doped compositions also remain below the $n(E)$ spectrum of the pristine compound at nonzero energies, apart from a small energy range near 10 and 20 eV and also for energies higher than 47 eV. For the latter high energies, $E > 47$ eV, $n(E)$ does not considerably change by doping. Thus, for most of the energy range, one can conclude that the dopings cause to reduce $n(E)$, compared to the corresponding spectrum of the pure case. The behavior of the extinction coefficients $k(E)$ is relatively comparable to that of the imaginary parts of the dielectric functions $\Im[\varepsilon]$, as can be seen from Figs. 11(b) and 11(d).

The dielectric energy loss functions (ELFs) with respect to energy are shown in Fig. 12 for the pure and doped compounds. The doping effects on the intensities and displacements of ELF peaks calculated for the pure case can be clearly compared with the ELFs calculated for the doped cases, see Fig. 12. For the pure BiFeO₃, the ELF spectrum peaks having the intensities of 0.7, 1.5, 1.3, and 1.2, occur at energies 9.4, 20.5, 28.1, and 54.8 eV, respectively. The penultimate energy, 28.1 eV corresponding to the third ELF peak with the intensity of 1.3, calculated for the pure case is close to 30 eV reported by Kun Liu *et al.* [32]. For the Ba-doped ((Ba,F)-codoped) composition, the ELF peaks with the intensity values of 0.48 (0.51), 3.45 (3.05), 2.23 (2.02), and 0.81 (0.62) occur at energies 10.20 (9.54), 23.88 (23.91), 27.66 (27.44), and 56.91 (55.09) eV, respectively. The importance of the above calculated intensities and their corresponding energies as well as their physical interpretations can be elucidated by considering the physical concepts of the ELF spectra shown in Fig. 12. By this figure, we represent the energy losses of fast electrons traversing the pure compound and

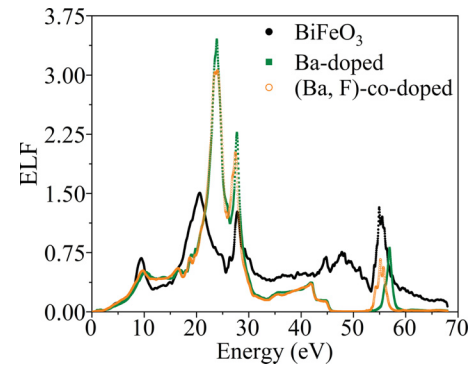


FIG. 12. Energy loss function, ELF, versus the energy of the incident radiation for the pure and doped compounds. All the ELF spectra as functions of the incident light energy, $E = \hbar\omega$, are calculated by GGA + U + SOC with $U_{\text{eff}} = 4$ eV for the pure compound and by GGA + U + SOC with $U_{\text{eff}} = 5$ eV for the Ba-doped and (Ba,F)-codoped compositions.

doped compositions. Therefore, the ELF spectra show how the energies are transferred from the transmitted electron to the materials in question, see Ref. [135]. As such, the ELF spectra reflect the scattering processes during the passage of the fast electrons through the materials [135]. Among these ELF peaks two kinds of peak can be observed: tall or prominent and short or weak peaks, corresponding to high and low ELF intensities reported above for the materials under study, respectively. The maximum intensity of an ELF spectrum occurs at an energy which is called the plasmon resonance energy and thence the corresponding peak is also called the plasmon peak [136]. As such, a plasmon peak is a prominent peak. But not every peak is necessarily a plasmon peak. Therefore, from our ELF results shown in Fig. 12 and the definitions of plasmon peak and energy, it can be seen that the plasmon peak of the pure compound is shifted towards higher energies from 20.5 to 23.88 eV for the Ba-doped composition and to 23.91 eV for the (Ba,F)-codoped composition. The latter plasmon energy of the (Ba,F)-codoped composition is close but a little bit larger than that of the Ba-doped composition, viz. 23.91 eV \gtrsim 23.88 eV. According to the definition of the ELF, as expressed in Eq. (9), these plasmon peaks of the pure compound and doped compositions occur where their corresponding real parts of the dielectric functions, as shown in Figs. 9(a) and 11(a), cross zero, $\Re[\varepsilon(E)] \approx 0$, with a positive slope, $d\{\Re[\varepsilon(E)]\}/dE > 0$, and the imaginary parts of the dielectric functions, as shown in Figs. 9(b) and 11(b), nearly vanish, $\Im[\varepsilon(E)] \ll 1$, with a negative slope, $d\{\Im[\varepsilon(E)]\}/dE < 0$. $\Im[\varepsilon(E)]$, as expressed in Eq. (3), yields the probability of the single-particle excitations according to the Fermi's golden rule [136,137]. In Eq. (3), the transition energies of the single-particle excitations manifest themselves as the prominent peaks of the $\Im[\varepsilon(E)]$ spectrum.

The oscillation strengths of the excitation peaks depend on the optical or joint density of states (JDOS) [129], i.e., $\Delta(E_{\mathbf{c}\mathbf{k}} - E_{\mathbf{v}\mathbf{k}} - \hbar\omega)$, and the diagonal matrix elements of the momentum operator, i.e., $\langle \mathbf{c}\mathbf{k}|p_{\alpha}|\mathbf{v}\mathbf{k}\rangle \langle \mathbf{v}\mathbf{k}|p_{\alpha}|\mathbf{c}\mathbf{k}\rangle = \langle \mathbf{c}\mathbf{k}|p_{\alpha}|\mathbf{v}\mathbf{k}\rangle \langle \mathbf{c}\mathbf{k}|p_{\alpha}|\mathbf{v}\mathbf{k}\rangle^* = |\langle \mathbf{c}\mathbf{k}|p_{\alpha}|\mathbf{v}\mathbf{k}\rangle|^2$ where in Eq. (3) $\alpha = \alpha'$ for the diagonal elements of the matrix representation of the momentum operator. It is worth mentioning that the

TABLE V. Energies of the prominent peaks of parallel component of imaginary part of dielectric tensor $\Im[\epsilon_{\parallel}]$, and their corresponding permissible absorption (emission) transitions, as well as changes in the orbital angular momentum quantum number Δl , spin angular momentum quantum number $\Delta\sigma$, and wave vector $\Delta\mathbf{k}$, for BiFeO₃. The permissible transitions are obtained according to the selection rules ($\Delta l = \pm 1, 0$ with no $0 \rightleftharpoons 0$ transition, $\Delta\sigma = 0$, and only direct transitions in RPA $\Delta\mathbf{k} = 0$). Indirect transitions in RPA, i.e., $\Delta\mathbf{k} \neq 0$, are not allowed because of the momentum conservation law resulted from the Fermi's golden rule in the lack of linear momentums of phonons Refs. [117–119]. In the first column, “Color” refers to the colors of the downward triangle symbols pointing to the prominent peaks of $\Im[\epsilon_{\parallel}]$ spectrum as shown in Fig. 13.

Color	Energy (eV)	Transitions	Δl	$\Delta\sigma$	$\Delta\mathbf{k}$
▼ Gray	3.0	$O 2p \rightleftharpoons Fe 3d, O 2p \& Fe 3d \rightleftharpoons Fe 3d, O 2p$	$\pm 1, 0$	0	0
▼ Blue	3.7	$O 2p \rightleftharpoons Fe 3d, O 2p, Bi 6p \& Fe 3d \rightleftharpoons Fe 3d, O 2p$	$\pm 1, 0$	0	0
▼ Green	5.3	$O 2p \rightleftharpoons Fe 3d, O 2p, Bi 6p \& Fe 3d \rightleftharpoons Fe 3d, O 2p$	$\pm 1, 0$	0	0
▼ Black	6.5	$O 2p \rightleftharpoons Fe 3d, O 2p, Bi 6p \& Fe 3d \rightleftharpoons Fe 3d, O 2p$	$\pm 1, 0$	0	0
▼ Olive	10.6	$Fe 3d \rightleftharpoons Bi 6p, O 2p \& O 2p \rightleftharpoons O 2p, Fe 4s, \& Bi 6p \rightleftharpoons O 2p, Fe 4s$	$\pm 1, 0$	0	0
▼ Red	12.6	$Bi 6s \rightleftharpoons Bi 6p, O 2p \& Fe 3d \rightleftharpoons Bi 6p, O 2p \& O 2p \rightleftharpoons O 2p,$ $Fe 4s \& Bi 6p \rightleftharpoons O 2p, Fe 4s$	$\pm 1, 0$	0	0
▼ Orange	14.4	$Bi 6s \rightleftharpoons Bi 6p, O 2p \& Fe 3d \rightleftharpoons Bi 6p, O 2p \& O 2p \rightleftharpoons O 2p,$ $Fe 4s \& Bi 6p \rightleftharpoons Bi 6p, O 2p, Fe 4s$	$\pm 1, 0$	0	0
▼ Pink	15.3	$Bi 6s \rightleftharpoons Bi 6p, O 2p \& Fe 3d \rightleftharpoons Bi 6p, O 2p \& O 2p \rightleftharpoons O 2p,$ $Fe 4s, \& Bi 6p \rightleftharpoons Bi 6p, O 2p, Fe 4s$	$\pm 1, 0$	0	0
▼ Navy	19.1	$Bi 6s \rightleftharpoons O 2p, Bi 6p \& Fe 3d \rightleftharpoons Bi 6p, O 2p \& O 2p \rightleftharpoons O 2p,$ $Fe 4s, \& Bi 6p \rightleftharpoons O 2p, Fe 4s$	$\pm 1, 0$	0	0
▼ Cyan	26.2	$O 2s \rightleftharpoons O 2p, Bi 6p$	± 1	0	0
▼ Violet	27.3	$O 2s \rightleftharpoons O 2p, Bi 6p$	± 1	0	0

optical DOS spectrum, i.e., JDOS, not shown here, can be obtained from Eq. (3) by setting all the matrix elements of the momentum operator to unity, e.g. see Ref. [129], Chapter 4 of Ref. [80], Fig. 5 of Ref. [83] and its related discussion. ELF, as expressed in Eq. (9), yields the probability of the collective-particles excitations or coherent oscillations of the valence charges, in addition to the above probability of the single-particle excitations yielded from $\Im[\epsilon(E)]$, as expressed in Eq. (3), see Ref. [137]. Therefore, in Eq. (9), the transition energies of the collective-particles excitations manifest themselves as the prominent peaks of the ELF spectrum. This implies that the difference between $\Im[\epsilon(E)]$ and ELF is due to being single and collective transitions of the particles in these two spectra, respectively. This means that each peak of $\Im[\epsilon(E)]$ originates from a single permissible transition between a valence DOS and a conduction DOS whereas each peak of ELF can originate from collective permissible transitions between several valence DOSs and several conduction DOSs. Therefore, the prominent energies of the plasmon peaks obtained from the ELF spectra determine the energies and whence frequencies of the incident electromagnetic waves at which the collective-particles excitations, besides the single-particle excitations, can also occur, due to the interactions of the electromagnetic waves with the valence electrons of the materials [137]. In order to find the sources of these prominent peaks, in addition to the ELF, we consider all the partial valence and conduction DOSs, band structures, and imaginary part of the dielectric tensor all together simultaneously, and then systematically analyze them. For this rigorous analysis, $\Im[\epsilon_{\parallel}]$ is considered, because the peaks of $\Im[\epsilon_{\parallel}]$ are a little bit sharper than and more importantly very close to those of $\Im[\epsilon_{\perp}]$. We also checked $\Im[\epsilon_{\perp}]$ but did not find more new transitions. In these analyses, we consider the following selection rules for both the angular momentum and spin, as well. To find the permissible interband transitions, we note

that any single or collective transition must satisfy the selection rules derived from Wigner-Eckart theorem [138] due to nonzero Clebsch-Gordan coefficients [138] for a spherical tensor of rank 1 [138] related to the linear momentum operator existed in both the Eqs. (3) and (9), viz. $\Delta l = 0, \pm 1$ regardless of the forbidden ($l = 0$) \longleftrightarrow ($l = 0$) transition, where l is the angular momentum quantum number, see also Ref. [83]. The latter selection rule, $\Delta l = 0, \pm 1$, is considered and accordingly satisfied by the states, as can be seen from the permitted transitions tabulated in Table V. We also consider the spin selection rule that indirect/different spin transitions between spin up valence DOS and spin down conduction DOS or spin down valence DOS and spin up conduction DOS are forbidden, see Ref. [137]. The spin selection rule originates from the lack of required momentum transfer/spin flip under photon absorption or emission [137]. Therefore, only transitions between valence and conduction states with the same spin are allowed, viz. $\Delta\sigma = 0$, where spin number σ is 1 for spin up and -1 for spin down. This selection rule, $\Delta\sigma = 0$, is considered, see Table V. In this analysis, we consider only direct transitions ($\Delta\mathbf{k} = 0$), since indirect or nonvertical transitions, i.e., $\Delta\mathbf{k} \neq 0$, are forbidden in the framework of RPA [117]. According to RPA, direct or vertical transitions are allowed only, see Eqs. (1) and (2) of Ref. [117]. However, if, in addition to photons, phonons are also involved, indirect or nonvertical transitions can take place, as well, see equation (3) of Ref. [117]. In the presence of phonons, momentums of electrons can be conserved in the indirect transitions, see equations (1) to (3) of Ref. [118], whereas, in the absence of phonons, momentums of electrons can be conserved in the direct transitions only, see also Ref. [119]. Taking these selection rules into account, our analyses are summarized in Fig. 13 and Table V. The summarized analysis shows that these prominent peaks mainly originate from the excitation states of the bound electrons of $O 2s, O 2p, Bi$

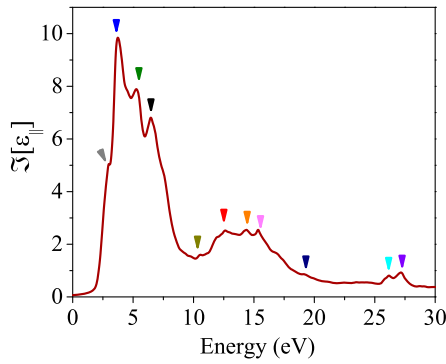


FIG. 13. Prominent peaks of the parallel component of the imaginary part of the dielectric tensor $\Im[\epsilon_{\parallel}]$ for BiFeO₃. The energies of the prominent peaks and their corresponding permitted transitions, as extracted from the associated partial DOSs and band structures, are tabulated in Table V, as indicated herein by the colored downward triangle symbols pointing to the peaks of $\Im[\epsilon_{\parallel}]$ spectrum.

6s, Bi 6p, Fe 3d, Fe 4s orbitals, see Fig. 13 and Table V. Vo Khuong Dien *et al.* also similarly studied transitions in LiFeO₂ attributing them to the excitation of Li 2s, O 2p, and Fe (4s and 3d) orbitals, see Table 2 of Ref. [139] and related discussion. These bound electrons can enhance photocurrent generation which in turn can improve the photovoltaic effects. Let us now turn our attention to the short or weak peaks of the ELF in Fig. 12, as indicated above. The latter weak plasmons modes originate from two sources. The first source is the so called Landau damping upon which conversely the collective excited states decay back to the single particle excited states [137]. Therefore, the weak plasmon peaks reported in this work determine energies/frequencies of the incident electromagnetic waves at which the Landau damping occur and thereby the constructed collective excited states are absorbed to their unexcited states. The second source of the weak modes originates from the energy regions where there are not zero-crossing points for $\Re[\epsilon(\omega)]$, though $\Im[\epsilon(\omega)]$ remains finite [137] so that the aforementioned conditions for constitution of the prominent modes are violated. The change in width and shape of plasmons may also originate from the different symmetries of the pristine case, *R3c*, and the doped cases, *P4mm*. We note that the Ba doping has remarkable impact on both the number and width of plasmons resulting in the well biplasmons generation in energy window 10-30 eV that maybe enhanced photovoltaic property, see Ref. [140]. After Ba doping, F doping reduces the energy of the peak and shifts most of the peaks in the Ba-doped case backwards to lower energy occurred in the codoped case. The latter shift results in a smaller leakage compared to the Ba-doped composition. Therefore, the data extracted from our ELF may be useful to predict the relative mobility of the charge carriers [141] and existing less multi-peaks in the ELF spectra of the codoped composition compared to that of the pure case may illustrate lower mobility of the carriers in various ranges of energy. It is worth to mention that the ELF spectra of the doped cases vanish in (46, 53 eV) and (57, 68 eV) which is not the case for the pristine compound in which its ELF spectrum nowhere vanishes, see Fig. 12. On the other hand, the ELF spectra of the doped compositions exhibit two high peaks. Thus, at some

energies, the electric loss functions of the doped compounds become zero, whereas at some other energies become very large. The pure case does not show the latter characteristic, that is, switching between two extreme limits, i.e., zero and high ELFs. One would also notice that the ELF peaks of the doped compositions are shorter than those of the pure compound almost at all the energies, apart from two long peaks occurred at energies around 24.00 and 27.50 eV, see Fig. 12. The ELF spectra of both the doped compositions almost match everywhere except in the energy range of (52.50, 69.00 eV) where a shift of 1.82 eV is observed between their peaks. In one side our results show that the ELF spectra of the Ba-doped and (Ba,F)-codoped compositions locate under the ELF spectrum of the pure compound in most of the energy intervals, except for (21.65, 28.56 eV) and (12, 17 eV). On the other hand, it is known that the lower the ELF, the lower the leakage current [27].

Before concluding this section, time seems apt to complete the half-baked discussion on the accuracy of the calculations, as started from Sec. V A 2 and continued in Sec. V A 3. To this end, let us turn our attention to the optical gaps, as tabulated in Table III, and the real and imaginary parts of the dielectric functions, as shown in Fig. 9. We defined the electronic band gap E_g^e in Sec. V A 3 and postponed the definition and discussion of the optical gap to this section wherein the exciton effect and neutral quasiparticle exciton as elementary but necessary concepts to physically interpret the results have been already discussed. Then, to begin the discussion, let us, first, define the optical gap to distinguish it from the electronic band gap. The optical gap E_g^{opt} is defined to be the lowest optical transition after photon absorption [120,142]. In other words, E_g^{opt} is the threshold energy for a photon to be absorbed, creating an exciton, i.e., an electron-hole pair that is bound together. In this sense, the optical gap without (w/o) electron-hole interaction $E_g^{\text{opt, w/o}}$ can be defined as the energy for creating an electron-hole pair that is not bound together [137]. Thus, the electron-hole binding energy (E_B) can be defined to be the difference energy between the optical gaps with (w) and without (w/o) electron-hole interaction, viz. $E_B = E_g^{\text{opt, w/o}} - E_g^{\text{opt, w}}$ [137]. In general, $E_g^{\text{opt, w/o}} > E_g^{\text{opt, w}}$, since after creating an exciton additional energy is needed to dissociate electron and hole from each other, and as a result $E_B > 0$ [120,129,137,142]. If such an additional binding energy is not provided, then the created pair of electron-hole remains coupled to each other. However, in contrast to the organic semiconductors and single-walled carbon nanotube, in the conventional inorganic semiconductor crystals, the E_B is usually small and thereby can be approximately ignored [120], i.e., $E_B \approx 0$. Furthermore, excitonic effects are more important in wide electronic band gap semiconductors such as α -quartz [129] and γ -Al₂O₃ [44,83]. Therefore, in this work, we drop the superscripts w and w/o. Hence, we simply indicate the optical gap by E_g^{opt} , instead of $E_g^{\text{opt, w}}$ and $E_g^{\text{opt, w/o}}$, viz. $E_B \approx 0 \implies E_g^{\text{opt, w}} \approx E_g^{\text{opt, w/o}} \equiv E_g^{\text{opt}}$. Taking the definitions of electronic band gap and optical gap into consideration, E_g^e should be distinguished from E_g^{opt} , otherwise it can manifest itself as a discrepancy between experimental and theoretical energy gaps. In Sec. V A 3, we discussed the sources of discrepancy between a measured experimental energy gap and

the other measured experimental energy gaps as well as the sources between a calculated theoretical energy gap and the other calculated theoretical energy gaps. Here, we discuss that the corollary of not distinguishing E_g^e and E_g^{opt} can be one of the main sources of discrepancy between a calculated theoretical energy gap and measured experimental energy gaps. This point becomes more crucial for the pure case under study, because most of the experimental energy gaps are optical gaps, while most of the theoretical energy gaps are electronic band gaps, see Table III. It is well known that an electronic band gap theoretically calculated by DFT+LDA/GGA is much less than its corresponding electronic band gap experimentally measured. Therefore, more elaborations, e.g., considering different theoretical methods, exchange-correlation functionals, exchange potentials, are usually performed to increase the theoretical E_g^e to approach it towards the experimental value. An optical gap is measured to be larger than its corresponding experimental electronic band gap, since E_g^e (E_g^{opt}) is almost close to the first uprising (peak) energy point of the imaginary part of the dielectric spectrum and the first peak is formed after the hillside of the spectrum, see Fig. 9 and Table III. Therefore, if the available experimental energy gap is the optical gap and E_g^e is not distinguished from E_g^{opt} , then, in order to reproduce the experimental E_g^{opt} , one may wrongly try to increase the theoretical E_g^e by applying large repulsive potentials more than necessary. In this case, the excessive increase of the electronic band gap can destruct the band structure. In this case, we have not only made the electronic band gap larger than the actual electronic band gap but also made the other physical properties resulting from the destructed band structure more incompatible with the experiment. This can be clearly seen in Fig. 9, where dielectric spectra calculated by different methods are compared with the corresponding experimental spectra. The comparison shows that over-increasing the energy gap too much by Ir-TB-mBJ ($c = 1.57$) and JTSKTB-mBJ ($c = 1.80$) has not only improved the results, it has caused more inconsistencies compared to the experimental spectra, e.g., see the insets Figs. 9(c') and 9(d'). The result shows that the spectra calculated by PBE-GGA + U with $U_{\text{eff}} = 4$ eV and TB-mBJ with $c = 1.38$ predicting smaller band gaps are closer to the experimental spectra than the other spectra calculated by Ir-TB-mBJ ($c = 1.57$), JTSKTB-mBJ ($c = 1.80$), and Sgap-KTB-mBJ ($c = 1.49$), see the insets Figs. 9(a) to 9(d) and their insets (a') and (d') and Table III. Let us recall that the $U_{\text{eff}} = 4$ eV and TB-mBJ with $c = 1.38$ are those two functionals that could reproduce magnetic moment in better agreement with the experimental magnetic moment than the other functionals used in Sec. VA 2, see Table III. In band structures section, Sec. VA 3, we did not decide, about the appropriate functionals, because most of the experimental energy gaps were optical gaps. But now we are in a position to try to complete this task, as well. To this end, let us calculate the optical gap of the pure system. For this, first, using Eq. (7), we convert our calculated perpendicular component of the extinction coefficient, k_{\perp} , to the absorption coefficient, α . For this purpose, k_{\perp} is considered for the case under study, because it leads to smaller optical gap than k_{\parallel} and therefore, k_{\perp} can determine the first excitation related to the actual optical gap. Second, following Tauc method [45], we

use Eq. 8 to plot $(\alpha E)^2$ and $(\alpha E)^{1/2}$ versus energy for extracting direct and indirect optical gaps, as shown in Figs. 14(a) and 14(b), respectively. Third, to find the reliable slopes of the tangent lines to the curves, we, following the method proposed by Makuła, Pacia, and Macyk [46], determine the optical gaps, as shown in Fig. 14. In this figure, in addition to the spectra calculated by PBE-GGA + U with $U_{\text{eff}} = 4$ eV and the original TB-mBJ with $c = 1.38$, experimental spectra measured by S. G. Choi *et al.* [39] are also included for comparison, see the inset of Fig. (3) of the latter reference. Similarly, we calculate the direct and indirect optical gaps using several other functionals but the results are more than that can be presented in Fig. 14 and therefore, the rest of the other results are presented in the Table III only. It is worth mentioning that indirect optical transitions include a photon and at least one phonon in order to conserve linear momentum and thereby indirect optical gap is less than direct optical gap [117]. Our calculated indirect optical gaps are also less than direct optical gap, Fig. 14 and Table III. It is also noteworthy that indirect transitions in RPA method is forbidden momentum due to conservation law resulted from the Fermi's golden rule in the lack of linear momentums of phonons and only direct transitions can take place. In nature, however, the probability of indirect transitions may be nonzero, and it can be predicted theoretically by Tauc method [45]. As in RPA indirect transitions are forbidden, our indirect optical gaps extracted from our absorption spectra serve only as a prediction, though they are comparable with the experimental data extracted from correct experimental absorption spectra. It is worth indicating that in contrast to electronic band gap, optical gap according to its definitions can be either direct or indirect depending on the transition occurred. The occurred transition itself, in turn, depends on the possibility of phonon absorption or emission. If when an electron transits from the conduction band to the valence band or vice versa, in addition to photon emission or absorption, phonon absorption or emission also occurs so that both momentum and energy are conserved, then the transition will be indirect. However, if during the latter transition phonon absorption or emission does not occur, then the transition will be direct. Therefore, the optical gap can be a double-valued quantity, because its definition depends on what happens during the experiment, i.e., whether a phonon absorption or emission occurs in practice or not. Hence, this can be considered as another source of discrepancy between energy gaps, if the single-valued electronic band gap is not well distinguished from the double-valued optical gap. Let us return to the main discussion and try to finish it, though there are many physical points that can be mentioned. The comparison shows that both of the methods, PBE-GGA + U with $U_{\text{eff}} = 4$ eV and the original TB-mBJ with $c = 1.38$, can successfully reproduce the experimental direct and indirect optical gaps. Overall, taking magnetic moment, as tabulated in Table III, dielectric spectra, as shown in Fig. 9, optical gaps, as shown in Fig. 14 and tabulated in Table III, and the results of the doped compositions into account altogether we choose we choose the PBE-GGA + U with $U_{\text{eff}} = 4$ eV for the study of the pure case and with PBE-GGA + U with $U_{\text{eff}} = 5$ eV for the study of the doped case to the extend

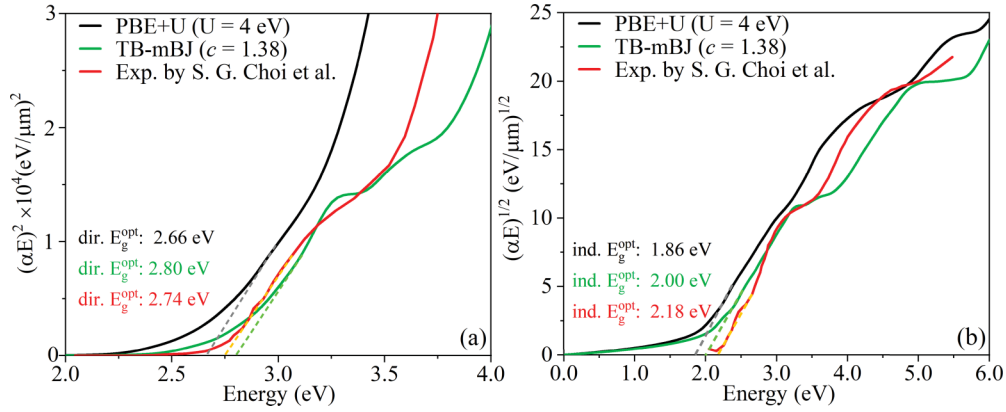


FIG. 14. Extractions of (a) direct optical gap (dir. E_g^{opt}), and (b) indirect optical gap (ind. E_g^{opt}) from our calculated perpendicular extinction spectra, as discussed in Sec. VB, using Eqs. (7) and (8), as expressed and discussed in Sec. IV A, using GGA + U + SOC with $U_{\text{eff}} = 4$ eV and TB-mBJ with its self-consistently converged $c = 1.38$ for the pure compound. The experimental curve is also obtained by applying Eq. (7) on the k_a spectrum, as shown in Fig. 3(b) of Ref. [31]. Then, the experimental dir. E_g^{opt} , as shown in the current figure (a), and ind. E_g^{opt} , as shown in the current figure (b), are extracted from the latter obtained experimental curve using Tauc method [45] method, i.e., employing Eq. (8). To increase the accuracy of the slopes of the tangent lines to curves, the method proposed in Ref. [46] is used, see Table 1 and Figs. 1 to 4 of the latter reference. This dir. E_g^{opt} is also consistent with the experimental direct optical gap extracted from the inset of Fig. 3 of Ref. [39].

presented by the results and their related discussions in this work.

Therefore, putting altogether, we have found that the Ba doping and (Ba,F) codoping can reduce the current leakage. This finding taking the symmetries and polar distortions of the doped compositions into account motivated us to investigate the effects of codoping on the spontaneous electric polarization which is the subject of the subsequent section, Sec. VC. Before this, let us ensure that it is consistent with experiment, as well. To this end, we noticed that this fact was also experimentally reported by Sinha *et al.* [27] that lower loss peak at an energy resulted in lower leakage current for the chromium-doped multiferroic bismuth ferrite, Cr doped BFO NPs, see Figs. 4 and 5 of Ref. [27]. Consequently, in Sec. VC, as the final contribution of this article, let us verify to make sure that whether the (Ba,F) codoping can also improve the intrinsic ferroelectricity of the multiferroic BiFeO_3 .

C. Spontaneous electric polarization

In this section, let us take the final step to complete the steps taken so far to introduce the (Ba,F)-codoped composition as a suitable alternative to the problematic pure compound. However, let us first calculate the spontaneous electric polarization for the pure case in Sec. VC1. By this, we can show the accuracy of the polarization calculation by comparing the calculated polarization of the pure compounds with the already available corresponding experimental and theoretical data. Then, we ultimately present our calculated spontaneous electric polarization for the codoped composition in Sec. VC2.

1. Pristine compound

Let us first consider the most stable phase of the pure BiFeO_3 pristine compound and calculate its electric polarization by density functional plus Berry phase theories. The calculations are performed using PBE-GGA + U with the

optimized $U_{\text{eff}} = 4$ eV for the G-AFM configuration of the rhombohedral ($R3c$) symmetry. To this end, we first optimized the lattice parameters by the latter functional considering its optimized parameter. Then, we calculate the SEPs using both the latter optimized lattice and Hubbard parameters. Since the polarization can depend on the c/a ratio, we recalculate the SEPs using the experimental lattice parameters reported in Ref. [143], as well. Furthermore, the polarization can also depend on the functional, Hubbard parameter, and the DFT solver method used. Zhang *et al.* [48] calculated the SEPs of the pure compound by PBE-GGA + U and LDA + U with $U_{\text{eff}} = 2$ eV using pseudopotential method. Thus, to make the comparison with the results reported in Ref. [48] more meaningful, we recalculate the SEPs using LDA + U with $U_{\text{eff}} = 2$ eV. Moreover, we recalculate the SEPs using LDA + U with our optimized $U_{\text{eff}} = 4$ eV. All the above results together (after performing unwrapping procedure, not shown here for this comparative phase) with the available theoretical results [48,49] and experimental data [51] are tabulated in Table VI. The comparison shows reasonable agreement with the theoretical [48,49] and experimental [51] data. Keeping fixed the c/a ratio, the results show that the polarization increases as U_{eff} decreases. It is well known that the larger the U_{eff} , the larger the localization degree. Hence, this implies that if c/a can remain unchanged, a larger localization degree can result in a smaller polarization. The results also show that for a fixed localization degree, SEP increases by growing up the c/a ratio.

In addition to the most stable $R3c$ symmetry, let us also consider the tetragonal ($P4mm$) structure for the pure compound, because the symmetry of the (Ba-F)-codoped composition as the main material of this work is also $P4mm$. In this case, the effects of the codoped can be more shown up. For the $P4mm$ symmetry in the AFM phase of the pure compound, we optimized the U_{eff} parameter once more, and found it to be 6 eV. Then, using PBE-GGA + U with $U_{\text{eff}} = 6$ eV, we used the optimized lattice parameters of the codoped

TABLE VI. Spontaneous electric polarization (ΔP) in $\mu\text{C}/\text{cm}^2$, lattice parameter (a) in \AA , hexagonality or tetragonality ratio c/a , code (Code), exchange-correlation functional (XC), Hubbard parameter (U) in eV, magnetic orderings (MO), and computational method (Scheme) for pure BiFeO_3 in both the $R3c$ and $P4mm$ symmetries and (Ba,F)-codoped composition in $P4mm$ symmetry. Available experimental and other theoretical results are included for comparison, as well. The present results are denoted by *. To avoid repetition, every blank cell of each block of the table, excluding irrelevant cells assigned to the experimental data, represents the repetition of its own upper cell in the table.

Crystal	Scheme	Symmetry	XC	U_{eff} (eV)	MO	Code	a	c/a	$\Delta P(\mu\text{C}/\text{cm}^2)$	Ref.	
BiFeO_3	Berry phase	$R3c$	PBE + U	4.0	G-AFM	WIEN2K	5.625	2.510	102.35 ^a	*	
			LDA + U	4.0			5.502	2.506	101.99 ^a	*	
			PBE + U	4.0			5.579	2.486	101.90 ^b	*	
				2.0						103.52 ^b	*
			LDA + U			VASP	5.497	2.453	94.80	[48]	
		PBE + U			2.0		5.623	2.500	100.30	[48]	
	Born effective charges				4.0			5.609	2.455	90.90	[49]
		Experiment								100.00	[51]
		Berry phase	$P4mm$	PBE + U	6.0	AFM	WIEN2K	3.996	1.050 ^c	125.66	*
					4.0	G-AFM		3.700	1.260	144.10	[47]
	Experiment				AFM				130.00 \pm 5.00	[50]	
(Ba-F)-codoped	Berry phase	$P4mm$	PBE + U	5.0	G-AFM	WIEN2K	3.996	1.050	80.17	*	

^aUsing our optimized lattice parameters calculated by the functionals reported in this table.

^bUsing experimental lattice parameters reported in Ref. [143].

^cThis ratio is obtained for the initial unit cell without spin polarization.

compound. Eventually, using the optimized U_{eff} and lattice parameters, we calculate the SEP. The SEP is then unwrapped, as discussed in Appendix. The unwrapped results together with the available experimental [50] and theoretical [47] results calculated for the G-AFM using PBE-GGA + U with $U_{\text{eff}} = 4$ eV are tabulated in Table VI for comparison. The comparison shows agreement with the experimental data. It also shows a reasonable agreement with the theoretical result taking the difference between the lattice parameters and thereby the c/a ratios as well as the difference between the considered magnetic phases, i.e., AFM and G-AFM, and as a result the difference between the optimized U_{eff} values, i.e., 4 and 6 eV.

Let us conclude this section as: since our optimization performed and procedure used to calculate the SEPs of the pure case in both $R3c$ and $P4mm$ symmetries are able to successfully reproduce the corresponding experimental data, it can be reliable almost within the same accuracy for predicting the SEP of the (Ba,F)-codoped composition, as well.

2. (Ba,F)-codoped composition

The ultimate task is to show that the spontaneous electric polarization can considerably exist in the codoped composition. To this end, the electric polarization of tetragonal (Ba,F)-codoped structure is calculated by the DFT-based full-potential APW + lo method accompanied by the Berry phase approach. The calculations are performed using GGA + U with the optimized $U_{\text{eff}} = 5$ eV for the $P4mm$ symmetry of the (Ba,F)-codoped composition. After performing the regular polarization calculations, we also consider the uncertainty problem lying in the heart of the modern theory of polarization. The Berry phases are usually wrapped into $[-\pi, \pi]$, e.g., see Ref. [35]. In fact, the Berry phase is well-defined modulo 2π . Consequently, the polarization is only well-defined modulo $e\mathbf{R}/\Omega$, where \mathbf{R} , e , and Ω are defined in Sec. IV B, see

also Ref. [144]. This is a resulting feature of the Berry phase theory of polarization where the polarization is defined only modulo a quantum of polarization indicating that the polarization may be considered as a multivalued quantity [144]. In Appendix, we find the best branch to resolve the uncertainty in the modulo $e\mathbf{R}/\Omega$ of the polarization. To this end, we compute the polarization at several intermediate points along the transition path following the procedure proposed by Raffaele Resta and David Vanderbilt in Ref. [144]. By this way, we unwrap the results to remove the uncertainty and uniquely determine the polarization. The final spontaneous electric polarization is given in Table VI. The result confirms that in the convenient $P4mm$ phase of the (Ba,F)-codoped composition, a considerable spontaneous polarization exists, though it is smaller than that of the pure case in spite of having the same c/a ratio. Therefore, the (Ba,F)-codoped composition can be considered as a multiferroic material due to the coexistence of SEP and G-AFM orderings, and as a less problematic applied material due to its more favorable symmetry and less leakage, compared to the pure case with its higher SEP but less desired symmetry and larger leakage. The origin of polarization in the codoped material mainly stems from the displacive atoms during the adiabatic transition from the nonpolar ($\lambda = 0$) to the polar ($\lambda = 1$) phase. In the codoped composition, the atomic displacements from $\lambda = 0$ to $\lambda = 1$ are found to be nonzero in the x and z but zero in the y direction. Thus, the polarization vector of the codoped composition has two x and z components, as discussed in Appendix. According to our results, the transverse x component of the SEP vector of the codoped composition mostly originates from the displacements of the Bi atoms whereas its longitudinal z component originates from the displacements of the Bi, Fe, and O atoms. In the pure compound, however, the polarization vector is oriented along the z direction only, and it has no net components in the other x and y directions. Therefore, the smaller polarization of the codoped composition mainly originates from the different

atomic displacements both in terms of magnitudes and directions. This in turn may originate from the doping of Ba and F cations with different atomic sizes and interactions compared to their corresponding hosts Bi and O. The SEP trend from pure to codoped material is consistent with the data tabulated in Table I of Ref. [145] reported by Tingting Qi *et al.* for the PbTiO_3 , following the same transition as (and having a close tetragonality of $c/a = \underbrace{1.065}_{\text{PbTiO}_3} \approx \underbrace{1.05}_{\text{BiFeO}_3}$ to) the BiFeO_3 , an its doped ferroelectric perovskite solid solutions.

Let us conclude the work by expressing that the spontaneous electric polarization calculated above in the present section, the G-AFM magnetic moment calculated in Sec. VA 2, and the low leakage current discussed in Sec. VB, as well as the convenient $P4mm$ symmetry for polarization switching strongly nominate the codoped composition as a possible multiferroic material.

VI. CONCLUSION

We have calculated and physically analyzed the structural, magnetical, optical, and electrical properties of the pristine BiFeO_3 , and its Ba-doped, as well as (Ba,F)-codoped compositions. The electronic calculations are performed in the framework of density functional theory employing full-potential APW + lo method using PBE-GGA + U with optimized U_{eff} parameters. For the optical calculations random phase approximation is employed. The calculations of the spontaneous electric polarization are performed in the framework of the modern theory of polarization using Berry phase approach. For the energy gap and magnetic moment calculations, in addition to PBE-GGA and PBE-GGA + U with various effective U parameters, a variety of mBJ exchange potentials, including the original TB-mBJ and its successors, KTB-mBJ, Sgap-KTB-mBJ, and JTSKTB-mBJ with their different self-consistently converged c parameters, as well as Ir-TB-mBJ with its different constrained c parameters are utilized for the pure compound. The accuracy of the calculations is assessed and due to the consistencies achieved with the experimental data, it is found that to an acceptable extent the experimental situations can be captured by the results presented in this work.

We have noticed that, so far, most of the available experimental energy gaps have been reported using optical techniques for the pure compound. Therefore, in addition to the electronic band gaps, optical gaps are also calculated for this material using all the above functionals. To this end, we obtain absorption spectra from our calculated extinction spectra. Furthermore, we similarly obtain absorption spectra from available experimental extinction spectra. Then, we using the Tauc method extract the optical gaps from the theoretical and experimental absorption spectra. Our calculated optical gaps using PBE-GGA + U with $U_{\text{eff}} = 4$ eV and TB-mBJ with its self-consistently converged $c = 1.38$ parameter are not only found in agreement with each other and our optical gaps extracted from the available experimental extinction spectra but also with another readily experimental optical gap already reported for the system in question.

Furthermore, we perform a systematic optical analysis to find the origins of the optical absorption and emission transi-

tions. To this end, we determine the differences between the peaks of all the valence and conduction partial densities of states taking selection rules into account to distinguish permitted transitions. Then, the transition energies are compared with the prominent peaks of the imaginary parts of dielectric spectra, and prominent peaks of the energy loss function, as well as to the band structure of the system to find the sources and types of the transitions. The rigorous analyses it is found that the prominent peaks of the parallel component of the imaginary parts of dielectric spectra can be attributed to O $2s$, O $2p$, Bi $6s$, Bi $6p$, Fe $3d$, and Fe $4s$ orbitals.

In this work, we have also found that the spontaneous electric and magnetic polarizations can satisfactorily coexist in the (Ba,F)-codoped composition. To realize the importance of the latter observation, it is essential to consider the problems of the pure BiFeO_3 crystal and the tasks performed here to ensure that the problems can be fixed by codoping, as the main motivations of this work.

Despite coexistence of spontaneous electric and antiferromagnetic polarizations simultaneously, the pure compound suffers from the following problems: (i) difficulty in synthesizing the stoichiometric BiFeO_3 , (ii) complex ferroelectric switching due to the $R3c$ structure [18], and (iii) high leakage current due to the volatile nature of Bi and change in iron valency, resulting in defects and reduction of the residual polarization [28,29]. To fix these problems, in Sec. V, we have inferred the following points: (i) both of the doped compositions have nonzero magnetic moments in agreement with experiment and thereby satisfy the first condition of being among the multiferroic materials, see Sec. VA 2. (ii) Both the doped compositions have nonzero band gaps consistent with the experimental data, as discussed in Sec. VA 3, and whence their electric polarizations, if any, can be calculated by the standard methods of polarization. (iii) The lone pair s -Bi is almost active stereochemically in the (Ba,F)-codoped composition and hence this composition has the capability to behave as a ferroelectric system which is not the case for the single-doped composition, see Sec. VA 4. (iv) The doped cases can reduce the leakage current, see Sec. VB. (v) The (Ba,F)-codoped (Ba-single-doped) composition can (cannot) form a ferroelectric material due to its tetragonal (pseudocubic) symmetry, see Sec. VA 1. The Ba-doped composition, due to its tiny polar distortion c/a of around 1.003 leading to the pseudocubic symmetry, cannot form a suitable ferroelectric material, see Sec. VA 1. (vi) Although spontaneous polarization of the (Ba,F)-codoped composition is not as large as that of the pure compound, the (Ba,F)-codoped composition with sufficient tetragonality, as shown in Sec. VA 1, and free of the pure compound problems, as discussed in Sec. V, still shows an acceptable ferroelectric polarization, as reported in Sec. VC 2.

The origin of the smaller polarization in the codoped composition is identified to mainly initiate from the different magnitudes and directions of the atomic displacements stemming from different atomic sizes and interactions of the Ba and F impurities compared to their corresponding hosts Bi and O.

All these evidences, as summarized above and discussed in details through Secs. VA 1 to VA 4, VB, VC 1, and VC 2, show that the codoped composition can constitute an appro-

appropriate multiferroic system and whence would be considered as a suitable alternative to the problematic pristine compound.

ACKNOWLEDGMENT

This work is partially supported by the University of Isfahan (UI).

APPENDIX: UNWRAPPING PROCEDURE

In the Berry phase scheme, the SEP, $\Delta\mathbf{P}$, along an adiabatic path is a multivalued quantity that can be only well defined modulo a quantum of polarization $e\mathbf{R}/\Omega$ [144], where \mathbf{R} , e , and Ω are defined in Sec. IV B. There can be such an uncertainty in polarization in the Berry phase approach. In this approach, a phase can be only well-defined modulo 2π . This implies that $\Delta\mathbf{P}$ can be defined uncertainly as $\mathbf{P}^{(\lambda=1)} - \mathbf{P}^{(\lambda=0)}$ modulo $e\mathbf{R}/\Omega$ [144,146–148]. The definition “ $\Delta\mathbf{P} := \mathbf{P}^{(\lambda=1)} - \mathbf{P}^{(\lambda=0)}$ (mod $e\mathbf{R}/\Omega$)” reads as “ $\Delta\mathbf{P}$ and $\mathbf{P}^{(\lambda=1)} - \mathbf{P}^{(\lambda=0)}$ are congruent modulo $e\mathbf{R}/\Omega$.” This implies that $\Delta\mathbf{P}$ and $\mathbf{P}^{(\lambda=1)} - \mathbf{P}^{(\lambda=0)}$ can be different but equivalent in mod $e\mathbf{R}/\Omega$ as they have the same remainder when divided by $e\mathbf{R}/\Omega$. In this definition, $\Delta\mathbf{P}$ is an actual quantity that can be observed and measured experimentally while $\mathbf{P}^{(\lambda=1)} - \mathbf{P}^{(\lambda=0)}$ is a successor quantity proposed by the modern theory of polarization [144,146–153] that may not be necessarily equal to the actual quantity. In other words, computing $\mathbf{P}^{(\lambda=1)} - \mathbf{P}^{(\lambda=0)}$ by the endpoints of the path only, may not always lead to the actual $\Delta\mathbf{P}$. This is due to the fact that there is no guarantee that the successor spontaneous polarization $\mathbf{P}^{(\lambda=1)} - \mathbf{P}^{(\lambda=0)}$ is the result of using the correct branch, if we only consider the endpoints of the path without making sure about the correctness of the branch [144]. Therefore, we have considered the uncertainty problem to uniquely obtain the spontaneous polarizations of pure BiFeO₃ compound and its (Ba,F)-codoped composition, as to be discussed subsequently. It is worth to mention that the uncertainty problem is more important in perovskite compounds. For the cases under study, the polarizations $\mathbf{P}^{(\lambda=0)}$ and $\mathbf{P}^{(\lambda=1)}$ and consequently the spontaneous

polarization $\Delta\mathbf{P}$ are oriented along the c axes of the tetragonal noncentrosymmetric (NCS) supercells. Therefore, for these cases, \mathbf{R} employed in $e\mathbf{R}/\Omega$ can be simplified as $\mathbf{R} = n c \hat{\mathbf{k}}$ so that $|\mathbf{R}| = R = nc$, where n is an integer number and c ($\hat{\mathbf{k}}$) is the lattice constant (unit vector) along the Cartesian z axis. Hence, the above definition can be represented as $\Delta\mathbf{P} := \mathbf{P}^{(\lambda=1)} - \mathbf{P}^{(\lambda=0)} + enc\hat{\mathbf{k}}/\Omega$ or equivalently as $\Delta P \hat{\mathbf{k}} := P^{(\lambda=1)}\hat{\mathbf{k}} - P^{(\lambda=0)}\hat{\mathbf{k}} + enc\hat{\mathbf{k}}/\Omega$, where $\Delta P = |\Delta\mathbf{P}|$, $P^{(\lambda=1)} = |\mathbf{P}^{(\lambda=1)}|$, and $P^{(\lambda=0)} = |\mathbf{P}^{(\lambda=0)}|$. By taking a dot product of the latter vector identity with the unit vector $\hat{\mathbf{k}}$, it can be simplified to its scalar form $\Delta P := P^{(\lambda=1)} - P^{(\lambda=0)} + enc/\Omega$. Therefore, the basic task to identify ΔP uniquely is reduced to determine the integer number n for these cases with polarization oriented along one-dimension only. We do it below by the procedure proposed in Ref. [144]. To this end, in addition to the starting structure “ $\lambda = 0$ ” and end structure “ $\lambda = 1$ ”, as the two endpoints of the adiabatic transition, we have constructed 3 intermediate superstructures $\lambda = 0.25, 0.50$, and 0.75 . In this way, we find a chance to identify a sudden change (jump), if any, in the calculated polarization at an intermediate distorted structure compared to its previous and next structures. If a jump (ascent or descent) occurs, we modify it to make smooth the path by shifting the jumped polarization, i.e., pulling downward the ascent polarization or pushing upwards the descent polarization, using a negative or positive integer multiple of the quantum of polarization, as practically discussed below. In fact, by this way, we unwrap the polarizations (Berry phases) of the constructed structures step by step which are by default traditionally wrapped regardless of spin into the interval $[-e\mathbf{R}/2\Omega, e\mathbf{R}/2\Omega] \equiv [-enc/2\Omega, enc/2\Omega]$ ($[-\pi, \pi]$). For spin polarized systems, a fact of 2 is considered.

To set up the G-AFM phase of the tetragonal BiFeO₃, we construct a $1 \times 2 \times 2$ supercell, as shown in Fig. 15(a). Electronic and ionic parts of polarization as two functions of parameter λ are individually shown in Fig. 15(b). The adiabatic transition of BiFeO₃ starts from the centrosymmetric nonpolar cubic structure, $\lambda = 0$, and terminates to the noncentrosymmetric polar tetragonal structure, $\lambda = 1$. Endpoints of the path indicated by $\lambda = 0$ and $\lambda = 1$ are not

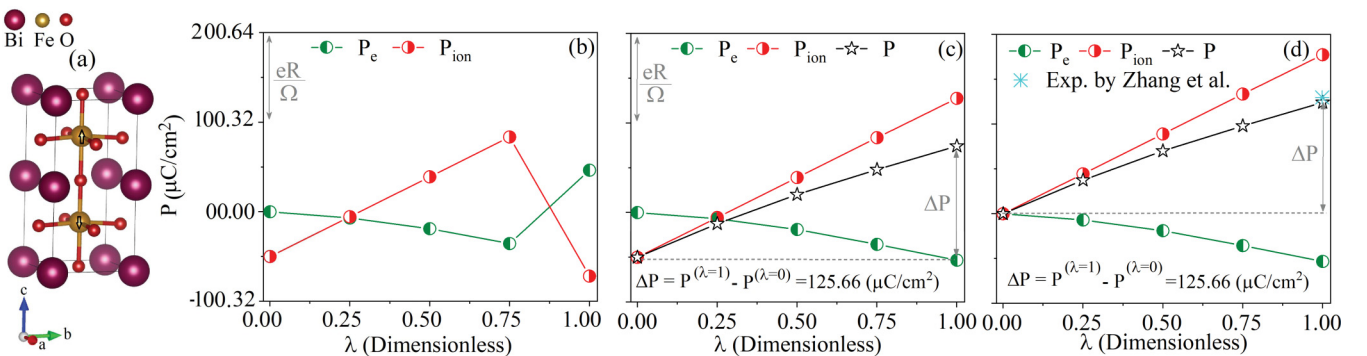


FIG. 15. (a) The $1 \times 1 \times 2$ supercell used to calculate SEP using DFT plus Berry phase theory employing PBE-GGA + U + SOC with $U_{\text{eff}} = 4$ eV for the tetragonal phase of BiFeO₃, (b) electronic part of the polarization (P_e) and ionic part of the polarization (P_{ion}) as functions of dimensionless λ parameter, (c) the latter P_e and P_{ion} paths after smoothing them by subtracting (adding) proper quantum of polarization from the ascent (to the descent) polarization together with the resultant total polarization, $P = P_e + P_{ion}$, and (d) the latter smoothed P_e and P_{ion} paths after shifting them so that they start from zero, *viz.*, the unwrapped P_e and P_{ion} paths. The quantum of polarization, $e\mathbf{R}/\Omega = 100.32 \mu\text{C}/\text{cm}^2$, and the SEP, $\Delta P = P^{(\lambda=1)} - P^{(\lambda=0)} = 125.66 \mu\text{C}/\text{cm}^2$, are indicated and/or expressed. The experimental datum extracted from Ref. [50] is also indicated for comparison.

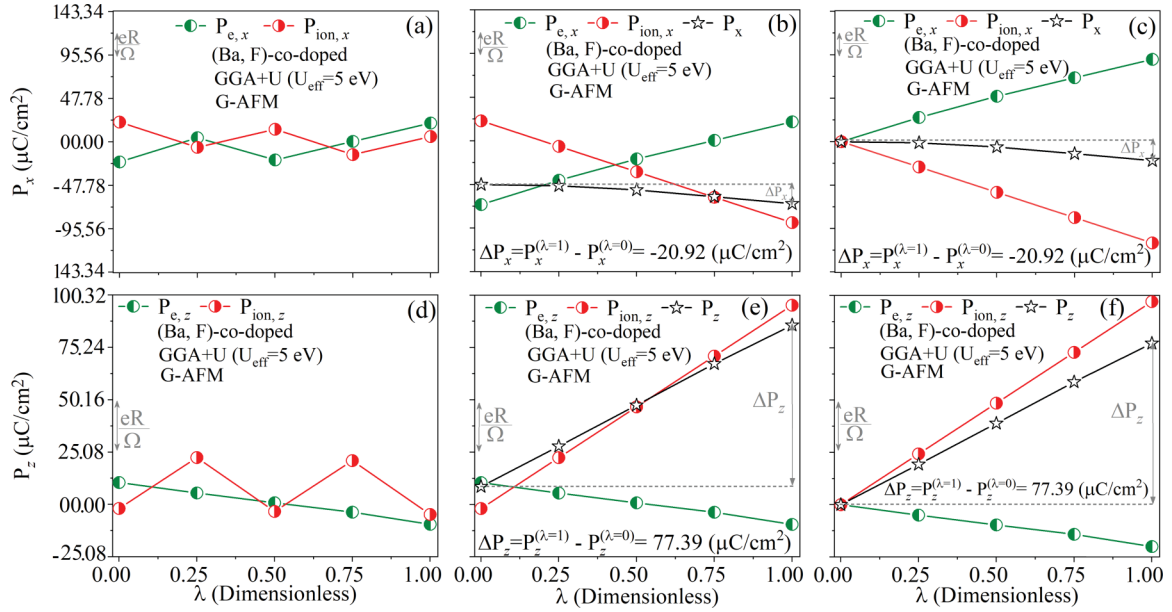


FIG. 16. Unwrapping procedure of the polarization calculated by DFT + Berry phase theory using PBE-GGA + U + SOC with $U_{\text{eff}} = 5$ eV for the (Ba,F)-doped composition. (a) Wrapped traverse x components of the electronic part of the polarization ($P_{e,x}$) and ionic part of the polarization ($P_{\text{ion},x}$) as functions of dimensionless λ parameter, (b) unwrapped $P_{e,x}$ and $P_{\text{ion},x}$ paths together with the resultant total polarization, $P_x = P_{e,x} + P_{\text{ion},x}$, (c) the shifted unwrapped $P_{e,x}$, $P_{\text{ion},x}$, and P_x paths, (d) wrapped longitudinal z components of the electronic part of the polarization ($P_{e,z}$) and ionic part of the polarization ($P_{\text{ion},z}$) as functions of dimensionless λ parameter, (e) unwrapped $P_{e,z}$ and $P_{\text{ion},z}$ paths together with the resultant total polarization, $P_z = P_{e,z} + P_{\text{ion},z}$, and (f) the shifted unwrapped $P_{e,z}$, $P_{\text{ion},z}$, and P_z paths. The quantum of polarizations in x direction, $eR/\Omega = 23.89 \mu\text{C}/\text{cm}^2$, and in z direction, $eR/\Omega = 25.08 \mu\text{C}/\text{cm}^2$, as well as the SEPs in x direction, $\Delta P_x = P_x^{(\lambda=1)} - P_x^{(\lambda=0)} = -20.92 \mu\text{C}/\text{cm}^2$, and in z direction, $\Delta P_z = P_z^{(\lambda=1)} - P_z^{(\lambda=0)} = 77.39 \mu\text{C}/\text{cm}^2$, are expressed.

always sufficient to ensure that the branch is chosen correctly. To this end, in addition to the initial structure $\lambda = 0$ and final structure $\lambda = 1$, we have considered three intermediate structures. These intermediate structures are indicated by $\lambda = 0.25, 0.50$, and 0.75 . The results show that P_e (P_{ion}) smoothly increases (decreases) as λ increases from 0 to 0.75, but an ascent (descent) jump occurs from $\lambda = 0.75$ to 1, see Fig. 15(b). Therefore, in order to make smooth the electronic and ionic paths, we pull (push) downward the ascent (upwards the descent) polarization, as shown in Fig. 15(c). To this end, we subtract (add) appropriate quantum of polarization from the ascent (to the descent) polarization, where the quantum of polarization is calculated to be $eR/\Omega = 100.32 \mu\text{C}/\text{cm}^2$ for $1 \times 1 \times 2$ supercell, see Fig. 15(c). The total polarization, i.e., $P = P_e + P_{\text{ion}}$, is also shown in Fig. 15(c). Without loss of generality, for convenience only, we displace the origins of P_{ion} and P paths and thereby entirely shift them so that they start from zero, as shown in Fig. 15(d). These shifts by constant values do not change the results, because the spontaneous polarization as the final important physical quantity is obtained from the difference between the polarizations calculated at the starting and ending structures, $\Delta P = P^{(\lambda=1)} - P^{(\lambda=0)}$, so that any constant shifts are canceled out. By this way, the spontaneous electric polarization is calculated to be $\Delta P = P^{(\lambda=1)} - P^{(\lambda=0)} = 125.66 \mu\text{C}/\text{cm}^2$ for the tetragonal BiFeO_3 compound, see Fig. 15(d) and Table VI.

The electric polarization of tetragonal (Ba,F)-codoped composition is calculated by the DFT plus Berry phase approach using GGA + U with $U_{\text{eff}} = 5$ eV. In this case, in ad-

dition to the longitudinal polarization (P_{\parallel}) along the tetragonal $c(\equiv z)$ direction, we find also a nonzero transverse polarization (P_{\perp}) along the tetragonal $a(\equiv x)$ direction only, whereas P_{\perp} along the tetragonal $b(\equiv y)$ direction still vanishes. In the transverse (longitudinal) direction of the codoped structure, the wrapped electronic polarization, $P_{e,x}$ ($P_{e,z}$), and ionic polarization, $P_{\text{ion},x}$ ($P_{\text{ion},z}$), are shown in Fig. 16(a) [Fig. 16(d)]. The paths of $P_{e,x}$, $P_{\text{ion},x}$, $P_{\text{ion},z}$ show zigzag behaviors from $\lambda = 0$ to 1, while the path of $P_{e,z}$ smoothly decreases as λ increases from 0 to 1, see Figs. 16(a) and 16(d). Therefore, the smooth $P_{e,z}$ path is left unchanged, while the zigzag paths are made smooth by pulling (pushing) downward the ascent (upwards the descent) jumped polarizations, as shown in Figs. 16(b) and 16(e). To this end, we subtract (add) needed quantum of polarizations from the ascent (to the descent) polarizations, where the quantum of polarizations are calculated to be $eR/\Omega = 23.89$ and $25.08 \mu\text{C}/\text{cm}^2$ for x and z directions, respectively, see Figs. 16(b) and (e). The x component of the total polarization, i.e., $P_x = P_{e,x} + P_{\text{ion},x}$, is also shown in Fig. 15(b). Similarly, the z component of the total polarization, i.e., $P_z = P_{e,z} + P_{\text{ion},z}$, is also shown in Fig. 15(e). In analogous to the pure case, here, we also displace the origins of paths and thereby entirely shift them so that all the paths start from zero, as shown in Figs. 16(c) and (f). By this way, the x component of the spontaneous electric polarization is calculated to be $\Delta P_x = P_x^{(\lambda=1)} - P_x^{(\lambda=0)} = -20.92 \mu\text{C}/\text{cm}^2$ for the tetragonal (Ba,F)-codoped composition, see Fig. 16(c). Similarly, the z component of the spontaneous electric polarization is calculated to be $\Delta P_z = P_z^{(\lambda=1)} - P_z^{(\lambda=0)} = 77.39 \mu\text{C}/\text{cm}^2$ for the

tetragonal (Ba,F)-codoped composition, see Fig. 16(f). The results show that the longitudinal component of the polarization is about 3.7 larger than the magnitude of the transverse component of the polarization. Finally, let us conclude

this Appendix by reporting the total SEP of the (Ba,F)-multidoped composition to be $\Delta P = \sqrt{(\Delta P_x)^2 + (\Delta P_z)^2} \approx \sqrt{(-20.92)^2 + (77.39)^2} \approx 80.17 \mu\text{C}/\text{cm}^2$, as represented in Table VI.

- [1] M. Fiebig, T. Lottermoser, D. Meier, and M. Trassin, The evolution of multiferroics, *Nat. Rev. Mater.* **1**, 16046 (2016).
- [2] S.-W. Cheong and M. Mostovoy, Multiferroics: a magnetic twist for ferroelectricity, *Nat. Mater.* **6**, 13 (2007).
- [3] Y. Tokura and S. Seki, Multiferroics with spiral spin orders, *Adv. Mater.* **22**, 1554 (2010).
- [4] Y. Heo and M. Alexe, Boosting piezoelectricity under illumination via the bulk photovoltaic effect and the Schottky barrier effect in BiFeO₃, *Adv. Mater.* **34**, 2105845 (2022).
- [5] A. Jana, S. Rane, P. R. Choudhury, and D. R. Chowdhury, External bias dependent dynamic terahertz propagation through BiFeO₃ film, *Nanotechnology* **33**, 325202 (2022).
- [6] N. Parvathy and R. Govindaraj, Atomic scale insights on the growth of BiFeO₃ nanoparticles, *Sci. Rep.* **12**, 4758 (2022).
- [7] Y. Sun, X. Li, A. Vijayakumar, H. Liu, C. Wang, S. Zhang, Z. Fu, Y. Lu, and Z. Cheng, Hydrogen generation and degradation of organic dyes by new piezocatalytic 0.7 BiFeO₃-0.3 BaTiO₃ nanoparticles with proper band alignment, *ACS Appl. Mater. Interfaces* **13**, 11050 (2021).
- [8] J. Suh, J. S. Lim, H.-S. Park, and C.-H. Yang, Complementary study of anisotropic ion conduction in (110)-oriented Ca-doped BiFeO₃ films using electrochromism and impedance spectroscopy, *Appl. Phys. Lett.* **119**, 022902 (2021).
- [9] P. Lv, J. Qian, C. Yang, Y. Wang, W. Wang, S. Huang, X. Cheng, and Z. Cheng, 4-inch ternary BiFeO₃ - BaTiO₃ - SrTiO₃ thin film capacitor with high energy storage performance, *ACS Energy Lett.* **6**, 3873 (2021).
- [10] J. Scott, Multiferroic memories, *Nat. Mater.* **6**, 256 (2007).
- [11] S. M. Yakout, Spintronics and innovative memory devices: a review on advances in magnetoelectric BiFeO₃, *J. Supercond. Novel Magn.* **34**, 317 (2021).
- [12] I. Sosnowska, T. P. Neumaier, and E. Steichele, Spiral magnetic ordering in bismuth ferrite, *J. Phys. C* **15**, 4835 (1982).
- [13] T. Zhao, A. Scholl, F. Zavaliche, K. Lee, M. Barry, A. Doran, M. Cruz, Y. Chu, C. Ederer, N. Spaldin *et al.*, Electrical control of antiferromagnetic domains in multiferroic BiFeO₃ films at room temperature, *Nat. Mater.* **5**, 823 (2006).
- [14] S. M. Selbach, T. Tybell, M.-A. Einarsrud, and T. Grande, The ferroic phase transitions of BiFeO₃, *Adv. Mater.* **20**, 3692 (2008).
- [15] D. Lebeugle, D. Colson, A. Forget, and M. Viret, Very large spontaneous electric polarization in BiFeO₃ single crystals at room temperature and its evolution under cycling fields, *Appl. Phys. Lett.* **91**, 022907 (2007).
- [16] J. B. Neaton, C. Ederer, U. V. Waghmare, N. A. Spaldin, and K. M. Rabe, First-principles study of spontaneous polarization in multiferroic BiFeO₃, *Phys. Rev. B* **71**, 014113 (2005).
- [17] V. V. Shvartsman, W. Kleemann, R. Haumont, and J. Kreisel, Large bulk polarization and regular domain structure in ceramic BiFeO₃, *Appl. Phys. Lett.* **90**, 172115 (2007).
- [18] M. N. Iliiev, M. V. Abrashev, D. Mazumdar, V. Shelke, and A. Gupta, Polarized raman spectroscopy of nearly tetragonal BiFeO₃ thin films, *Phys. Rev. B* **82**, 014107 (2010).
- [19] J. Silva, A. Reyes, H. Esparza, H. Camacho, and L. Fuentes, BiFeO₃: A review on synthesis, doping and crystal structure, *Integrated Ferroelectrics* **126**, 47 (2011).
- [20] Y. Zhao, Z. Yin, X. Li, M. Zheng, Y. Cheng, J. You, J. Wu, and X. Zhang, Metastable tetragonal BiFeO₃ stabilized on anisotropic a-plane ZnO, *Cryst. Growth Des.* **21**, 4372 (2021).
- [21] A. Makhdoom, M. Akhtar, M. Rafiq, and M. Hassan, Investigation of transport behavior in Ba doped BiFeO₃, *Ceram. Int.* **38**, 3829 (2012).
- [22] N. Setter, What is a ferroelectric-a materials designer perspective, *Ferroelectrics* **500**, 164 (2016).
- [23] C. Ederer and N. A. Spaldin, Effect of Epitaxial Strain on the Spontaneous Polarization of Thin Film Ferroelectrics, *Phys. Rev. Lett.* **95**, 257601 (2005).
- [24] A. J. Hatt, N. A. Spaldin, and C. Ederer, Strain-induced isosymmetric phase transition in BiFeO₃, *Phys. Rev. B* **81**, 054109 (2010).
- [25] R. Zeches, M. Rossell, J. Zhang, A. Hatt, Q. He, C.-H. Yang, A. Kumar, C. Wang, A. Melville, C. Adamo *et al.*, A strain-driven morphotropic phase boundary in BiFeO₃, *Science* **326**, 977 (2009).
- [26] O. Clemens, R. Kruk, E. A. Patterson, C. Loho, C. Reitz, A. J. Wright, K. S. Knight, H. Hahn, and P. R. Slater, Introducing a large polar tetragonal distortion into Ba-doped BiFeO₃ by low-temperature fluorination, *Inorg. Chem.* **53**, 12572 (2014).
- [27] A. Sinha, B. Bhushan, R. Sharma, S. Sen, B. Mandal, S. Meena, P. Bhatt, C. Prajapat, A. Priyam, S. Mishra *et al.*, Enhanced dielectric, magnetic and optical properties of Cr-doped BiFeO₃ multiferroic nanoparticles synthesized by sol-gel route, *Results Phys.* **13**, 102299 (2019).
- [28] S. Pradhan and B. Roul, Improvement of multiferroic and leakage property in monophasic BiFeO₃, *Phys. B: Condens. Matter* **406**, 3313 (2011).
- [29] X. Ren, G. Tan, J. Li, Y. Liu, M. Xue, H. Ren, A. Xia, and W. Liu, Mechanism for enhanced ferroelectricity in multi-doped BiFeO₃ thin films, *J. Mater. Sci.: Mater. Electron.* **32**, 1265 (2021).
- [30] Z. Cheng, X. Wang, S. Dou, H. Kimura, and K. Ozawa, Improved ferroelectric properties in multiferroic BiFeO₃ thin films through La and Nb codoping, *Phys. Rev. B* **77**, 092101 (2008).
- [31] S. G. Choi, H. T. Yi, S.-W. Cheong, J. N. Hilfiker, R. France, and A. G. Norman, Optical anisotropy and charge-transfer transition energies in BiFeO₃ from 1.0 to 5.5 eV, *Phys. Rev. B* **83**, 100101(R) (2011).
- [32] K. Liu, H. Fan, P. Ren, and C. Yang, Structural, electronic and optical properties of BiFeO₃ studied by first-principles, *J. Alloys Compd.* **509**, 1901 (2011).
- [33] A. Lima, Optical properties, energy band gap and the charge carriers effective masses of the R3c BiFeO₃ magnetoelectric compound, *J. Phys. Chem. Solids* **144**, 109484 (2020).
- [34] M. Berry, Classical adiabatic angles and quantal adiabatic phase, *J. Phys. A: Math. Gen.* **18**, 15 (1985).

- [35] S. Ahmed, J. Kivinen, B. Zaporzan, L. Curiel, S. Pichardo, and O. Rubel, BerryPI: A software for studying polarization of crystalline solids with WIEN2k density functional all-electron package, *Comput. Phys. Commun.* **184**, 647 (2013).
- [36] D. Vanderbilt, Berry-phase theory of proper piezoelectric response, *J. Phys. Chem. Solids* **61**, 147 (2000).
- [37] M. V. Berry, Quantal phase factors accompanying adiabatic changes, *Proc. R. Soc. A* **392**, 45 (1984).
- [38] D. Xiao, M.-C. Chang, and Q. Niu, Berry phase effects on electronic properties, *Rev. Mod. Phys.* **82**, 1959 (2010).
- [39] J. Ihlefeld, N. Podraza, Z. Liu, R. Rai, X. Xu, T. Heeg, Y. Chen, J. Li, R. Collins, J. Musfeldt *et al.*, Optical band gap of BiFeO₃ grown by molecular-beam epitaxy, *Appl. Phys. Lett.* **92**, 142908 (2008).
- [40] F. Tran and P. Blaha, Accurate Band Gaps of Semiconductors and Insulators with a Semilocal Exchange-Correlation Potential, *Phys. Rev. Lett.* **102**, 226401 (2009).
- [41] D. Koller, F. Tran, and P. Blaha, Merits and limits of the modified Becke-Johnson exchange potential, *Phys. Rev. B* **83**, 195134 (2011).
- [42] D. Koller, F. Tran, and P. Blaha, Improving the modified Becke-Johnson exchange potential, *Phys. Rev. B* **85**, 155109 (2012).
- [43] R. A. Jishi, O. B. Ta, and A. A. Sharif, Modeling of lead halide perovskites for photovoltaic applications, *J. Phys. Chem. C* **118**, 28344 (2014).
- [44] M. Yazdanmehr, S. J. Asadabadi, A. Nourmohammadi, M. Ghasemzadeh, and M. Rezvanian, Electronic structure and band gap of Al₂O₃ compound using mBJ exchange potential, *Nanoscale Res. Lett.* **7**, 488 (2012).
- [45] J. Tauc, R. Grigorovici, and A. Vancu, Optical properties and electronic structure of amorphous germanium, *Phys. Status Solidi (b)* **15**, 627 (1966).
- [46] P. Makuła, M. Pacia, and W. Macyk, How to correctly determine the band gap energy of modified semiconductor photocatalysts based on UV-Vis spectra, *J. Phys. Chem. Lett.* **9**, 6814 (2018).
- [47] A. Ali, I. Khan, Z. Ali, F. Khan, and I. Ahmad, First-principles study of BiFeO₃ and BiTiO₃ in tetragonal structure, *Int. J. Mod. Phys. B* **33**, 1950231 (2019).
- [48] Y. Zhang, J. Sun, J. P. Perdew, and X. Wu, Comparative first-principles studies of prototypical ferroelectric materials by LDA, GGA, and SCAN meta-GGA, *Phys. Rev. B* **96**, 035143 (2017).
- [49] M. Pugaczowa-Michalska and J. Kaczkowski, First-principles study of structural, electronic, and ferroelectric properties of rare-earth-doped BiFeO₃, *J. Mater. Sci.* **50**, 6227 (2015).
- [50] J. X. Zhang, Q. He, M. Trassin, W. Luo, D. Yi, M. D. Rossell, P. Yu, L. You, C. H. Wang, C. Y. Kuo, J. T. Heron, Z. Hu, R. J. Zeches, H. J. Lin, A. Tanaka, C. T. Chen, L. H. Tjeng, Y.-H. Chu, and R. Ramesh, Microscopic Origin of the Giant Ferroelectric Polarization in Tetragonal-Like BiFeO₃, *Phys. Rev. Lett.* **107**, 147602 (2011).
- [51] D. Lebeugle, D. Colson, A. Forget, M. Viret, A. M. Bataille, and A. Gukasov, Electric-Field-Induced Spin Flop in BiFeO₃ Single Crystals at Room Temperature, *Phys. Rev. Lett.* **100**, 227602 (2008).
- [52] F. Kubel and H. Schmid, Structure of a ferroelectric and ferroelastic monodomain crystal of the perovskite BiFeO₃, *Acta Crystallogr., Sect. B: Struct. Sci.* **46**, 698 (1990).
- [53] P. Blaha, K. Schwarz, G. K. H. Madsen, D. Kvasnicka, J. Luitz, R. Laskowski, F. Tran, and L. D. Marks, WIEN2K, *An Augmented Plane Wave + Local Orbitals Program for Calculating Crystal Properties* (Karlheinz Schwarz, Technische Universität Wien, Vienna, Austria, 2021).
- [54] S. Vijayanand, H. S. Potdar, and P. A. Joy, Origin of high room temperature ferromagnetic moment of nanocrystalline multiferroic BiFeO₃, *Appl. Phys. Lett.* **94**, 182507 (2009).
- [55] J. L. Ortiz-Quiñonez, D. Déaz, I. Zumeta-Dubé, H. Arriola-Santamaría, I. Betancourt, P. Santiago-Jacinto, and N. Navat-Etzana, Easy synthesis of high-purity BiFeO₃ nanoparticles: New insights derived from the structural, optical, and magnetic characterization, *Inorg. Chem.* **52**, 10306 (2013).
- [56] J. Peñalva and A. Lazo, Synthesis of bismuth ferrite BiFeO₃ by solution combustion method, *J. Phys.: Conf. Ser.* **1143**, 012025 (2018).
- [57] M. Benyoussef, S. Saitzek, N. S. Rajput, M. Courty, M. El Marssi, and M. Jouiad, Experimental and theoretical investigations of low-dimensional BiFeO₃ system for photocatalytic applications, *Catalysts* **12**, 215 (2022).
- [58] S. K. Singh and H. Ishiwara, Reduced leakage current in BiFeO₃ thin films on Si substrates formed by a chemical solution method, *Jpn. J. Appl. Phys.* **44**, L734 (2005).
- [59] S. Habouti, C.-H. Solterbeck, and M. Es-Souni, Uv assisted pyrolysis of solution deposited BiFeO₃ multiferroic thin films. Effects on microstructure and functional properties, *J. Sol-Gel Sci. Technol.* **42**, 257 (2007).
- [60] A. Lahmar, K. Zhao, S. Habouti, M. Dietze, C.-H. Solterbeck, and M. Es-Souni, Off-stoichiometry effects on BiFeO₃ thin films, *Solid State Ionics* **202**, 1 (2011).
- [61] J. Park, S.-H. Lee, S. Lee, F. Gozzo, H. Kimura, Y. Noda, Y. Jai Choi, V. Kiryukhin, S.-W. Cheong, Y. Jo, E. Sang Choi, L. Balicas, G. Sang Jeon, and J.-G. Park, Magnetoelectric feedback among magnetic order, polarization, and lattice in multiferroic BiFeO₃, *J. Phys. Soc. Jpn.* **80**, 114714 (2011).
- [62] P. Hohenberg and W. Kohn, Inhomogeneous electron gas, *Phys. Rev.* **136**, B864 (1964).
- [63] W. Kohn and L. J. Sham, Self-consistent equations including exchange and correlation effects, *Phys. Rev.* **140**, A1133 (1965).
- [64] K. Schwarz, P. Blaha, and G. K. Madsen, Electronic structure calculations of solids using the WIEN2k package for material sciences, *Comput. Phys. Commun.* **147**, 71 (2002).
- [65] P. Blaha, K. Schwarz, F. Tran, R. Laskowski, G. K. H. Madsen, and L. D. Marks, WIEN2k: An APW + lo program for calculating the properties of solids, *J. Chem. Phys.* **152**, 074101 (2020).
- [66] J. P. Perdew, K. Burke, and M. Ernzerhof, Generalized Gradient Approximation Made Simple, *Phys. Rev. Lett.* **77**, 3865 (1996).
- [67] V. I. Anisimov, I. V. Solovyev, M. A. Korotin, M. T. Czyżyk, and G. A. Sawatzky, Density-functional theory and NiO photoemission spectra, *Phys. Rev. B* **48**, 16929 (1993).
- [68] Y. Kohori, Y. Inoue, T. Kohara, G. Tomka, and P. Riedi, ¹¹⁵In NQR study with evidence for two magnetic quantum critical points in dual Ce site superconductor Ce₃PtIn₁₁, *Phys. B: Condens. Matter* **259-261**, 103 (1999).
- [69] S. J. Asadabadi and F. Kheradmand, Ab initio prediction of magnetically dead layers in freestanding γ -Ce(111), *J. Appl. Phys.* **108**, 073531 (2010).

- [70] M. Yazdani-Kachoei, S. Rahimi, R. Ebrahimi-Jaberi, J. Nematollahi, and S. Jalali-Asadabadi, Thermoelectric properties plus phonon and de Haas–van Alphen frequencies of hole/electron-doped CeIn_3 , *Sci. Rep.* **12**, 663 (2022).
- [71] M. Yazdani-Kachoei, S. Jalali-Asadabadi, I. Ahmad, and K. Zarringhalam, Pressure dependency of localization degree in heavy fermion CeIn_3 : A density functional theory analysis, *Sci. Rep.* **6**, 31734 (2016).
- [72] S. Jalali-Asadabadi, Electronic structure and electric-field gradient analysis in CeIn_3 , *Phys. Rev. B* **75**, 205130 (2007).
- [73] S. J. Asadabadi, S. Cottenier, H. Akbarzadeh, R. Saki, and M. Rots, Valency of rare earths in RIn_3 and RSn_3 : *Ab initio* analysis of electric-field gradients, *Phys. Rev. B* **66**, 195103 (2002).
- [74] M. Shafiq, M. Yazdani-Kachoei, S. Jalali-Asadabadi, and I. Ahmad, Electric field gradient analysis of RIn_3 and RSn_3 compounds ($\text{R} = \text{La}, \text{Ce}, \text{Pr}$ and Nd), *Intermetallics* **91**, 95 (2017).
- [75] M. Di Ventura and S. T. Pantelides, Hellmann-Feynman theorem and the definition of forces in quantum time-dependent and transport problems, *Phys. Rev. B* **61**, 16207 (2000).
- [76] S. Jalali-Asadabadi, E. Ghasemikhah, T. Ouahrani, B. Nourozi, M. Bayat-Bayatani, S. Javanbakht, H. A. R. Aliabad, I. Ahmad, J. Nematollahi, and M. Yazdani-Kachoei, Electronic structure of crystalline buckyballs: fcc- C_{60} , *J. Electron. Mater.* **45**, 339 (2016).
- [77] M. Yazdanmehr, S. Jalali-Asadabadi, J. Nematollahi, A. Nourmohammadi, and I. Ahmad, Predictions of band gap and subbands of $\gamma\text{-Al}_2\text{O}_3$ in presence of intrinsic point defects by DFT+TB-mBJ, *Computational Condensed Matter* **19**, e00379 (2019).
- [78] G. Rehman, M. Shafiq, Saifullah, R. Ahmad, S. Jalali-Asadabadi, M. Maqbool, I. Khan, H. Rahnamaye-Aliabad, and I. Ahmad, Electronic band structures of the highly desirable III–V semiconductors: TB-mBJ DFT studies, *J. Electron. Mater.* **45**, 3314 (2016).
- [79] G. Onida, L. Reining, and A. Rubio, Electronic excitations: density-functional versus many-body Green’s-function approaches, *Rev. Mod. Phys.* **74**, 601 (2002).
- [80] M. S. Dresselhaus, Solid state physics; PART II: Optical properties of solids (2001), <https://web.mit.edu/6.732/www/opt.pdf>.
- [81] Q. Chen, A. R. Kutayiah, I. Oladyshkin, M. Tokman, and A. Belyanin, Optical properties and electromagnetic modes of Weyl semimetals, *Phys. Rev. B* **99**, 075137 (2019).
- [82] C. Ambrosch-Draxl and J. O. Sofo, Linear optical properties of solids within the full-potential linearized augmented plane-wave method, *Comput. Phys. Commun.* **175**, 1 (2006).
- [83] H. Papi, S. Jalali-Asadabadi, A. Nourmohammadi, I. Ahmad, J. Nematollahi, and M. Yazdanmehr, Optical properties of ideal $\gamma\text{-Al}_2\text{O}_3$ and with oxygen point defects: An *ab initio* study, *RSC Advances* **5**, 55088 (2015).
- [84] Q.-Y. Rong, W.-Z. Xiao, C.-P. Cheng, and L.-L. Wang, Magnetism and ferroelectricity in BiFeO_3 doped with Ga at Fe sites, *J. Alloys Compd.* **797**, 117 (2019).
- [85] V. Khomchenko, D. Kiselev, E. Selezneva, J. Vieira, A. Lopes, Y. Pogorelov, J. Araujo, and A. Kholkin, Weak ferromagnetism in diamagnetically-doped $\text{Bi}_{1-x}\text{A}_x\text{FeO}_3$ ($\text{A} = \text{Ca}, \text{Sr}, \text{Pb}, \text{Ba}$) multiferroics, *Mater. Lett.* **62**, 1927 (2008).
- [86] S. W. Bae, P. H. Borse, and J. S. Lee, Dopant dependent band gap tailoring of hydrothermally prepared cubic $\text{SrTi}_x\text{M}_{1-x}\text{O}_3$ ($\text{M} = \text{Ru}, \text{Rh}, \text{Ir}, \text{Pt}, \text{Pd}$) nanoparticles as visible light photocatalysts, *Appl. Phys. Lett.* **92**, 104107 (2008).
- [87] H. K. Chandra, K. Gupta, A. K. Nandy, and P. Mahadevan, Ferroelectric distortions in doped ferroelectrics: $\text{BaTiO}_3\text{:M}$ ($\text{M}=\text{V-Fe}$), *Phys. Rev. B* **87**, 214110 (2013).
- [88] A. Ghosh, D. P. Trujillo, H. Choi, S. M. Nakhmanson, S. P. Alpay, and J.-X. Zhu, Electronic and magnetic properties of lanthanum and strontium doped bismuth ferrite: A first-principles study, *Sci. Rep.* **9**, 194 (2019).
- [89] M. Kaur, K. Yadav, and P. Uniyal, Multiferroic and optical studies on the effects of Bi^{2+} ions in BiFeO_3 nanoparticles, *J. Mater. Sci.: Mater. Electron.* **27**, 4475 (2016).
- [90] N. Manjula, K. S. Kumar, M. Ramanadha, A. S. Rani, and R. Vijayalakshmi, The effect of Ba doping on the structural, optical, magnetic, and dielectric properties of BiFeO_3 nanoparticles, *J. Supercond. Novel Magn.* **31**, 3043 (2018).
- [91] E. Djatoubai, M. S. Khan, S. ul Haq, P. Guo, and S. Shen, BiFeO_3 band gap engineering by dopants and defects control for efficient photocatalytic water oxidation, *Applied Catalysis A: General* **643**, 118737 (2022).
- [92] C.-H. Yang, D. Kan, I. Takeuchi, V. Nagarajan, and J. Seidel, Doping BiFeO_3 : approaches and enhanced functionality, *Phys. Chem. Chem. Phys.* **14**, 15953 (2012).
- [93] L. Hedin, New method for calculating the one-particle Green’s function with application to the electron-gas problem, *Phys. Rev.* **139**, A796 (1965).
- [94] W. G. Aulbur, L. Jönsson, and J. W. Wilkins, Quasiparticle calculations in solids, *Solid State Phys.* **54**, 1 (2000).
- [95] F. Aryasetiawan and O. Gunnarsson, The GW method, *Rep. Prog. Phys.* **61**, 237 (1998).
- [96] K. Haule, Exact Double Counting in Combining the Dynamical Mean Field Theory and the Density Functional Theory, *Phys. Rev. Lett.* **115**, 196403 (2015).
- [97] L. G. Ferreira, M. Marques, and L. K. Teles, Slater half-occupation technique revisited: the LDA – 1/2 and GGA – 1/2 approaches for atomic ionization energies and band gaps in semiconductors, *AIP Adv.* **1**, 032119 (2011).
- [98] R. Rodrigues Pelá, U. Werner, D. Nabok, and C. Draxl, Probing the LDA – 1/2 method as a starting point for G_0W_0 calculations, *Phys. Rev. B* **94**, 235141 (2016).
- [99] T. Higuchi, Y.-S. Liu, P. Yao, P.-A. Glans, J. Guo, C. Chang, Z. Wu, W. Sakamoto, N. Itoh, T. Shimura, T. Yogo, and T. Hattori, Electronic structure of multiferroic BiFeO_3 by resonant soft x-ray emission spectroscopy, *Phys. Rev. B* **78**, 085106 (2008).
- [100] J. A. McLeod, Z. V. Pchelkina, L. D. Finkelstein, E. Z. Kurmaev, R. G. Wilks, A. Moewes, I. V. Solovyev, A. A. Belik, and E. Takayama-Muromachi, Electronic structure of BiMO_3 multiferroics and related oxides, *Phys. Rev. B* **81**, 144103 (2010).
- [101] K. A. McDonnell, N. Wadnerkar, N. J. English, M. Rahman, and D. Dowling, Photo-active and optical properties of bismuth ferrite (BiFeO_3): an experimental and theoretical study, *Chem. Phys. Lett.* **572**, 78 (2013).
- [102] F. Gao, Y. Yuan, K. F. Wang, X. Y. Chen, F. Chen, J.-M. Liu, and Z. F. Ren, Preparation and photoabsorption characterization of BiFeO_3 nanowires, *Appl. Phys. Lett.* **89**, 102506 (2006).

- [103] R. V. Pisarev, A. S. Moskvina, A. M. Kalashnikova, and T. Rasing, Charge transfer transitions in multiferroic BiFeO₃ and related ferrite insulators, *Phys. Rev. B* **79**, 235128 (2009).
- [104] S. Zeljković, T. Ivas, H. Maruyama, and J. C. Nino, Structural, magnetic and optical properties of BiFeO₃ synthesized by the solvent-deficient method, *Ceram. Int.* **45**, 19793 (2019).
- [105] M. Basith, N. Yesmin, and R. Hossain, Low temperature synthesis of BiFeO₃ nanoparticles with enhanced magnetization and promising photocatalytic performance in dye degradation and hydrogen evolution, *RSC Adv.* **8**, 29613 (2018).
- [106] R. Palai, R. S. Katiyar, H. Schmid, P. Tissot, S. J. Clark, J. Robertson, S. A. T. Redfern, G. Catalan, and J. F. Scott, β phase and γ - β metal-insulator transition in multiferroic BiFeO₃, *Phys. Rev. B* **77**, 014110 (2008).
- [107] P. S. V. Mocherla, C. Karthik, R. Ubig, M. S. Ramachandra Rao, and C. Sudakar, Tunable band gap in BiFeO₃ nanoparticles: The role of microstrain and oxygen defects, *Appl. Phys. Lett.* **103**, 022910 (2013).
- [108] R. Moubah, G. Schmerber, O. Rousseau, D. Colson, and M. Viret, Photoluminescence investigation of defects and optical band gap in multiferroic BiFeO₃ single crystals, *Appl. Phys. Express* **5**, 035802 (2012).
- [109] M. Goffinet, P. Hermet, D. I. Bilc, and P. Ghosez, Hybrid functional study of prototypical multiferroic bismuth ferrite, *Phys. Rev. B* **79**, 014403 (2009).
- [110] A. Stroppa and S. Picozzi, Hybrid functional study of proper and improper multiferroics, *Phys. Chem. Chem. Phys.* **12**, 5405 (2010).
- [111] H. A. A. Khan, S. Ullah, G. Rehman, S. Khan, and I. Ahmad, First principle study of band gap nature, spontaneous polarization, hyperfine field and electric field gradient of desirable multiferroic bismuth ferrite (BiFeO₃), *J. Phys. Chem. Solids* **148**, 109737 (2021).
- [112] E. Sagar, R. Mahesh, N. Pavan Kumar, and P. Venugopal Reddy, Investigation of structural and multiferroic properties of three phases of BiFeO₃ using modified Becke Johnson potential technique, *J. Phys. Chem. Solids* **110**, 316 (2017).
- [113] R. Mahesh and P. Venugopal Reddy, A study of ferroelectric and magnetic properties of rare earth (RE=La, Nd, Sm, Gd) doped BiFeO₃ using modified Becke Johnson potential with SOC techniques, *Mater. Chem. Phys.* **232**, 460 (2019).
- [114] S. J. Clark and J. Robertson, Band gap and Schottky barrier heights of multiferroic BiFeO₃, *Appl. Phys. Lett.* **90**, 132903 (2007).
- [115] I. Sosnowska, W. Schäfer, W. Kockelmann, K. Andersen, and I. Troyanchuk, Crystal structure and spiral magnetic ordering of BiFeO₃ doped with manganese, *Appl. Phys. A* **74**, s1040 (2002).
- [116] S. Basu, L. Martin, Y. Chu, M. Gajek, R. Ramesh, R. Rai, X. Xu, and J. Musfeldt, Photoconductivity in BiFeO₃ thin films, *Appl. Phys. Lett.* **92**, 091905 (2008).
- [117] A. R. Zanatta, Revisiting the optical band gap of semiconductors and the proposal of a unified methodology to its determination, *Sci. Rep.* **9**, 11225 (2019).
- [118] M. Saritaş and H. D. McKell, Absorption coefficient of Si in the wavelength region between 0.80-1.16 μm , *J. Appl. Phys.* **61**, 4923 (1987).
- [119] J. Kangsabanik, M. K. Svendsen, A. Taghizadeh, A. Crovetto, and K. S. Thygesen, Indirect band gap semiconductors for thin-film photovoltaics: High-throughput calculation of phonon-assisted absorption, [arXiv:2207.09569](https://arxiv.org/abs/2207.09569).
- [120] J.-L. Bredas, Mind the gap! *Mater. Horiz.* **1**, 17 (2014).
- [121] A. Walsh, D. J. Payne, R. G. Egdell, and G. W. Watson, Stereochemistry of post-transition metal oxides: revision of the classical lone pair model, *Chem. Soc. Rev.* **40**, 4455 (2011).
- [122] X. Shen, Y. Xia, G. Wang, F. Zhou, V. Ozolins, X. Lu, G. Wang, and X. Zhou, High thermoelectric performance in complex phosphides enabled by stereochemically active lone pair electrons, *J. Mater. Chem. A* **6**, 24877 (2018).
- [123] R. Ali Saha, A. Halder, D. Fu, M. Itoh, T. Saha-Dasgupta, and S. Ray, The critical role of stereochemically active lone pair in introducing high temperature ferroelectricity, *Inorg. Chem.* **60**, 4068 (2021).
- [124] P. Ravindran, R. Vidya, A. Kjekshus, H. Fjellvåg, and O. Eriksson, Theoretical investigation of magnetoelectric behavior in BiFeO₃, *Phys. Rev. B* **74**, 224412 (2006).
- [125] L. Volkova and D. Marinin, Magnetoelectric ordering of BiFeO₃ from the perspective of crystal chemistry, *J. Supercond. Novel Magn.* **24**, 2161 (2011).
- [126] A. Lyogenkaya, G. Grechnev, O. Kotlyar, A. Panfilov, and V. Gnezdilov, Electronic structure and magnetic properties of FeTe, BiFeO₃, SrFe₁₂O₁₉ and SrCoTiFe₁₀O₁₉ compounds, *Ukr. J. Phys.* **61** 523 (2016).
- [127] M. Rafiee and S. J. Asadabadi, Quantum size effects in Pb/Si(111) thin films from density functional calculations, *Comput. Mater. Sci.* **47**, 584 (2009).
- [128] E. E. Salpeter and H. A. Bethe, A relativistic equation for bound-state problems, *Phys. Rev.* **84**, 1232 (1951).
- [129] E. K. Chang, M. Rohlfing, and S. G. Louie, Excitons and Optical Properties of α -Quartz, *Phys. Rev. Lett.* **85**, 2613 (2000).
- [130] N. Ashcroft and N. Mermin, *Solid State Physics*, HRW international editions (Holt, Rinehart and Winston, 1976).
- [131] R. G. Parr and Y. Weitao, *Density-Functional Theory of Atoms and Molecules* (Oxford University Press, USA, 1994).
- [132] Y. Gillet, Ab initio study of Raman and optical spectra of crystalline materials and their temperature dependence, Ph.D. thesis, Université catholique de Louvain, Louvain-la-neuve, Belgium (2017).
- [133] V. M. Adamyan, O. A. Smirnov, and S. V. Tishchenko, Effects of environmental and exciton screening in single-walled carbon nanotubes, *J. Phys.: Conf. Ser.* **129**, 012012 (2008).
- [134] Q. Gao, Y. Peng, T. Wang, C. Shen, C. Xia, J. Yang, and Z. Wei, Quantum confinement effects on excitonic properties in the 2D vdW quantum system: The ZnO/WSe₂ case, *Adv. Photo. Res.* **2**, 2000114 (2021).
- [135] Q. Meng, L. Wu, H. L. Xin, and Y. Zhu, Retrieving the energy-loss function from valence electron energy-loss spectrum: Separation of bulk-, surface-losses and Cherenkov radiation, *Ultramicroscopy* **194**, 175 (2018).
- [136] S. Simsek, A. M. Mamedov, and E. Ozbay, Electron energy-loss spectroscopy and the electronic structure of ABO₃ ferroelectrics: First principle calculations, [arXiv:1204.4024](https://arxiv.org/abs/1204.4024).
- [137] V. K. Dien, N. T. Han, W.-P. Su, and M.-F. Lin, Spin-dependent optical excitations in LiFeO₂, *ACS Omega* **6**, 25664 (2021).
- [138] J. J. Sakurai, *Modern Quantum Mechanics; Revised Edition* (Addison-Wesley, Reading, MA, 1994).

- [139] H. Wang, Y. Zheng, M.-Q. Cai, H. Huang, and H. L. Chan, First-principles study on the electronic and optical properties of BiFeO₃, *Solid State Commun.* **149**, 641 (2009).
- [140] T. Eyob, K. Namera, and L. Demeyu, Dopant size effect on BiFeO₃ perovskite structure for enhanced photovoltaic activity, [arXiv:2205.03785](https://arxiv.org/abs/2205.03785).
- [141] M. Idrees, M. Nadeem, M. Mehmood, M. Atif, K. H. Chae, and M. M. Hassan, Impedance spectroscopic investigation of delocalization effects of disorder induced by Ni doping in LaFeO₃, *J. Phys. D* **44**, 105401 (2011).
- [142] J. Zirzmeier, S. Schrettl, J. C. Brauer, E. Contal, L. Vannay, É. Brémond, E. Jahnke, D. M. Guldi, C. Corminboeuf, R. R. Tykwinski, and H. Frauenrath, Optical gap and fundamental gap of oligoynes and carbyne, *Nat. Commun.* **11**, 4797 (2020).
- [143] S. Ivanov, P. Nordblad, R. Tellgren, T. Ericsson, S. Korchagina, L. Rybakova, and A. Hewat, Influence of PbZrO₃ doping on the structural and magnetic properties of BiFeO₃, *Solid State Sci.* **10**, 1875 (2008).
- [144] R. Resta and D. Vanderbilt, Theory of polarization: a modern approach, in *Physics of Ferroelectrics* (Springer, 2007), pp. 31–68.
- [145] T. Qi, I. Grinberg, and A. M. Rappe, Correlations between tetragonality, polarization, and ionic displacement in PbTiO₃-derived ferroelectric perovskite solid solutions, *Phys. Rev. B* **82**, 134113 (2010).
- [146] R. D. King-Smith and D. Vanderbilt, Theory of polarization of crystalline solids, *Phys. Rev. B* **47**, 1651 (1993).
- [147] D. Vanderbilt and R. D. King-Smith, Electric polarization as a bulk quantity and its relation to surface charge, *Phys. Rev. B* **48**, 4442 (1993).
- [148] R. Resta, Macroscopic polarization in crystalline dielectrics: the geometric phase approach, *Rev. Mod. Phys.* **66**, 899 (1994).
- [149] R. Resta, Theory of the electric polarization in crystals, *Ferroelectrics* **136**, 51 (1992).
- [150] R. Resta, Macroscopic electric polarization as a geometric quantum phase, *Europhys. Lett.* **22**, 133 (1993).
- [151] R. Resta, M. Posternak, and A. Baldereschi, Towards a Quantum Theory of Polarization in Ferroelectrics: The Case of K₂SeO₆, *Phys. Rev. Lett.* **70**, 1010 (1993).
- [152] D. Vanderbilt, *Berry Phases in Electronic Structure Theory: Electric Polarization, Orbital Magnetization and Topological Insulators* (Cambridge University Press, 2018).
- [153] N. A. Spaldin, A beginner's guide to the modern theory of polarization, *J. Solid State Chem.* **195**, 2 (2012).